Numerical Investigation of Parabolic Trough Solar Collector Integrated with Phase Change Material for Steam Supply in a Malt Kilning Process - a case of Assela Malt Factory

Jara Abera Kumsa

A Thesis Submitted to The department of Thermal and Aerospace Engineering

School of Mechanical, Chemical and Materials Engineering

Presented in Partial Fulfillment of the Requirement for the Degree of Master of Science in Thermal Engineering

Office of Graduate Studies

Adama Science and Technology University

August, 2021

Adama, Ethiopia

Numerical Investigation of Parabolic Trough Solar Collector Integrated with Phase Change Material for Steam Supply in a Malt Kilning Process - a case of Assela Malt Factory

Jara Abera Kumsa

Advisor: Dr. Addisu Bekele

A Thesis Submitted to The department of Thermal and Aerospace Engineering

School of Mechanical, Chemical and Materials Engineering

Presented in Partial Fulfillment of the Requirement for the Degree of Master of Science in Thermal Engineering

Office of Graduate Studies

Adama Science and Technology University

August, 2021

Adama, Ethiopia

Declaration

I hereby declare that this Master Thesis entitled **"Numerical Investigation of Parabolic Trough Solar Collector Integrated with Phase Change Material for Steam Supply in a Malt Kilning Process - a case of Assela Malt Factory"** is my original work. That is, it has not been submitted for the award of any academic degree, diploma or certificate in any other university. All sources of materials that are used for this thesis have been duly acknowledged through citation.

Jara Abera Kumsa	________________________	________________
Name of the Student	Signature	Date

Recommendation

I, the advisor of this thesis, hereby certify that I have read the thesis entitled **"Numerical Investigation of Parabolic Trough Solar Collector Integrated with Phase Change Material for Steam Supply in a Malt Kilning Process - a case of Assela Malt Factory"** prepared under my guidance by **Jara Abera Kumsa** submitted in partial fulfillment of the requirements for the degree of Masters of Science in Thermal engineering. Therefore, I recommend the submission of the thesis to the department following the applicable procedures.

Dr. Addisu Bekele	______________________	_______________
Advisor	Signature	Date

Approval Page

I, the advisor of the thesis entitled **"Numerical Investigation of Parabolic Trough Solar Collector Integrated with Phase Change Material for Steam Supply in a Malt Kilning Process - a case of Assela Malt Factory"** and developed by **Jara Abera Kumsa**, hereby certify that the recommendation and suggestions made by the board of examiners are appropriately incorporated into the final version of the thesis.

Dr. Addisu Bekele	____________________	______________
Advisor	Signature	Date

We, the undersigned, members of the Board of Examiners of the thesis by **Jara Abera** have read and evaluated the thesis entitled "**Numerical Investigation of Parabolic Trough Solar Collector Integrated with Phase Change Material for Steam Supply in a Malt Kilning Process - a case of Assela Malt Factory"** and examined the candidate during the open defense. This is, therefore, to certify that the thesis is accepted for partial fulfillment of the requirement of the degree of Master of Science in Thermal Engineering.

____________________	____________________	____________________
Chairperson	Signature	Date
____________________	____________________	____________________
Internal Examiner	Signature	Date
____________________	____________________	____________________
External Examiner	Signature	Date

Finally, approval and acceptance of the thesis is contingent upon submission of its final copy to the Office of Postgraduate Studies (OPGS) through the Department Graduate Council (DGC) and School Graduate Committee (SGC).

____________________	____________________	____________________
Department Head	Signature	Date
____________________	____________________	____________________
School Dean	Signature	Date
____________________	____________________	____________________
Office of Postgraduate Studies, Dean	Signature	Date

AKNOWLEDMENT

Frist of all, I would like to thank my creator, my strong pillar, my source of inspiration, wisdom, knowledge, and understanding Almighty God. Then, I am greatly thankful to my thesis advisor **Dr. Addisu Bekele (Associate Professor of Thermal Engineering)**, for providing me with a definite direction, professional guidance, boundless support, and constant encouragement from the beginning of the work-study and moral support in many ways during the study period.

I would especially like to express my deepest appreciation to my parents especially my mother hero **Asnakech Gebeyehu** for her prayer, unfailing supporting, motivating and encouraging me throughout many ups and downs until today. Without her I would have never been able to achieve my dream and thanks for her support, in always having my back.

I would also like to thanks all my best friends and classmates for their encouragement, suggestion, and assistance, and gave a worthy comment on my work and through the process of researching.

Finally, I would like to thank Assela Malt Factory staff for their indispensable advice and supporting for me during the research work.

TABLE OF CONTENTS

LIST OF TABLES

LIST OF FIGURES

LIST OF SYMBOLS AND ABBREVIATION

LCC - Life cycle cost

LCS - Life cycle saving

CI - Investment cost

CF - Cash flow

DNI – Direct normal irradiance

DR - Daily range temperature of the day

FDM - Finite difference method

FPC - Flat plate collector

HCE - Heat collecting element

HTF – Heat Transfer Fluid

LHTES –Latent heat thermal energy storage

NTU - Number of transfer unit

NPV - Net present value

PCM – Phase Change Materials

PTC- Parabolic trough collector

PTSC - Parabolic Trough Solar Collector

TES – Thermal energy storage

SHTES – Sensible thermal energy storage

ST - Local solar time

PDE- Partial Differential Equation

ST - Shell and tube

Symbols	Name	units
$\dot{m}$	Mass flow rate	kg/s
C	Specific heat capacity	J/kg.K
I	Global hourly radiation	$W/_{m^2}$
h	Convective heat transfer coefficient	$W/_{m^2.K}$
T_m	Melting temperature	K
T_i	Inlet temperature of HTF	K
m	Mass	kg
τ_o	Non dimensional time	-
ρ_{pcm}	Density of PCM	$kg/_{m^3}$
m_{PCM}	Mass of PCM	kg
V_{PCM}	Volume of PCM	m^3
H	Heat fusion of the pcm	kJ/kg
Nu	Nusselt number	-
T	Storage duration	second
k_m	Thermal conductivity of PCM	
ΔT	Temperature difference	K
ΔP	Pressure drop	Pa
H	Global daily radiation	$W/_{m^2}$
$\bar{H}_o$	Extraterrestrial radiation	$W/_{m^2}$
Pr	Prandtl number	-

GREEK LETTERS

α	Thermal absorptivity	σ	Stefan Boltzmann($W/_{m^2.K^4}$)
β	Surface slope angle (°)	φ	Latitude angle (°)
γ	Surface azimuth angle (°)	ω	Solar hour angle (°)
δ	Declination angle (°)	θ_i	Incidence of angle (°)
ε	Emissivity	θ_z	Zenith angle (°)
μ	Dynamic viscosity	ϑ	Kinematic viscosity
τ	Transmittance	α_S	Solar altitude angle (°)
ϵ	porosity	η	Efficiency

SUBSCRIPTS

A	Receiver tube
ab	Energy absorbed
cv	Convection
ext	External
f	Working fluid
g	Glass envelope
int	Internal
max	Maximum
min	Minimum
r	Radiation
Opt	Optical
st	Storage

ABSTRACT

Assela Malt Factory is one of industrial zone used medium temperature in the kilning room which sourced from the boiler room which driven by electric power. Due to high electric consumption for steam supply, Assela malt factory need 26,670,600 KWh thermal energy per year. Solar energy is the most abundant renewable energy sources which is accessible and free to all countries. In this study the performance of parabolic trough solar collector incorporating with phase change materials is investigated which used as alternative energy sources for steam supply in Malt kilning process at Assela Malt factory. A transient one dimensional explicit finite difference method is used to investigate performance of PTSC and charging process of thermal energy storage which done by using MATLAB. Maximum optical and thermal efficiency of parabolic trough solar collector is about 76.4% and 70% respectively. By increasing receiver tube length temperature outlet of the collector also increasing and vice versa. Mass flow rate and PTC temperature outlet have inversely proportional. Thermal energy storage system with shell and tube configuration using D-mannitol as phase change material is studied. This PCM is stored in shell side and water (steam) used as HTF flows in the tube for transferring heat from HTF to PCM. From numerical simulation to fulfill thermal energy demand of Assela Malt factory approximately around 84 number of parabolic trough solar collectors (1428 m^2 *solar field area) of* $0.05\ kg/s$ *mass flow rate of heat transfer fluid are required. To substitute the gap during night time mass of 4139 kg of D-mannitol (phase change materials) and 220 number of HTF tubes with 0.06 m diameter and 2.7 m length of each tube are required. Totally the results from a numerical simulation are performed with meteorological data Kulumsa station.*

Key word: *Heat transfer fluid, Malt kilning, parabolic trough, phase change materials, thermal energy storage.*

CHAPTER ONE

INTRODUCTION

1.1 Background of Study

Asella Malt factory was established on the main road of Addis Ababa-Asella near Kulumsa Agricultural Research Center on around 14.7 hectares of land with 9.3 million Birr capital on September 1/1984 G.C. It was established with the aim of producing Malt for domestic breweries in the country.

Assela Malt Factory, the state company recently sold to Ethiopian farmers, is set to triple its Malt production to one million quintals per year. Currently, the factory is producing some 360,000 quintals of barley per year. In Ethiopia Assela is the largest Malt supplier to most of the breweries in the country. It was sold for 1.3 billion birr (around $46 million at the current exchange rate) to Oromia Cooperatives Union since May 2018. It has been covering 25-30% of the demand of Malt in Ethiopia.

Malting could be prepared in three-step i.e. Soaking (grain steeped in water), germination (improvement of growing and improving enzymatic movement), and kilning (drying the grain and end the enzymatic action) (Kumar et al, 2016).

Figure 1. 1. Malting process

The industrial region expends most of its energy in either electrical or thermal energy frameworks. Electrical energy is utilized for lighting, air conditioning, and for working engine drives through Thermal energy (heat) is utilized to handle warming applications such as coloring, fading, cooking, drying, etc. A significant share of energy demand within the industrial sector is for the heating process (Sharma, 2017).

Assela Malt Factory is one of industrial zone used medium temperature in the kilning room which sourced from the boiler room. The electric boiler produces a steam with temperature up to 160°C, at pressure of 6 Bar and steam mass flow rate 10000 kg/hr. The steam is directed to the heat exchanger (at which heat is transferred from steam to the air) then the heated air is directly goes to the kilning room and the warm water is back to the boiler. Due to fast growth in conventional fuel costs and natural imperatives, enterprises are not attracted to utilize fossil fuels in the industrial sector any longer. By applying renewable energy based systems in industries, the greenhouse emissions could be reduced significantly.

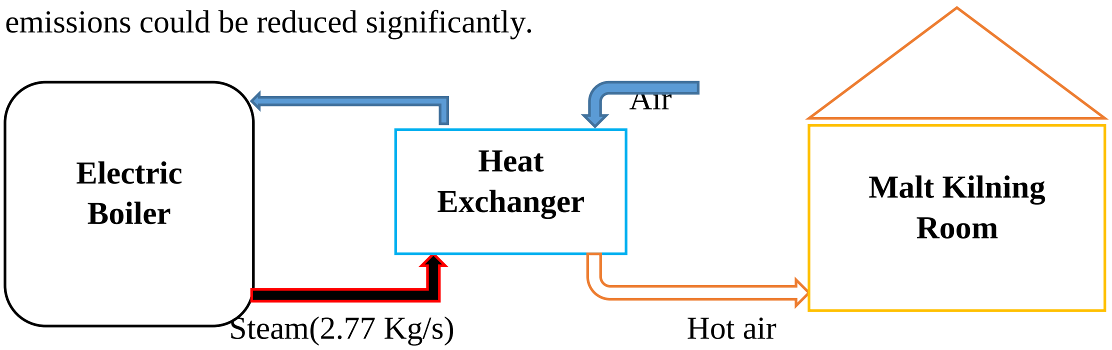

Figure 1. 2. Malt kilning process at Assela Malt Factory

Therefore, traditional energy supplies should be shifted to renewable sources of energy and new technologies has to be developed and applied in industries (Mekhilef, 2011).

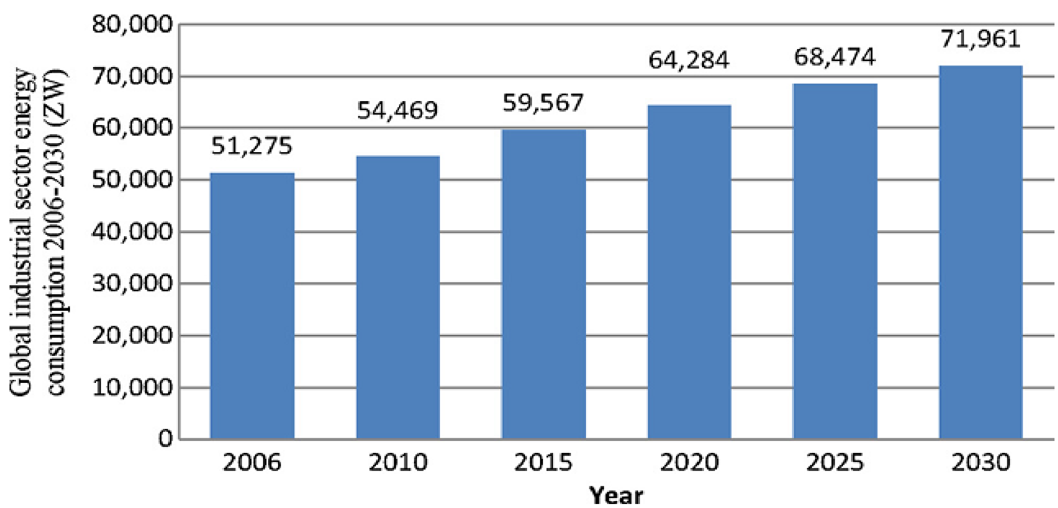

Figure 1. 3. Global industrial sector energy consumption during 2006–2030 (Mekhilef, 2011).

Solar energy is a kind of renewable energy and also the most abundant renewable energy source that is accessible and free to all countries. Solar power is energy from the sun that is harnessed and converted into two common applications, electrical and thermal energy. Overall, solar energy technology has two main categories that could convert solar energy into electrical energy. One application is concentrating solar power (CSP) systems that produce heat or electricity by hundreds of mirrors which concentrate the sunlight to a temperature commonly between 400 and 1000 °C. In addition, CSP as a solar energy technology can operate either through storing heat or through combination with fossil-fueled power plants such as natural gas and oil power plants, making power available at times when the sun is not shining (Shahsavari, 2018).

1.2. Energy Demand for Kilning

Manger et al (2001) have highlighted that the energy consumption of the kiln process is considerable. For a 24h kiln the heating capacity is approximately 20,000 kW for a batch size of 360 tonnes of barley as green Malt and the aeration capacity is 1,700,000 m^3/hr at 1,850 Pa total air pressure. In a hot climate country the production of 1 tonne of Malt requires approximately 800 kWh as heat and approximately 90 kWh as electrical energy just for the kilning. Due to the higher absolute air humidity because of the higher ambient temperature the air volume for the kilning process as well the heat demand is higher compared to European countries (Hauner, 2019).

Smith et al (1980) Up to 80% of the total energy requirement for Malting is represented by air heating in the kilning process. This feasibility study concludes that in a good solar location (Colorado, USA) up to 40% of the kiln heat energy can be supplied by solar collectors simply by passing the intake air through them. By scheduling kiln operation solar heat availability could be maximized. Conventional back up heating would ensure completion under adverse conditions. Some 40% of the heat collected during daytime could be stored by pebble bed unit for night time use. Alternatively, Malt partially kilned on one day could be stored overnight for completion on the second day. In general terms, Malt kilning is an excellent application of solar energy, providing direct heat, free from combustion products, with no need for heat exchangers. The current cost of solar energy is marginal compared with conventional fuel. Its attractions include its cleanliness, freedom from pollution and its fixed cost over the useful life of the equipment.

Hauner et al (2019) the kilning of green Malt requires large amounts of thermal energy which is nowadays mainly based on fossil fuels. In a standard state-of-the-art Malting plant in South-East

Asia, 800 kWh is needed for one tonne of Malt. At such a high level of energy usage, it is obvious that more sustainable energy sources must be investigated.

In Vialonga, Portugal the largest demonstration system with a total of 315 large-area flat plate collectors (4,725 m² gross collector area) mounted on ground and connected to an atmospheric 400 m³ solar energy storage tank is being commissioned by spring 2014. The energy from the sun will be used to supply the so called drying kiln with hot water at a temperature of around 75-80°C to heat up drying air for drying of green Malt (Mauthner, 2013).

Generally using solar energy as alternative energy is preferable for Ethiopian industry for heat generation. Assela Malt factory is one of the large factory in Ethiopia which consume much energy for drying of Malt. We can decrease energy consumption of this factory by using renewable energy technology especially parabolic trough solar collector.

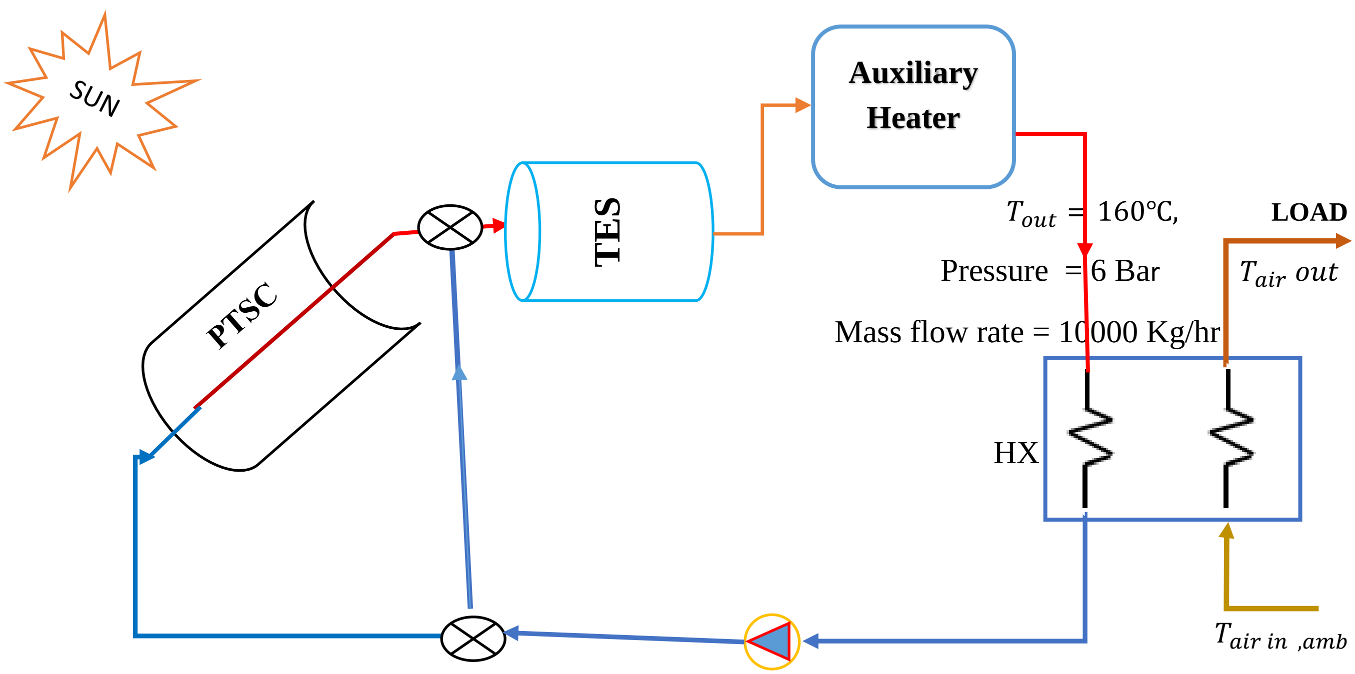

Figure 1. 4. Schematic diagram of parabolic trough solar integrated with phase change material for Assela Malt factory drying process.

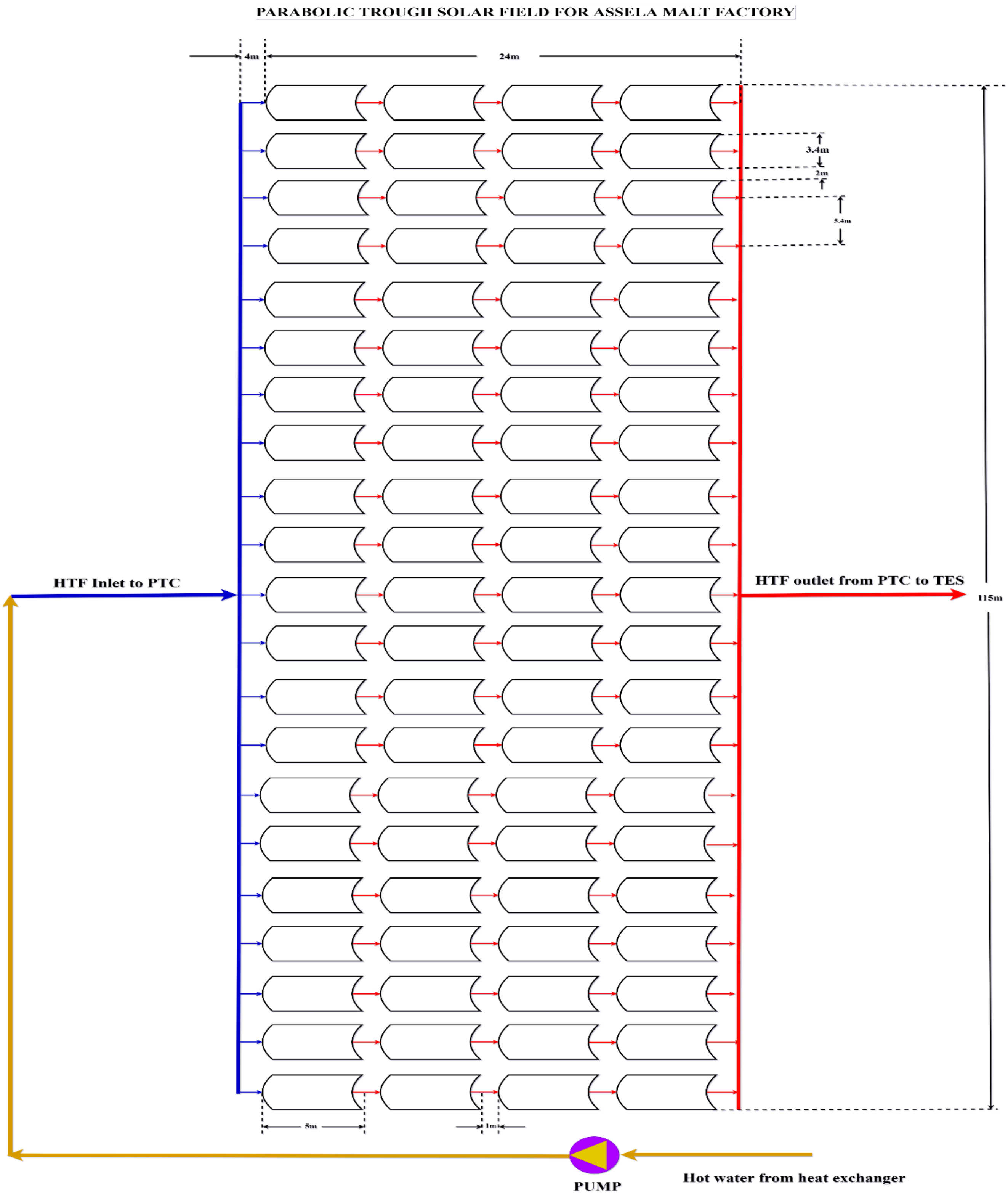

Figure 1. 5. Parabolic trough collector solar field for Assela Malt factory

1.3 Statement of Problem

In our country, nearly all industrial areas are dependent on the electrical power supply and fossil fuel for an energy source rather than using renewable energy sources. In this way, energy charges are rising day to day additionally using fossil fuel that leads to greenhouse gas emissions, and air pollution influence the environment.

In Assela Malt factory electrical boiler is used to generate and supply steam for the process of Malt kilning. The boiler uses electric power for steam production of 160 ℃. Due to high electric consumption for steam supply, Assela malt factory need 26,670,600 KWh thermal energy per year. So the factory expends high cost to buy this electric power every month. Only for the electric boiler which supplies steam the factory pays millions Birr per year. This is seriously affecting the profit of the factory.

The kilning of green Malt requires large amounts of thermal energy which is nowadays mainly based on electric power and fossil fuels. In a standard state-of-the-art Malting plant in South-East Asia, 800 kWh is needed for one tonne of Malt (Hauner et al., 2019). Solar energy (Parabolic trough solar collector) integrated with phase change material as an alternative free renewable energy source is the solution for steam supply in the Malt kilning process. This study will tend this factory to use solar technology integrated with phase change materials rather than electrical boilers to generate steam demand for Malt kilning. Solar energy is available during the daytime only. To substitute this intermittent gap using phase change material (PCM) as thermal energy storage which stores energy during the daytime and releases energy when solar radiation is not available.

1.4 Objectives

1.4.1 General Objective

The general objective of this study is the performance investigation of a parabolic trough solar collector integrated with phase change material for steam supply in a Malt kilning process at the Assela Malt factory.

1.4.2 Specific Objectives

Specific objectives of this study are:

- Investigate the thermal energy demand of Assela Malt Factory
- Size and design the parabolic trough solar collector solar field layout which required to fulfill the thermal energy demand of steam supply for Malt drying.
- Numerically analyze the optical and thermal performance of the parabolic trough solar collector.
- Study the performance of the PCM thermal energy storage integrated to the PTSC.

1.5 Significance of the Study

The significance of this study is energy shift from using electrical boiler to solar energy sources. Conversion of energy to free renewable energy has a contribution for factory profit also for country development by reducing energy consumption. This thesis is looking for using parabolic trough solar collector integrated with phase change material for Malt kilning in Assela Malt factory.

1.6 Scope of the Study

This study covers only the theoretical performance or simulation of a parabolic trough solar collector integrated with phase change material for Malt drying which has involvement in reducing energy consumption by using solar energy as an alternative source of energy for steam supply in the Assela Malt factory.

CHAPTER TWO

LITERATURE REVIEW

2.1 Introduction

In this chapter, the previous work done by different researchers on the solar-powered heating process of industrial applications is reviewed. Also, parabolic trough solar collectors integrated with phase change materials for steam supply to drying are reviewed in this chapter.

2.2 Solar Collector

Typical categories of renewable energy resources are accessible in nature such as – solar, wind, geothermal, tidal, biomass...etc. from those accessible renewable energies, solar energy is the foremost utilized form of energy, as it's crucial and abundant in nature (Raghurajsinh, 2016).

A solar collector could be an extraordinary kind of heat exchanger that changes solar radiant energy into heat. As there are a few collector types within the market, an introductory overview was fitting to choose the suitable type.

In general, a separation can be made between Stationary Collectors (non-concentrating) with Flat Plate Collectors (FPC), Evacuated Tube Collectors (ETC), Vacuum Tube Collectors CPC (Compound Parabolic Concentrator), and Concentrating Collectors with Parabolic Trough Collectors (PTC), Linear Fresnel Reflectors (LFR), Parabolic Dish Reflectors (PDR) and heliostatic field collectors (Hauner, 2019).

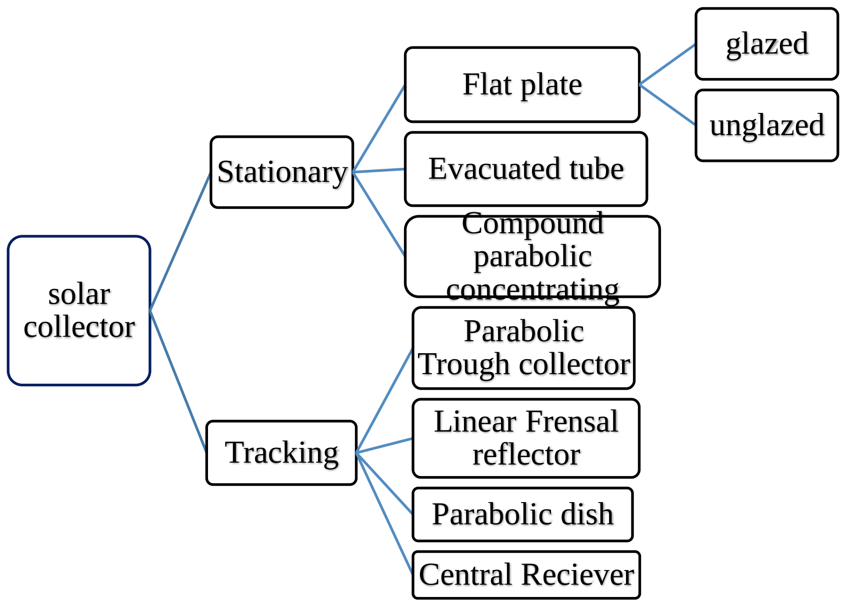

Figure 2. 1. Types of solar collectors.

Non-concentrating

Non-concentrating collectors:-have a collector that is the same as the absorber area. Flat plate collectors are the most common and are used when temperatures below about 80℃ are adequate, such as for space heating.

Concentrating Collectors

Concentrating sun-powered collectors make utilize of optical enhancement of the sun's beams onto a central point or line. Such a collector can create greatly high temperatures due to concentrating energy onto a little receiving region with less region to lose heat as compared with a flat-plate design.

Solar collectors have been chosen because of the following reasons (Hauner, 2019):

- Convenient region because of the continuous radiation intensity throughout the year
- The sourced energy can be directly used for the process
- It is clean energy and does not contribute to the greenhouse effect
- Low investment costs
- Short payback time
- Little additional electrical energy is necessary
- Easy to install and integrate to an existing heating system for a heated pool

Table 2. 1. Types of solar thermal collector

Stationary solar collector type	**Absorber plate**	**Temperature range in (K)**	**Concentration ratio**
Flat plate collector (FPC)	Flat	303-353	1
Evacuated tube collector (ETC)	Flat	323-473	1
Concentrating parabolic collector(CPC)	Tubular	333-513	1-5

Based on temperature range parabolic trough collector is selected for steam supply in the Assela Malt industry.

2.3 Parabolic Trough Solar Collector

Parabolic trough collectors (PTC) belong to line focusing systems. They concentrate the solar energy by reflecting the incident light rays to their focal point. At this height, an absorber tube is placed containing a streaming fluid, the so-called heat transfer fluid (HTF). Both elements have the necessary properties to gain the heat and transfer it from the inlet to the outlet of the tube (see Figure below). The one-axis tracking system enables the perpendicular facing of the collector´s aperture to the sun, thus taking maximum advantage of the solar direct normal irradiance, as illustrated in Figure 2.2 (Chaves, 2019). This technology finds diverse applications and forms of implementation within two main branches: electricity generation and industrial process heat production. Commonly parabolic power plants operate at temperatures ranging from 300°C to 500°C and in for industrial process heat generation between 100°C to 300°C.

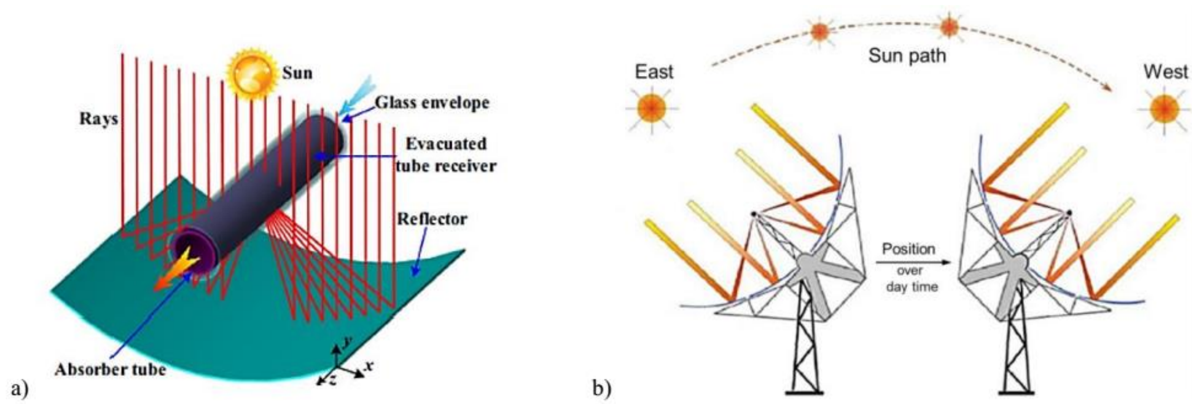

Figure 2. 2. General Scheme on concentrating solar energy at the focal point of a PTC b) One-axis tracking of the sun (Chaves, 2019)

Solar parabolic trough collector (SPTC) contains a receiver (working fluid hollow), a concentric translucent cover, and a parabolic reflector dish. The receiver is fixed permanently at the focus of the parabolic concentrator. The concentric translucent cover is used to defend the receiver pipe from heat losses and hence a vacuum pressure is sustained. The parabolic concentrator is positioned on an unbending structure and the solar tracking mechanism is placed on the stiff structure to path the solar radiation by the parabolic concentrator(Jebasingh & Herbert, 2016). Parabolic trough collectors (PTC) are prepared by curving a sheet of reflective material into a parabolic profile. A steel black tube, surrounded with a glass pipe to decrease heat losses, is located along the focal line of the collector (Kalogirou,2012).

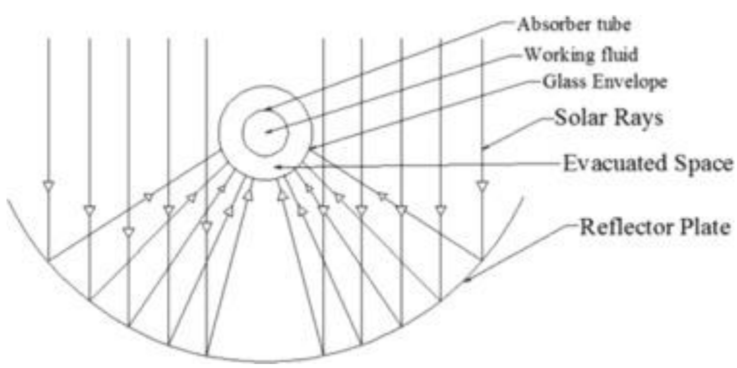

Figure 2. 3. Schematic diagram of solar parabolic trough collector (Jebasingh & Herbert, 2016)

In order to provide high temperatures with great efficiency, a high-performance sun-powered collector is required. Systems with light structures and low-cost technology for process heat applications up to 400 °C may be gotten with parabolic through collectors (PTCs). PTCs can successfully deliver heat at temperatures between 50 and 400 °C (Kalogirou, 2004). The tracking mechanism must be dependable and able to take after the sun with a certain degree of exactness, return the collector to its unique position at the end of the day or amid the night, and additionally track amid periods of irregular cloud cover. Moreover, the following components are utilized for the assurance of collectors, i.e. they turn the collector out of the center to secure it from the perilous natural and working conditions, like wind gust, overheating, and disappointment of the thermal liquid stream mechanism. The specified exactness of the tracking mechanism depends on the collector acceptance point.

Lamrani et al (2018) have studied the thermal performance of a PTSC under transient climatic situations. One dimensional transient model that is based on energy balance equation of collector components developed and solved by implicit finite difference method using Mat lab software. Results obtained show that the length of the receiver tube has a great effect on HTF outlet temperature and using synthetic oil as a working fluid is suitable compared to water.

Ouagued et al (2013) have investigated the performance of a tracking solar parabolic trough collector using a heat transfer model by dividing the receiver into several segments and applying heat balance in each segment over a section of the solar receiver under Algerian climate. Different tilted, tracking collectors and oils are considered so as to determine the most efficient PTSC system.

Marif et al (2014) have investigated the optical and thermal performance of a solar parabolic trough collector under the climate conditions of Algerian Sahara one dimensional implicit finite difference method with energy balance approach. The receiver model depends on an energy balance in each section of the glass envelope, receiver tube, and the fluid developed. Two fluids (liquid water and TherminolVP-1™ synthetic oil) and different tracking systems were considered for the study. They found out that the high optical efficiency is obtained with full tracking equal to 73.92% and the one axis polar East-West and horizontal East-West tracking systems were most desirable for a parabolic trough collector throughout the whole year.

Compared to the multi-dimensional models the 1-D model is superior, because it involves less solution time and complexity. The review study on different models indicates that 1-D energy balance gives reasonable results for short HCEs (< 100 m) The 1-D model becomes insufficient with increasing HCE length, and thus the discretization through the axial direction is needed to reduce the deviation(Yılmaz & Mwesigye, 2018).

Kumar & Kumar (2015) have developed one-dimensional steady state heat transfer in order to estimate the through-out-year performance characteristics in terms of water temperature rise, heat energy generation, optical and thermal efficiency for the climactic conditions of Bhiwani city in India. These all parameters were evaluated for horizontal and vertical plane using analytical simulation by Mat lab R2012a. They concluded that higher heat energy generation is found to be 2.38 kW h/day in May on horizontal plane, 2.46 kW h/day in April on inclined plane, the maximum optical efficiency is attained as 72.26% and 72.4% on horizontal and an inclined plane respectively. The peak instantaneous thermal efficiency is accomplished as 66.78% in July on a horizontal plane, 65.77% in September on the inclined plane of the collector. The result was validated with the existing experimental results of Sandia National Laboratories (SNL).

Mokheimer et al (2014) have investigated the hourly, daily and monthly performance of the PTSC using simulation code developed using EES software under Dhahran, Saudi Arabia weather conditions. Euro Trough solar collector (ET-100) and LUZ solar collector LS-3 PTSC were considered for this study. They concluded that the maximum optical efficiency that can be reached in Dhahran is 73.5%, whereas the minimum optical efficiency is 61%. These results were validated using available experimental data and against the results obtained by the THERMOFLEX code.

Elmohlawy et al (2018) provided a software simulation model for perf ormance prediction of a parabolic trough collectors system (PTCs), as a part of solar thermal power plants. The simulation has been carried out in Mathcad program environment using the equations, correlations, and typical values of certain parameters available in the open literature in addition to methods from widely accepted reference materials and assumptions to the best ability. The software is carried out to predict the solar radiation intensity from sunrise to sunset, the DNI (Direct Normal Irradiance), PTCs parameters which include: heat losses factor (UL), collector efficiency factor (F'), and the heat removal factor (FR), optical efficiency η_{opt}, temperatures, the mass flow rate of heat transfer fluid (HTF), heat transfer to and from PTCs. The effects of the variations in some PTCs design parameters and operating conditions on the PTC solar field performance can be investigated such as the beam radiation incidence angle, the emittance of the receiver, and glass cover using this software model. The calculations were limited to high-temperature oil (therminol VP-1) as HTF. The PTCs model is validated with the experimental and numerical results.

Assefa (2011) has studied his master thesis on Techno-Economic Assessment of Parabolic trough Steam Generation for Hospital. This project aims in analyzing the Technical performance of parabolic trough steam generation and oil fired boiler steam generation system for Black lion general specialized hospital which is located in Addis Ababa and to perform an economic assessment on both systems so as to make a comparison test. Black lion hospital uses one three-pass (3p) wet back fire tube boiler, 3000 kg/hr steam generation capacity at a pressure of 12 bar, with another one standby to satisfy the daily steam demand of different services in the hospital. The hospital uses furnace oil for the generation of the steam, consumes 245 m^3 and pays 1,593,087.41 birr (96,550.00 Dollar) in the fiscal year, 2,008/09.

For different temperature differences between inlet and outlet of the trough collector area and thermal efficiency is checked using Matlab, optimal thermal efficiency of 62.76% and collector area 11000m^2 is found for 300℃ at the outlet and 150℃ at the inlet to the trough. (Assefa, 2011).

Abrahim (2019) has studied his master thesis on Performance Analysis of Parabolic Trough Solar Steam Generators: A case of Wenji Pulp and Paper Factory. His thesis aims in performance analysis of parabolic trough steam generation for Wenji pulp and paper factory which is located in Wenji town. In this paper, the required data is collected from Wenji Pulp and Paper Factory and weather data was taken from the Adama meteorology agency. Thermal modelling of the parabolic trough solar steam generator system is developed. The proposed system functionality is tested using MATLAB software. In present study three different mass flow rates (0.3kg/s, 0.4kg/s and 0.5kg/s) are taken to test temperature of HTF outlet from solar collector.

It's observed that the temperature of HTF is inversely proportional to the mass flow rate. So it's possible to increase or decrease the temperature of HTF by decreasing or increasing mass flow rate respectively.

The corresponding efficiency of the system was found to be equal to 69%. The optical efficiency of the collector was higher i.e. 75 %. The maximum value of thermal efficiency can reach up 68 % (Abrahim, 2019)

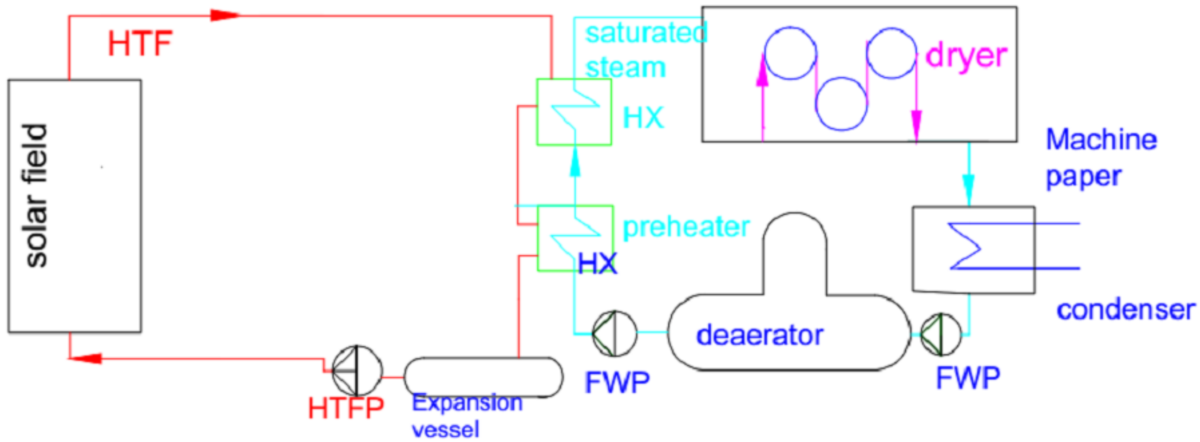

Figure 2. 4. Schematic flow diagram of a parabolic trough solar steam generator (Abrahim, 2019)

Ghodbane and Boumeddane (2016) have presented the efficiencies study of a linear solar concentrator of a parabolic trough type. This study was conducted on the device in the Guemar area, this region is located in the state of El-Oued, which it is found in the southeast of Algeria. Six typical days were selected to conduct the study. The solar collector has been studied optically and thermally. The optical study was using SolTrace. Matlab was used as a device of programming to solve the non-linear system of mathematical equations. The method of finite differences in the implicit case was used as a way of solution.

The main objective of this work was to determine the water vapor temperature which can be reached through this collector in the Guemar region, Algeria. This technology is mature and highly efficient; it is available today in Algeria (the hybrid power plant of Hassi R'Mel and the solar village of Adrar). An energy balance was chosen which is based on heat exchange between the four absorber tubes, the heat transfer fluid, and glass tubes. A program Matlab was developed using the finite difference method in case implicit to simulate the performance of the concentrator.

The optical performance of the collector was higher i.e. 83.61 %. The maximum value of thermal efficiency can reach up 82.80 %, because the inlet temperature of the water is almost identical to the ambient temperature, which thus corresponds to a very good thermal insulation and the lower heat loss to the atmosphere. This reduction in the thermal efficiency after the maximum value is due to thermal losses believe that with increasing water temperatures respectively at the inlet and outlet of the absorber.

This numerical study shows that the fluid temperature exceeds 488 K; they note that there is a change in the water liquid to vapor. This change is caused by a change in the pressure, in the temperature, and in the volume of the heat transfer fluid. Finally, the results are very encouraging for the use of solar energy in the study area (Ghodbane and Boumeddane, 2016).

Reta (2020) has investigated the performance of a parabolic trough solar collector integrated with phase change material for Injera baking application. The cylindrically encapsulated capsules with NaNo3 are used for the storage system. The performance of a solar parabolic trough collector and the charging process of the designed thermal energy storage are studied using the one-dimensional explicit Finite difference method. The result from the numerical simulation shows that four parabolic trough solar collectors connected in parallel are required to fulfill the demand and 168.1 Kg mass of PCM encapsulated in 277 cylindrical capsules is required. Polar East-West and horizontal East-West tracking systems were best appropriate for a parabolic trough collector throughout the entire year.

2.4 Thermal Energy Storage

Thermal energy storage (TES) is defined as a temporary storage of heat energy at high or low temperatures (Dakuri and Hayavadana, 2014). TES systems can be classified as active or passive, the former can be direct or indirect. In the direct type, the storage medium is also the heat transfer fluid, whereas, in the indirect type, a second fluid is used for storing the heat. In passive TES systems, a solid material is used as the storage medium (packed bed) with the heat transfer fluid passes through the storage medium only during the charging and discharging phases (Babajide, 2016).

There are three methods for storing thermal energy, the first two being the most widely used in TES systems (Dincer & Rosen, 2007):

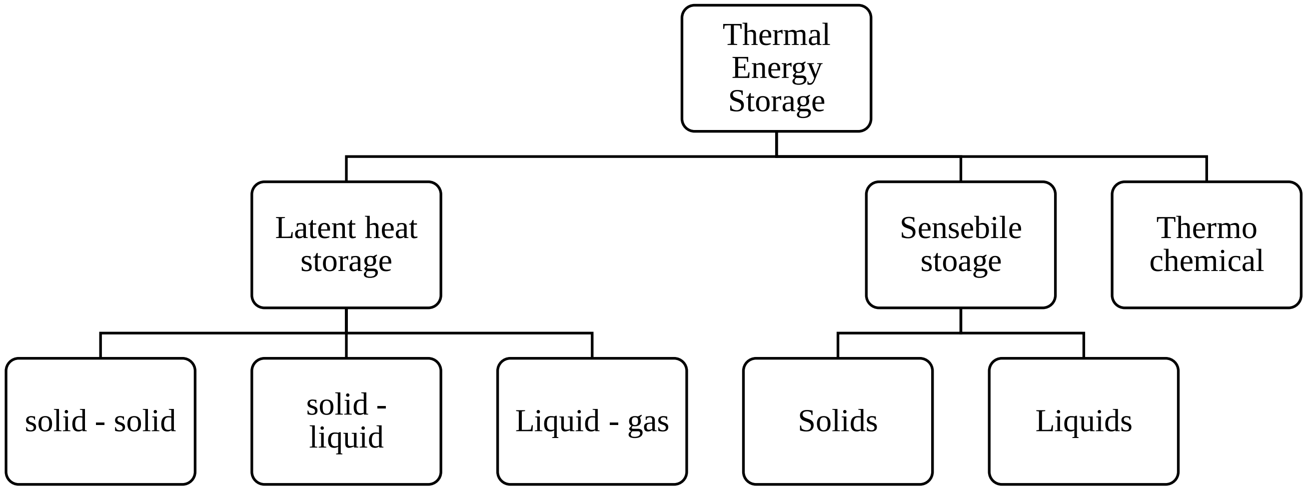

Figure 2. 5. Classification of thermal energy storage and processes

TES can be classified as sensible heat storage (SHS), and latent heat storage (LHS). SHS stores heat by raising the temperature of the storing medium, and it bases on the heat capacity and the change in temperature of the material during the charging and discharging process (Arun and Shukla, 2015). The amount of heat stored depends on the specific heat of the medium, the temperature change, and the size of the storage tank. Whereas, LHS is based on the phase change process of the substance within a limited temperature change. LHS is one of the most efficient ways of storage mediums compared to the competing SHS. It provides a much higher storage density with a smaller temperature difference between storing and releasing heat, and it depends on the phase change process of the material (Dakuri and Hayavadana, 2014).

2.4.1 Sensible Heat Thermal Energy Storage (SHTES)

In SHS, thermal energy is stored by raising the temperature of a solid or liquid. Sensible heat storage is a system that uses the heat capacity of a substance to store heat energy due to the temperature difference. It utilizes the heat capacity and the change in temperature of the storage medium during the process. The amount of heat stored depends on the specific heat of the medium, the temperature change, and the amount of storage material.

2.4.2 Latent Heat Thermal Energy Storage (LHTES)

The LHS systems offer high storage capacity as compared to sensible heat storage and also involve low heat losses. Phase change materials are latent heat storage materials. The thermal energy transfer occurs when a material changes from solid to liquid or liquid to solid. It is based on the heat absorption or release when a storage material undergoes a phase change from solid to liquid or gas or vice-versa. LHTES units are mostly used to store solar energy for high-temperature applications with simultaneous works (Yune, 2019).

Amongst the above thermal heat storage techniques, LHTES is particularly attractive due to its ability to provide high-energy storage density and its characteristics to store heat at the constant temperature corresponding to the phase transition temperature of phase change material (PCM). Latent heat storage can be accomplished through solid-liquid, liquid-gas, solid-gas, and solid-solid phase transformations (Rai, 2001).

2.4.3 Types of Phase Change Materials

PCM can be classified mainly according to their chemical composition and melting temperature. Based on melting Temperature PCM can be divided into low (below 120℃), middle (between 120 and 200℃), and high (above 200℃) melting temperature PCM, as shown in Figure 2.6 (Gustavo et al., 2017).

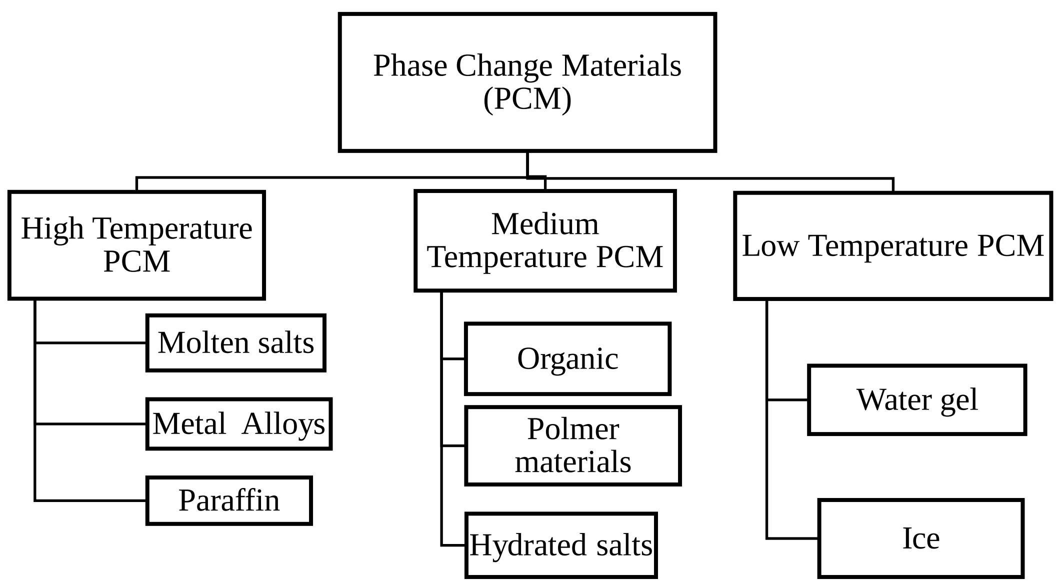

Figure 2. 6. Category of PCM based on melting temperature

These phase change materials have different advantage and disadvantages which is discussed in Table 2.2.

Table 2. 2. Advantage and disadvantages of different types of phase change materials

Type of Materials	Advantage	Disadvantage
Organics PCMs	• Available in a large temperature range • No super cooling • Compatible with other materials • No separation • Chemically PCMs are stable • These are safe to use • Non-reactive in nature • Can be recycled	• Low thermal conductivity • large volume changes • Flammable • Expensive except technical grade paraffin wax
Inorganic PCMs	• High volumetric latent heat • Less expensive • Easily available • Thermal conductivity is higher • The thermal fusion of these PCMs are very high • Lower volumetric variation • These PCMs are non-flammable	• Changed volume is remarkably high • Supercooling • Corrosiveness
Eutectics	• The melting point of these PCMs are sharp • High volumetric storage density	Less thermophysical properties data is available

2.4.3.1 Selection Principles and Required Thermophysical Properties of PCM

The performance of the selected materials in various aspects will directly affect the heat storage ability and thermal storage efficiency. Therefore phase change material must meet certain criteria and possess certain material characteristics. The following six major requirement types are given in detail based on thermodynamics, kinetics, chemistry, and economics of the PCM (Wei et al., 2018).

- **Thermal performance requirements.**

The melting temperature of the material must be much with application temperature to get the maximumefficiency. For the same phase change temperature, high latent and specific heat makes the thermalstorage density as great as possible. Relatively large thermal conductivity is required to have improved system efficiency of the storage design. To avoid phase separation phenomena caused by density differences between the solid and liquid states the PCM should have a consistent chemicalcomposition in both phases.

  - ✓ The suitable phase-change temperature in the desired operating temperature range;
  - ✓ high thermal conductivity;
  - ✓ high latent heat of phase transition per unit mass;
  - ✓ high specific heat and high density;
  - ✓ congruent melting and long term thermal stability;
  - ✓ Favorable phase equilibrium and no segregation;
  - ✓ small volume variation on phase-change;

- **Physical performance requirements.**
  - ✓ Good phase equilibrium
  - ✓ Low vapor pressure
  - ✓ High density
  - ✓ Small volume change in the phase change process
- **Dynamic performance requirements**

As low as possible during solidification, and no super-saturation during melting. Fast crystallization is required to raise the dynamic response-ability of the whole thermal storage system.

- **Chemical performance requirements**
  - ✓ Good chemical stability
  - ✓ Minimal corrosiveness and anti-oxidation
  - ✓ The material should be non-toxic, non-flammable, non-explosive, and safe to use.
  - ✓ Completely reversible melting/solidification cycles;
  - ✓ long term chemical stability and no degradation after a large number of
  - ✓ melting/solidification cycles;
  - ✓ no corrosiveness and capability with construction materials;
  - ✓ Nontoxic, non-flammable, and non-explosive.
- **Economic performance requirements**
  - ✓ Abundant and available;
  - ✓ Cost-effective.
  - ✓ The PCM is low-cost and possesses good industrial utility.
- **Technical performance requirements:**

The selected material should be

  - ✓ technically efficient,
  - ✓ Compact, reliable, and applicable.

Lianga et al (2017) have presented an experimental study on the TES performance of water tanks with PCMs in the solar heating system. The WS-PCM-TES is composed of 72 phase change heat storage units, stainless steel fixed support, and a square heat preservation water tank. The dimensions of the phase change heat storage unit are diameter 50 mm and length is 450 mm. Each unit consumes 0.367 kg of stainless steel and the volume is 0.883 L. The PCMs are encapsulated in a molten state, and a certain volume is reserved to accommodate the volume change before and after the phase transition. Thus, 0.685 kg of PCMs can be encapsulated in a single unit, the total mass is 49.32 kg. It was concluded that increasing the heat storage density of the energy storage water tank can increase the heat storage capacity and the heat storage efficiency of the same volume WS-PCM-TES.

Abhilash et al (2016) have investigated the thermal energy storage systems incorporating PCMs for use in a solar water heater are investigated. Since the demand for hot liquid available is inversely proportional to the availability of solar energy. Then, the system suggested incorporates PCM inside the water tank of the solar water heater to store more heat that can be utilized further. Experimentally done with a conventional solar water tank of a capacity of 60 L of an evacuated type solar water heater was modified and a cylindrical PCM tank was fabricated holding a volume of 14 liters of PCM made up of steel. Compares the results obtained from both conventional and modified PCM filled storage tanks in January 2016 at 8:30 AM and 26°C of ambient temperature. PCM box was filled with Paraffin C-32 as the PCM material which has a melting point of approximately 66 - 69°C. During charging the solar water heater for the case of without PCM, the water ran up to a temperature of more than 90°C in 105 minutes with that of PCM in 120 minutes; that is 15 minutes of time lag was found. He concludes that incorporating the paraffin used the prolonged time to which hot water was available and the PCM holds the heat till night so as to make available hot water by solar water heater during night time also. In the solar water heater, an increase in time of 220 minutes was obtained from that of PCM to without PCM.

Linga et al (2015) have investigated the performance of solar water heating systems (SWHS) that integrated with latent heat storage unit deals with variabilities of insolation. In this study, they investigated the performance of mannitol (Melting temperature $166.7℃$, enthalpy of phase change γ: $323\frac{KJ}{kg}$,) in packing solar thermal energy and generating hot water. Outcomes indicate that mannitol can accumulate high-level energy and the TES performance is affected by the inlet temperature of HTF and inlet flow rate of HTF in the tube. In this paper 14kg mass of mannitol with latent heat-activated can heat up 100L of water from 30 up to 50 o C in 6 hours is presented.

Yune (2019) has studied investigating the thermal performance of a solar water heating system integrated with phase change material as a thermal energy storage in A Case of Adama Hospital Medical College the design of flat plate solar collector and performance analysis of TES incorporating with and without phase change materials (PCM) with flat plate solar collector for use in domestic water heating purposes. The TES system holds shell and tube configuration using paraffin wax (n-Heptacosane) as PCM on the shell side and the water used as HTF on tube side to transferring heat to storage tank from solar collector.

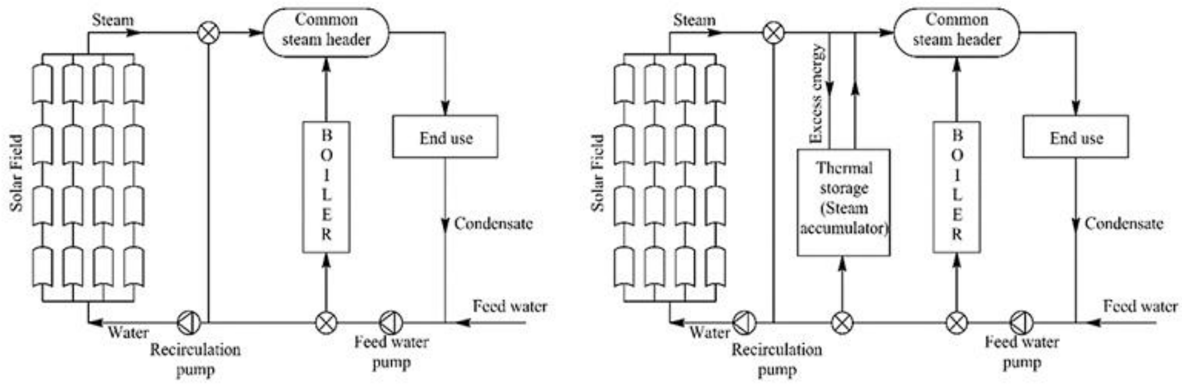

Figure 2. 7. Schematics of solar industrial process heating systems (with and without provision for thermal storage) (Sharma, 2017)

2.4.4 Steam generation using parabolic trough collector systems

Parabolic trough collectors (PTCs) are high efficient collectors commonly used in high-temperature applications to generate steam. PTCs use 3 concepts to generate steam

I. The steam-flash (pressurized hot water is flashed in a separate vessel to generate steam),

The system pressurized the water boiling. The pressurized water goes through the solar collector and eventually flashed to a flash vessel. The water level in the flash vessel is maintained at a constant level through feed water.

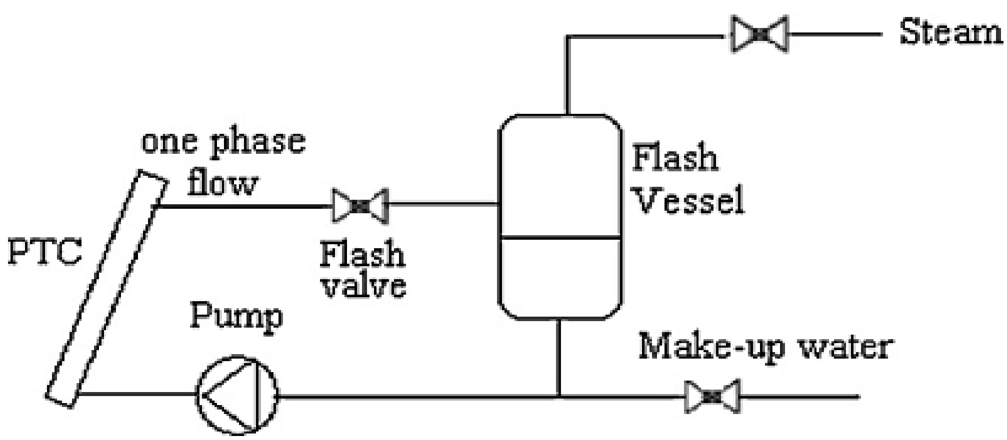

Figure 2. 8. The steam-flash generation system (Mekhilef, 2011).

I. The direct or in situ (there are 2 phase flow in the collector receiver to generate steam)

In the direct or situ boiling concept, the only difference is that flash-valve is removed in this configuration. Make-up water is directly heated to generate the steam in the receiver.

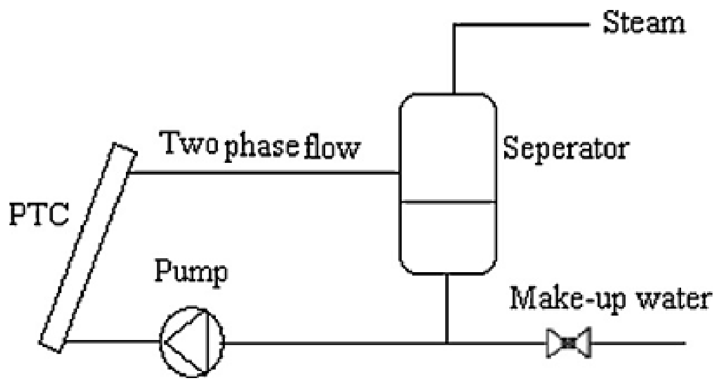

Figure 2. 9. The in situ generation system (Mekhilef, 2011).

II. The unfired-boiler (steam is generated via heat exchange in an unfired boiler).

In this concept, a heat medium fluid goes through the collector. This system is rather simple than before mentioned systems. The pressure is quite low and the control scheme is straightforward.

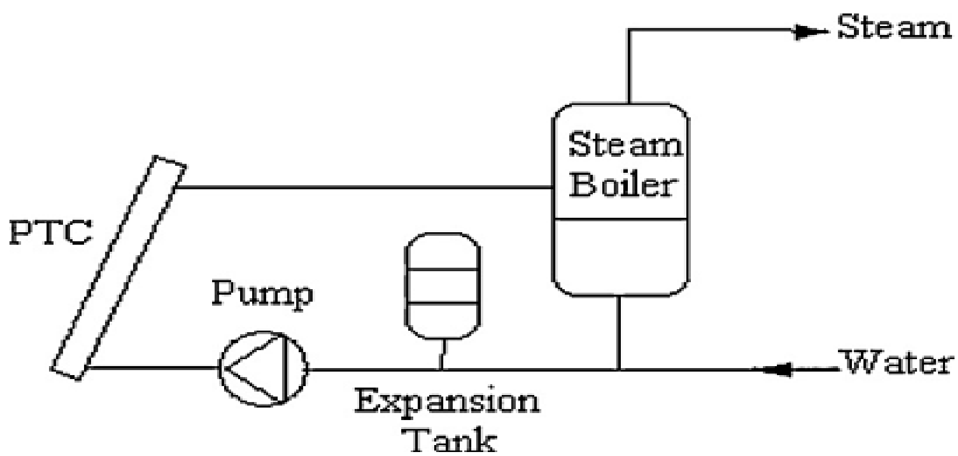

Figure 2. 10. The unfired-boiler steam generation concept.

Depending on the above literature unfired boiler steam generation concept in chosen for the Assela Malt factory.

2.5 Research Gap

In the above literature reviews, renewable energy technology is growing fast in the industry also the domestic sector. Different researchers use different solar collectors for various applications. For steam generation concentrating collectors are widely applicable. Parabolic trough solar collectors are the best choice for steam generation.

The technology of solar energy has led to the development of several solar appliances used for water heating, lighting, steam generation, and solar thermal systems. The most encouraged among them is the solar thermal system that achieves the energy necessary for different applications at domestic as well as at the industry level both for day and night time use. In solar systems, and available energy supply does not usually coincide in time with the demand and is intermittent. So, the utilization of solar energy can be more attractive and trustworthy it accompanied by a thermal energy storage system (TES). The high temperature in the kilning room is sourced from the boiler room. The boiler produces steam with a temperature of up to 160°C and is directed to the kilning room.

So solar energy as alternative thermal energy is very important for this factory in order to reduce energy consumption, parabolic trough solar steam generator incorporating with phase change material for steam supply for Malt kilning at Assela Malt factory.

CHAPTER THREE

MATERIALS AND METHODS

3.1 Methodology

This thesis is focused on the performance investigation of parabolic trough solar collectors incorporating with phase change materials for steam supply to Malt kilning at Assela Malt factory. Different literatures reviews of PTSC integrated with phase change materials are conducted. The literatures available are from journals, dissertations, and books. Mostly, the latest literature review of relevant materials on parabolic trough solar collector systems and latent heat thermal storage units was conducted. Secondary, the data are referred from related research and previous done, existing statistical information, etc. In general, the following activities were accomplished to achieve the thesis objectives.

- ✓ Data collecting from Assela Malt factory and weather data taken from Adama meteorology agency Kulumsa station.
- ✓ Estimating the steam demand for Malt kilning at Assela Malt factory
- ✓ Estimating solar beam radiation of Assela Malt factory at Kulumsa location using collected data and standards.
- ✓ Thermal modelling of the parabolic trough solar steam generator system using the data collected.
- ✓ Modeling and transient thermal performance analysis of parabolic trough solar collector.
- ✓ Design the parabolic trough solar collector integrated with PCM required to fulfill the thermal energy demand of steam supply for Malt drying.
- ✓ Numerically analyze the performance of the parabolic trough solar collector
- ✓ Study the performance of the PCM thermal energy storage integrated to the PTSC.
- ✓ Simulate the offered system and components functionally using MATLAB and Excel.
- ✓ Writing the study results with the help of graph, table, figure, number, and give the discussion of the result and final validating with the published paper.
- ✓ Finally, prepare and arrange the full paper and make a presentation.

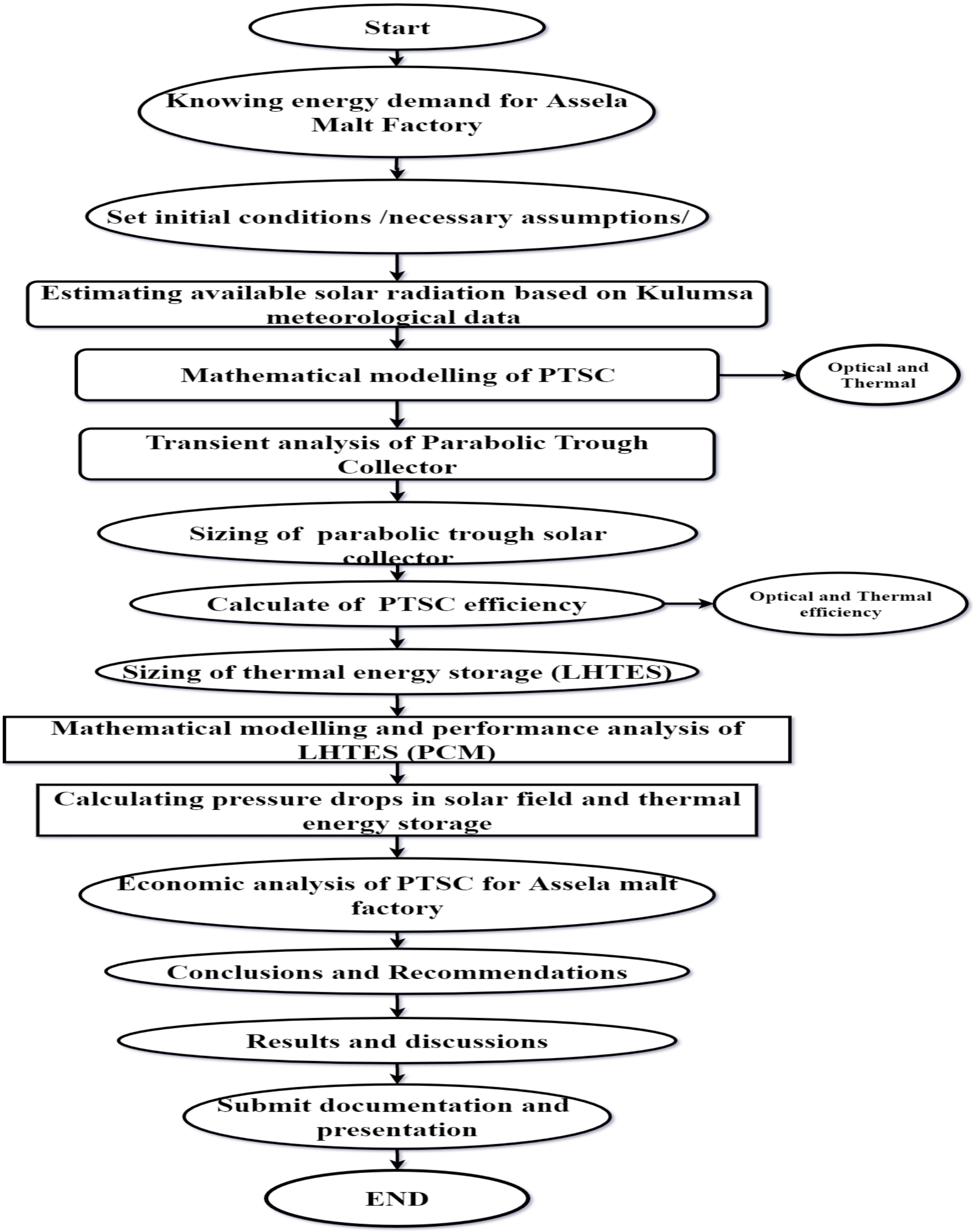

Figure 3. 1. Methodology used in this thesis

CHAPTER FOUR

SOLAR RADIATION DATA ESTIMATION

4.1 Estimation of Available Solar Radiation

Solar energy is available all around the world, especially in tropical zone. Its intensity varies significantly according to the place on the earth's surface and for the same place according to the time and the existing meteorological conditions. As a very important renewable energy source, solar radiation parameters and solar-earth angles are the most important factors for the estimation of the energy reaching the earth's surface. Developing countries like Ethiopia which has 12 months of sun shined, the solar thermal system which is an environmentally friendly and sustainable source of energy is the best alternative of energy-consuming. Ethiopia has an annual mean average solar radiation of about 5.2 kWh/m^2, and the range of 4 – 6 kWh/m^2 with an average sunlight length of more than 10 hours per day throughout the year and has a high potential for solar irradiation (UNCC, 2002).

4.2 Estimation of Global Solar Radiation Using Sunshine Duration

To estimate solar radiation the data like geographical coordinate of site, sunshine hours, and weather condition is the most important and prior requirements. Simply, Sunshine duration is the length of time that the ground surface is irradiated by direct solar radiation and is used to characterize the climate of sites (Yune, 2019).

Geographical coordinates of Assela Malt Factory, Kulumsa station: -Latitude (ϕ) of 8°2' N = 8.0141° N Longitude of 39°10’E= 39.1602°E Altitude: 2200 m above sea level. Temperature (min/max): 10°C and 22°C.

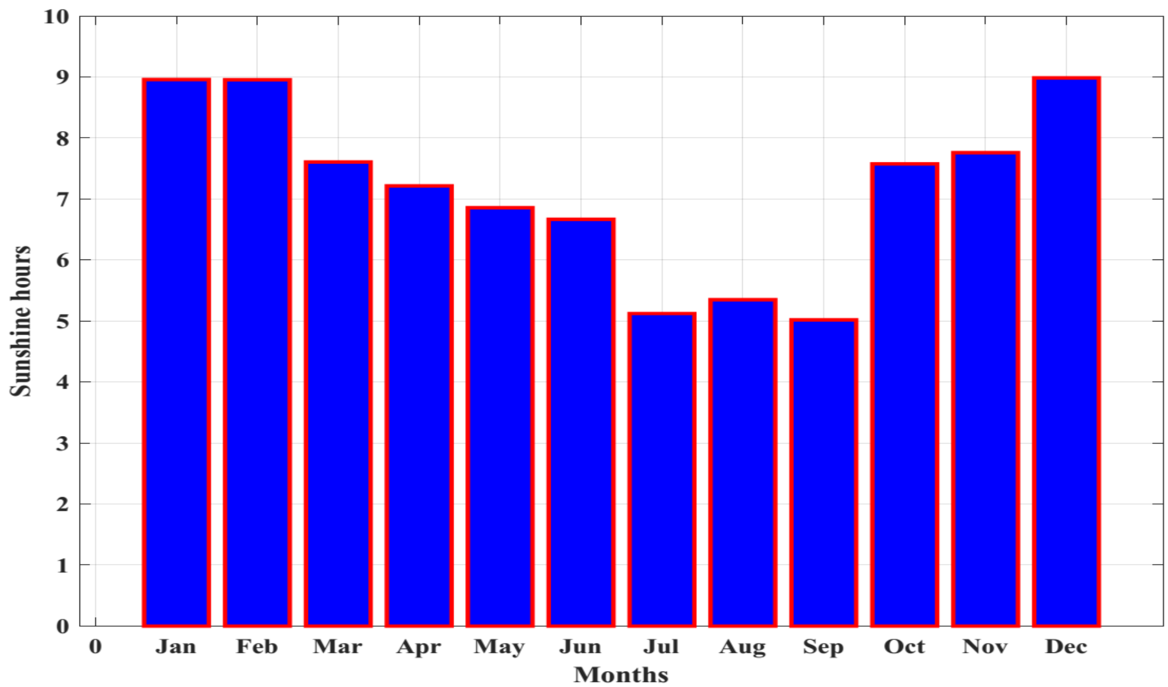

Figure 4. 1. Monthly averagely sunshine duration for each month of Kulumsa for ten years (source; East Shoa Meteorology)

Solar time: Time based on the apparent angular motion of the sun across the sky with solar noon the time the sun crosses the meridian of the observer. Solar time is the time used in all of the sun-angle relationships; it does not coincide with local clock time. It is necessary to convert standard time to solar time by applying the equation of time, which takes into account the perturbations in the earth's rate of rotation which affect the time the sun crosses the observer's meridian. The difference in minutes between solar time and standard time is:

$$\text{Solar time} - \text{Standard time} = 4(L_{st} - L_{loc}) + E \qquad (4.1)$$

Where $L_{st}$is the standard meridian for the local time zone, L_{loc} is the longitude of the location in question, and longitudes are in degrees west, that is, 0°<L<360°. The parameter E is the equation of time (in minutes) (Duffie and Beckman, 2013)

.

The parameter E is the equation of time (min) and sited (Kalogirou, 2014).

$$E = 9.87 \sin(2B) - 7.53 \cos(B) - 1.5 \sin(B) \text{ [min]} \tag{4.2}$$

$$\text{Where } B = (N - 81)\frac{360}{365} \tag{4.3}$$

Latitude (ϕ): The latitude of an observer (location) on the Earth's surface is the angle made between the radial line joining the observer (location) with the center of the Earth, and its projection on the equatorial plane ($-90° \leq \phi \leq 90°$) (Tiwari, 2016). The latitude of Assela is 7.9621° north, and Longitude 39.1284° east.

Declination angle (δ): the angular position of the sun at solar noon (i.e., when the sun is on the local meridian) with respect to the plane of the equator, north positive; $-23.45° \leq \delta \leq 23.45°$. The declination angle in degrees for any day of the year (N) can be calculated by the equation (Duffie and Beckman, 2013).

$$\delta = 23.45 \sin\left[\frac{360}{365} * (284 + N)\right] \tag{4.4}$$

Slope (β): the angle between the plane of the surface in question and the horizontal; $0° \leq \beta \leq 180°$ ($\beta > 90°$ means that the surface has a downward-facing component.)

(γ): The deviation of the projection on a horizontal plane of the normal to the surface from the local meridian, with zero due south, east negative, and west positive; ($-180° \leq \gamma \leq 180°$).

Hour angle (ω): the angular displacement of the sun east or west of the local meridian due to rotation of the earth on its axis at 15° per hour; morning negative, afternoon positive.

$$\omega = (ST - 12) * 15° \tag{4.5}$$

Where ST is the local solar time.

Angle of incidence (θ): the angle between the beam radiation on a surface and the normal to that surface.

$$\begin{aligned} \cos\theta = {} & \sin\delta\sin\phi\cos\beta - \sin\delta\cos\phi\sin\beta\cos\gamma + \cos\delta\cos\phi\cos\beta\cos\omega + \\ & \cos\delta\sin\phi\sin\beta\cos\gamma\cos\omega + \cos\delta\sin\beta\sin\gamma\sin\omega \end{aligned} \tag{4.6}$$

Zenith angle (θ_Z): the angle between the vertical and the line to the sun, that is, the angle of incidence of beam radiation on a horizontal surface.

Solar altitude angle($\boldsymbol{\alpha_S}$): the angle between the horizontal and the line to the sun, that is, the complement of the zenith angle.

$$\mathrm{Sin}\alpha_S = \sin\phi\sin\delta + \cos\phi\cos\delta\cos\omega \tag{4.7}$$

Solar azimuth angle ($\boldsymbol{\gamma_s}$): the angular displacement from south of the projection of beam radiation on the horizontal plane. Displacements east of south are negative and west of south are positive.

Sunshine hour ($\mathbf{N_S}$): The total duration in hours of the Sun's movement from sunrise to sunset. It is defined in terms of the hour angle as (Kalogirou, 2014):

$$\mathrm{N}_S = \frac{2*\omega_s}{15} \tag{4.8}$$

Where ω_s is sunset hour angle when θ_Z=90°

$$\mathrm{Cos}\omega_s = -\tan\phi * \tan\delta \tag{4.9}$$

$$\mathrm{N}_S = \frac{2}{15}\cos^{-1}(-\tan\phi * \tan\delta) \tag{4.10}$$

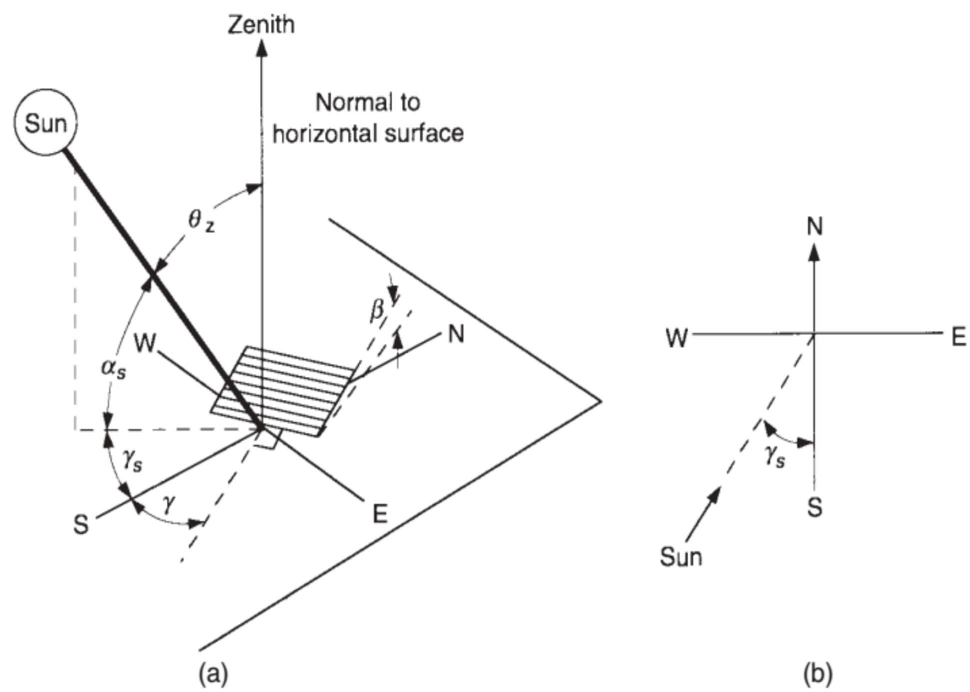

Figure 4. 2. (a) Zenith angle, slope, surface azimuth angle, and solar azimuth angle for a tilted surface. (b) Plan view showing solar azimuth angle (Duffie and Beckman, 2013).

Table 4. 1. Recommended average days for months and values of n by months(Duffie and Beckman, 2013).

Month	n for ith Day of Month	For Average Day of Month		
		Date	n	δ
January	i	17	17	−20.9
February	$31 + i$	16	47	−13.0
March	$59 + i$	16	75	−2.4
April	$90 + i$	15	105	9.4
May	$120 + i$	15	135	18.8
June	$151 + i$	11	162	23.1
July	$181 + i$	17	198	21.2
August	$212 + i$	16	228	13.5
September	$243 + i$	15	258	2.2
October	$273 + i$	15	288	−9.6
November	$304 + i$	14	318	−18.9
December	$334 + i$	10	344	−23.0

4.3 Extraterrestrial Radiation on a Horizontal Surface

The extraterrestrial radiation measured on the plane normal to the radiation on the nth day of the year for a whole year can be calculated by. (Kalogirou, 2014).

$$\overline{H}_o = G_{sc}(1 + 0.033 \cos \frac{360n}{365}) \tag{4.11}$$

Where $\overline{H}_o$ extraterrestrial radiation measured on the plane normal to the radiation on the nth day of the year (${W}/{m^2}$). G_{sc} The solar constant, 1367 ${W}/{m^2}$ and n is the day of the year.

Solar constant: The amount of solar energy per unit time, at the mean distance of the earth from the sun, received on a unit area of a surface normal to the sun (perpendicular to the direction of propagation of the radiation) outside the atmosphere.

The extraterrestrial solar radiation incident on a horizontal surface placed parallel to the ground outside of the atmosphere given by (Kalogirou, 2014):

$$\overline{H}_o = G_{sc}(1 + 0.033 \cos \frac{360n}{365}) (\cos\delta\cos\phi\cos\omega + \sin\delta\sin\phi) \tag{4.12}$$

The extraterrestrial solar radiation incident on a horizontal surface of Assela Malt factory at by using Kulumsa metrology station data.

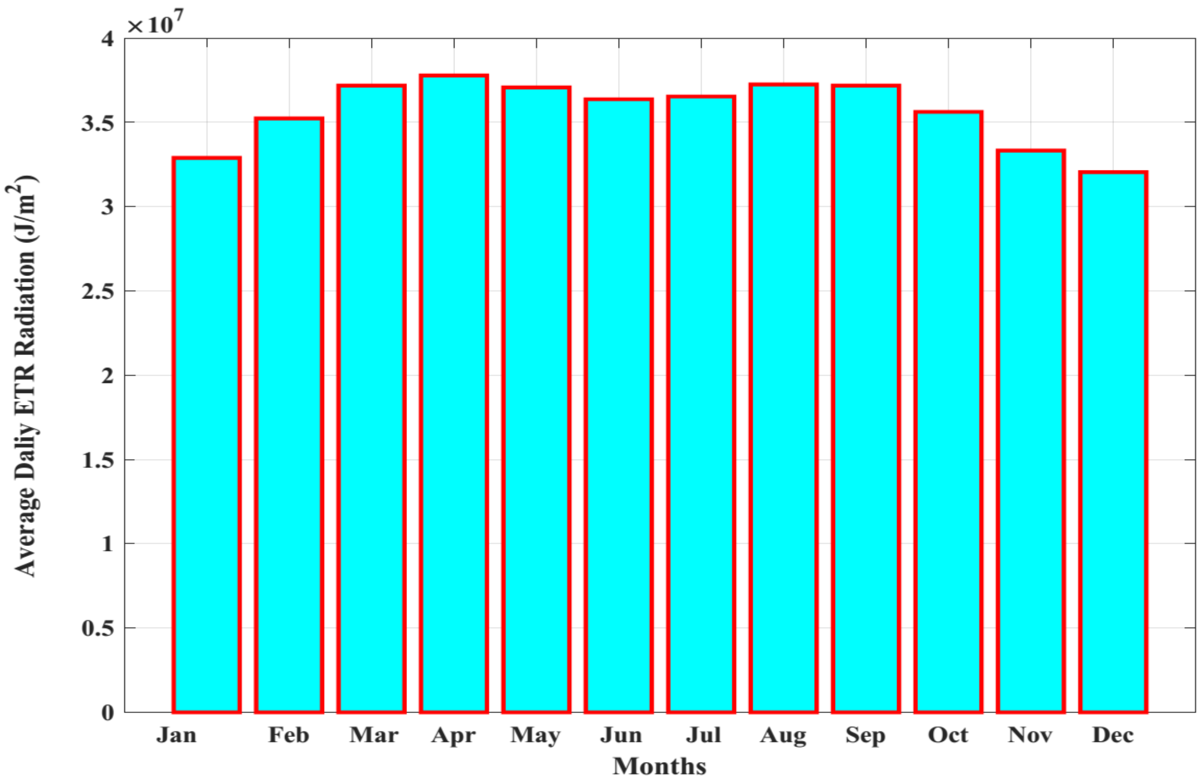

Figure 4. 3. The solar radiation incident on a horizontal plane outside of the atmosphere (Extraterrestrial (ETR) daily Solar Radiation

4.3.1 Prediction of Monthly Average Daily Global Radiation on a Horizontal Surface

The first empirical correlation using the idea of employing sunshine hours for the estimation of global solar radiation was proposed by Angstrom. The Angstrom correlation was modified by Prescott and Page. The simplest model used to estimate monthly average daily solar radiation on a horizontal surface is the well-known Angstrom equation (Duffie and Beckman, 2013).

$$\frac{\bar{H}}{\bar{H}_o} = \mathrm{a} + \mathrm{b}\left(\frac{\bar{n}_S}{\bar{N}_S}\right) \qquad (4.13)$$

Where $\bar{H}$ - Monthly average daily radiation on a horizontal surface (Global radiation).

$\bar{H}_o$ - Monthly average radiation outside of the atmosphere (extraterrestrial, ETR on the horizontal surface) for the same location (W/m^2).

a, b – empirical constants.

$\bar{n}_s$ - Monthly average daily hours of bright sunshine (sunshine hour).

$\bar{N}_s$ - Monthly average of the maximum possible daily hours of bright sunshine.

The regression parameters a and b can be determined from; -

$$a = -0.11 + 0.235\cos\phi + 0.323\left(\frac{\bar{n}_s}{\bar{N}_s}\right) \quad (4.14)$$

$$b = 1.449 - 0.533\cos\phi - 0.694\left(\frac{\bar{n}_s}{\bar{N}_s}\right) \quad (4.15)$$

$\bar{H}_o$ Can be obtained by the Klein relationship:

$$\bar{H}_o = \frac{24*3600*G_{sc}}{\pi}\left(1 + 0.033\cos\frac{360n}{365}\right)\left(\cos\phi\cos\delta\cos\omega_s + \frac{\pi*\omega_s}{180}\sin\phi\sin\delta\right) \quad (4.16)$$

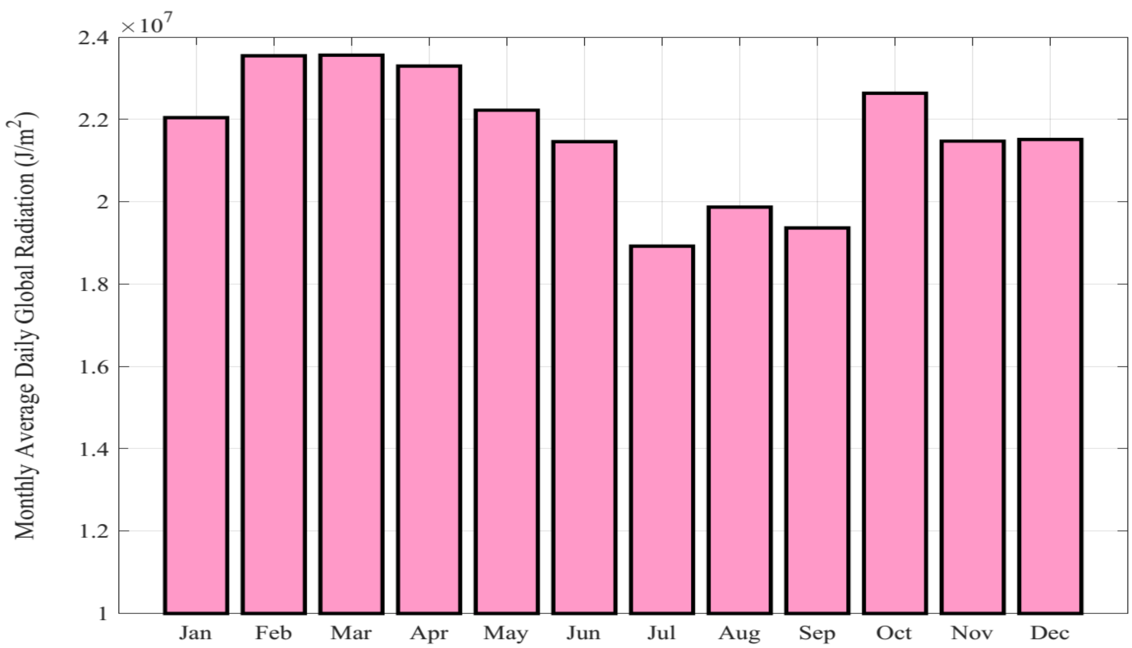

Figure 4. 4. Monthly average daily global radiation on horizontal surface of Kulumsa – Assela

4.3.2 Prediction of Monthly Average Daily Diffuse Radiation on a Horizontal Surface

The monthly average daily diffuse radiation on a horizontal surface can be determined from the monthly average daily global radiation on a horizontal surface and the number of bright sunshine hours (Duffie and Beckman, 2013).

$$\frac{\overline{H}_d}{\overline{H}} = 0.931 - 0.814(\frac{\overline{n}_s}{\overline{N}_s}) \quad (4.17)$$

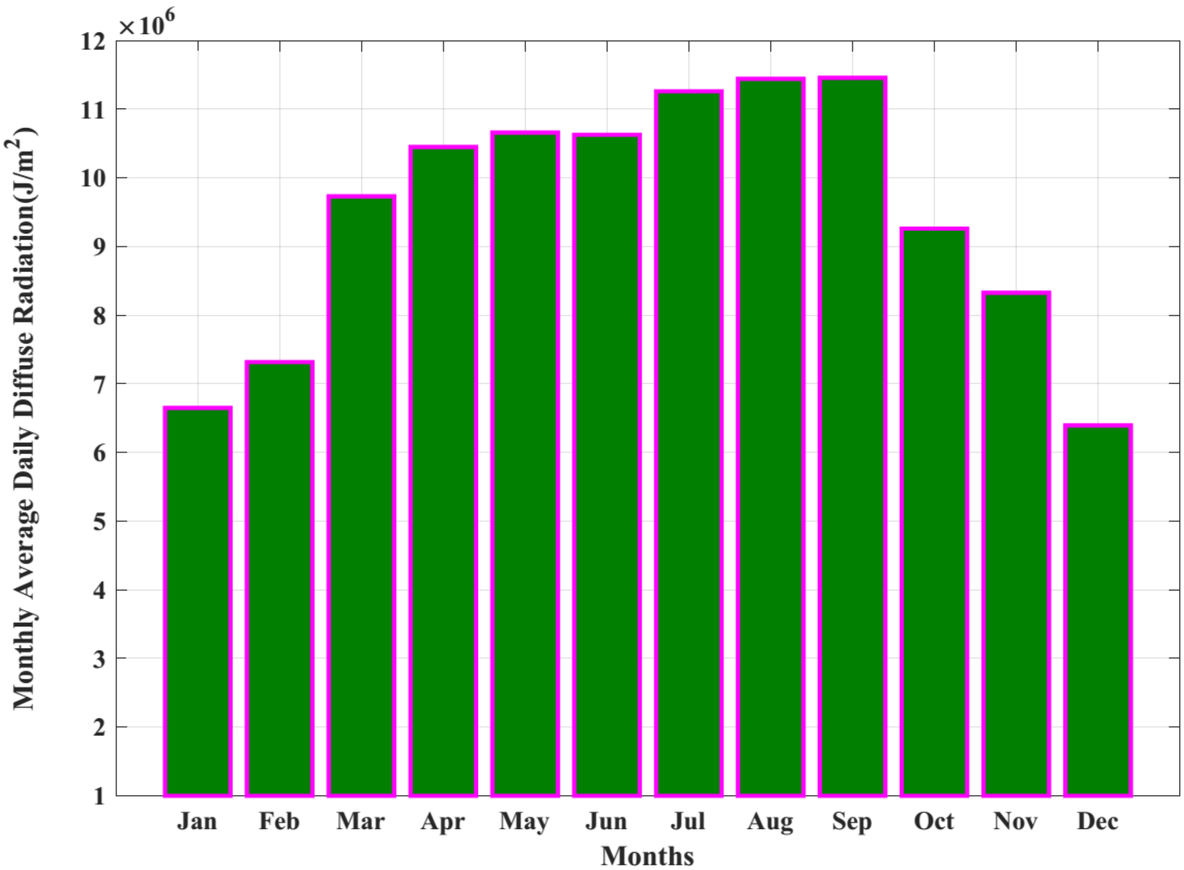

Figure 4. 5. Graph of monthly average daily diffuse radiation on a horizontal surface

Monthly Average daily beam radiation on horizontal surface calculated as follow (Reta, 2020):

$$\overline{H}_b = \overline{H} - \overline{H}_d \quad (4.18)$$

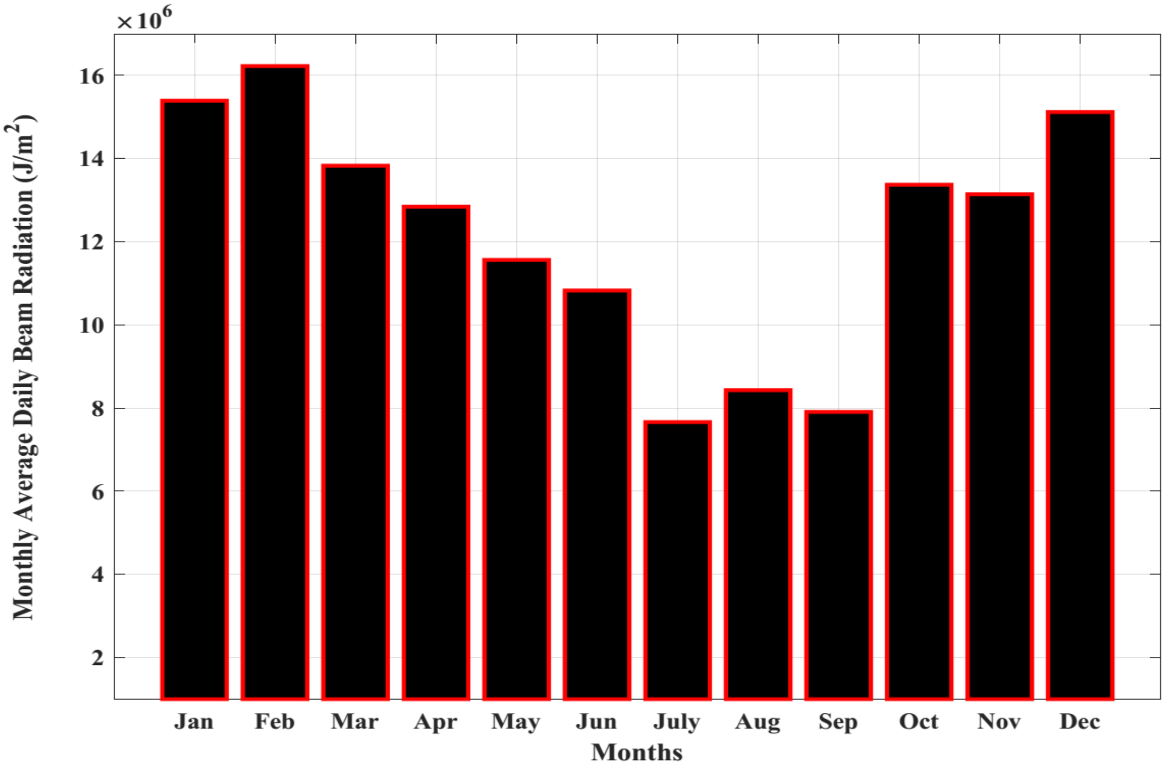

Figure 4. 6. Graph of monthly average daily beam radiation on a horizontal surface of Kulumsa.

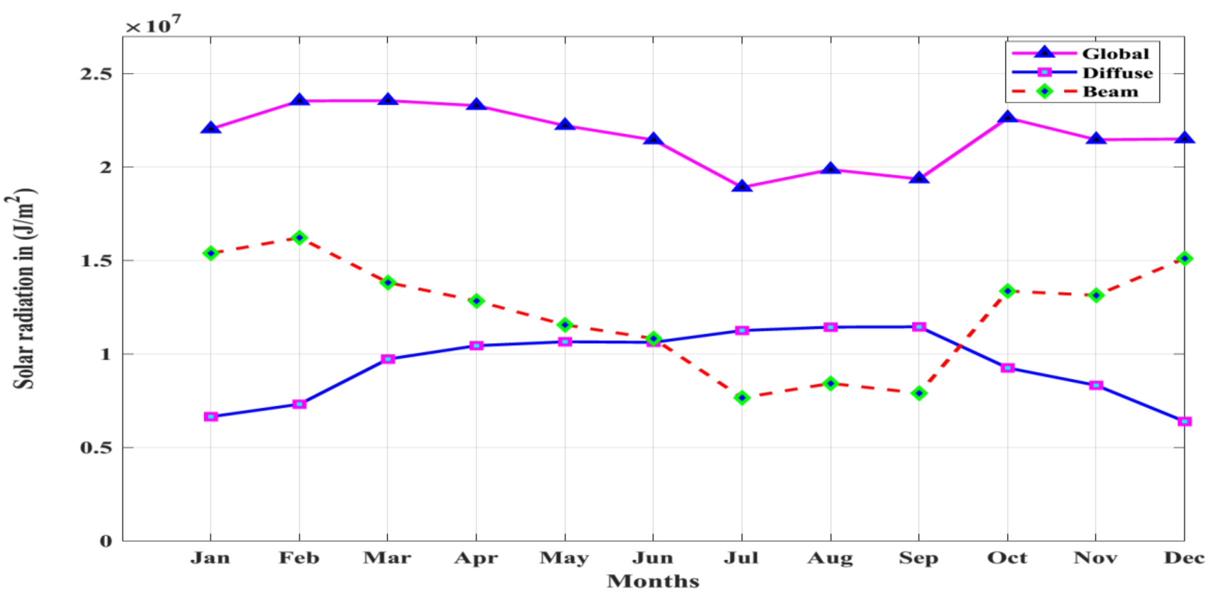

Figure 4. 7. Graph of monthly average daily global, diffuse and beam radiation on a horizontal surface

4.3.3 Prediction of Monthly Average Hourly Global Radiation on a Horizontal Surface (*I*)

The monthly average hourly global radiation on a horizontal surface can be calculated from the knowledge of the monthly average daily global radiation on a horizontal surface, Dincer et al., (2007). The total hourly solar radiation falling on a horizontal surface, I in W.h/m, could be estimated from the daily global radiation, H (in kJ/m^2 per day) in accordance with (Duffie and Beckman, 2013).

$$\frac{\bar{I}}{\bar{H}} = \frac{\pi}{24}(a + b\cos\omega)\frac{\cos\omega - \cos\omega_s}{\sin\omega_s - \frac{\pi\omega_s}{180}\cos\omega_s} \qquad (4.19)$$

Where

$$a = 0.409 + 0.5016\sin(\omega_s - 60) \qquad (4.20)$$

$$b = 0.6609 - 0.4767\sin(\omega_s - 60) \qquad (4.21)$$

4.3.4 Prediction of Monthly Average Hourly Diffuse Radiation on a Horizontal Surface

The monthly average hourly diffuse radiation on a horizontal surface can be calculated from the knowledge of the monthly average daily diffuse radiation on a horizontal surface.

$$\frac{\bar{I}_d}{\bar{H}_d} = \frac{\pi}{24}\frac{\cos\omega - \cos\omega_s}{\sin\omega_s - \frac{\pi\omega_s}{180}\cos\omega_s} \qquad (4.22)$$

Monthly average hourly beam solar irradiance on a horizontal surface

$$\bar{I}_b = \bar{I} - \bar{I}_d \qquad (4.23)$$

4.3.5 Prediction of Hourly Variation of Temperature

In the design and simulation of parabolic trough solar collector atmospheric temperature is one of the needed inputs. The hourly difference of outdoor temperature is assessed by a mathematical model that uses the minimum and maximum temperatures of the day. The day-to-day ambient temperature can be determined by via (Bellos et al., 2017):

$$T_{am} = T_{am,min} + \frac{DR}{2}\cos(2\pi * \frac{(t_h - t_{h,max})}{24}) \qquad (4.24)$$

Where $T_{am,min}$ - mean daily temperature of the day.

DR is the daily range temperature of the day

t_h- is the time of the day

$t_{h,max}$ - time for the occurrence of daily maximum temperatures

It assumed that the ambient temperature is usually maximized at 14:00 and thus the parameter, $t_{h,max}$ is selected to be equal to 14 h (Bellos et al., 2017).

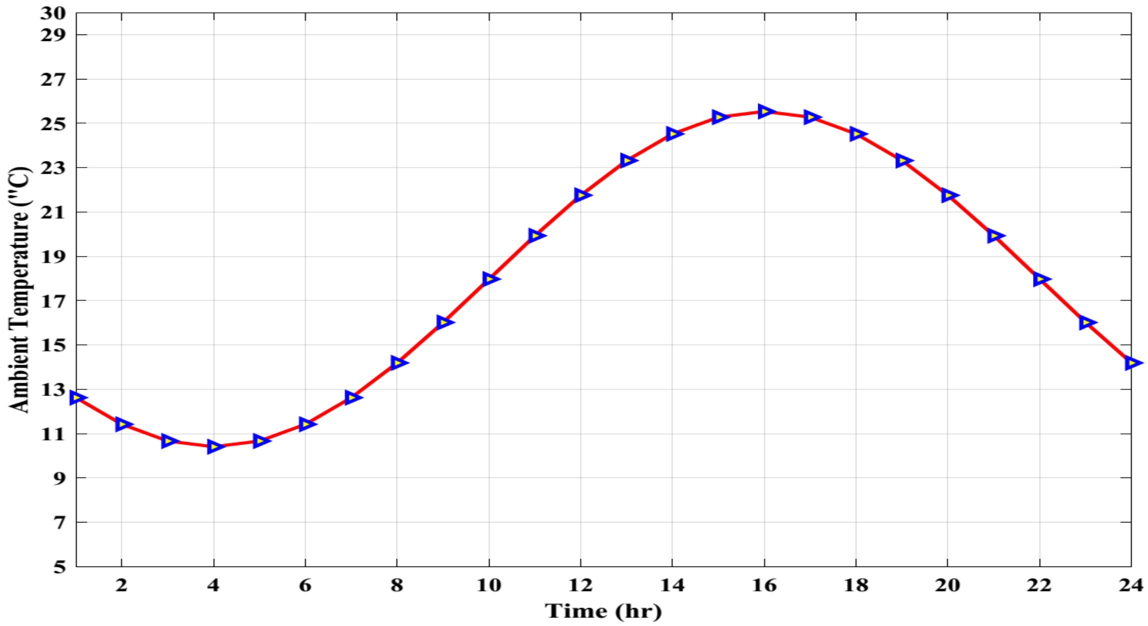

Figure 4. 8. Hourly variation of ambient temperature in (℃) for February 16

CHAPTER FIVE

MODELING OF PARABOLIC TROUGH SOLAR COLLECTOR

The concentrating technologies can operate at higher temperature levels and they are usually used in temperature levels between 150-500℃. The parabolic trough solar collector (PTC) is the most mature solar concentrating technology at this moment. The PTC usually operates with thermal oils as Syltherm 800, Therminol VP-1, Therminol 55, Dowtherm A, etc for operation up to 400℃. Moreover, they can operate with water/steam for electricity production in Rankine cycles. Furthermore, there are applications with molten salts as work fluids and especially nitrate salts which can operate up to 550~600℃ (Bellos, 2018).

The conventional PTC consists of a linear parabolic shape concentrator, a linear tubular receiver, and a metallic support structure. The PTC tracks the sun usually with a single axis mechanism for the solar rays to be properly in the collector aperture.

The receiver of the conventional PTC is an evacuated tube receiver with a metallic inner tube (the absorber) and an outer glass tube (the cover). Usually, there are vacuum conditions between the absorber and the cover in order to eliminate the convection thermal losses of the absorber.

5.1 Basic Mathematical Modeling of the Conventional PTC

Parabolic troughs concentrate the incident direct irradiance on its focal line. In a cross-section view, an asymmetric parabola around its vertex is visible and the focus is reduced onto a point. An analytical representation of the parabola is given as follows (Chaves, 2019):

$$\mathrm{y} = \frac{1}{4 * f} x^2 \tag{5.1}$$

f: focal length [m]

Moreover, four important parameters characterize the collector's geometry: aperture width a, aperture length l, focal length, and rim angle ψ.

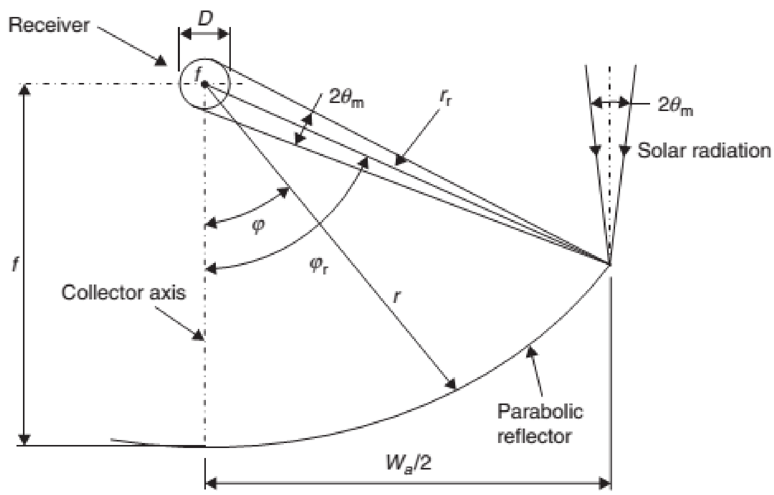

Figure 5. 1. Cross-section of a parabolic trough collector with the circular receiver (Kalogirou, 2014)

The rim angle (φ_r): is the angle between the optical axis and the line between the focal point and the mirror rim, has the interesting characteristics that it alone determines the shape of the cross-section of a parabolic trough. That means that the cross-sections of parabolic troughs with the same rim angle are geometrically similar (Gunther, 2011).

Rim angle (φ_r) is calculated using the aperture (W) and the focal distance (f) as below (Bellos, 2018):

$$\varphi_r = \tan^{-1}\left[\frac{8 * \frac{f}{W}}{16 * \left(\frac{f}{W}\right)^2 - 1}\right] \tag{5.2}$$

The total collector aperture (A_a)is the product of the width (W) and the length (L)

$$A_a = \mathrm{W.L} \tag{5.3}$$

The surface area of a parabolic trough may be important to determine the material need for the trough. The area is calculated as follows:

$$\mathrm{A} = \left(\frac{W}{2}\sqrt{1+\frac{W^2}{16f^2}} + 2f * \ln\left(\frac{a}{4f} + \sqrt{1+\frac{W^2}{16f^2}}\right)\right) * \mathrm{L} \tag{5.4}$$

The absorber area (A_{ro}) is the outer area of the tube:

$$A_{ro} = \pi . D_{ro} . \mathrm{L} \tag{5.5}$$

The concentration ratio (C): is defined as the ratio collector aperture to the receiver (absorber) area. which are the factors increasing the radiation flux on the energy-absorbing surface (Bellos, 2018).

$$C = \frac{A_a}{A_{ro}} = \frac{W * L}{\pi . D_{ro} . L} = \frac{W}{\pi . D_{ro}} \tag{5.6}$$

Table 5. 1. LS-2 parabolic trough collector tested in Sandia. The geometrical characteristics of the absorber tubes (Lamrani & Draoui, 2018).

Geometric characteristic	Value
Mirror length (L)	5 m
Mirror width (W)	3.4 m
Focal length (f)	1.84 m
Internal diameter of the absorber(D_{ri})	0.066 m
External diameter of the absorber(D_{ro})	0.070 m
Internal diameter of the glass(D_{gi})	0.109 m
External diameter of the glass(D_{go})	0.115 m
Reflected surface reflectivity (ρ_m)	0.93
Transmissivity of the glass(τ)	0.95
Absorptance coefficient of absorber tube (α)	0.94
The emissivity of the absorber tube (ε_r)	0.24
The emissivity of the glass (ε_g)	0.86
Shape factor (γ)	0.92
Incident angle modifier K(θ)	1

5.2 Optical Modeling

The size of the receiver (diameter D) required to intercept all the solar image can be obtained from trigonometry is given by (Kalogirou, 2014):

$$\mathrm{D} = 2r_r \sin\theta_m \tag{5.7}$$

Where θ_m- half acceptance angle (degrees)

$$r_r = \frac{2f}{1+\cos\varphi_r} \tag{5.8}$$

For a parabolic reflector, the radius, r, is given by

$$r = \frac{2f}{1+\cos\varphi} \tag{5.9}$$

φ - Angle between the collector axis and a reflected beam at the focus

The aim of optical analysis of the sun rays is to specify the thermal output of the examined collector. In ideal conditions, the concentrators reflect all of the incident solar energy. However, in reality, there is no perfect reflection of solar radiation due to the presence of optical losses. The Optical performance of PTCs depends on factors such as tracking error, geometric error, and technical failure (Reta, 2020).

The energy balance on the absorber indicates that the absorbed solar irradiation (Q_{abs}) is separated into useful heat (Q_u) and thermal losses (Q_{loss}):

$$Q_{abs} = Q_u . Q_{loss} \tag{5.10}$$

The absorbed solar energy (Q_{abs}) is calculated using the optical efficiency of the solar collector (η_{opt}) and the available solar irradiation (Q_s).

$$Q_{abs} = \eta_{opt} . Q_s \tag{5.11}$$

Optical efficiency is defined as the ratio of the energy absorbed by the receiver to the energy incident on the collector's aperture.

The optical efficiency depends on the optical properties of the materials involved, the geometry of the collector, and the various imperfections arising from the construction of the collector (Kalogirou, 2014).

The optical efficiency changes with the incident angle and it can be modeled using the incident angle modifier (K) and the maximum optical efficiency ($\eta_{opt,max}$) which is observed for zero-incident angle:

$$\eta\_opt = K(\theta).\eta\_(opt,max) \tag{5.12}$$

The incident angle modifier is a function of the geometric characteristics of the PTC, as well as of the incident angle (θ). The equation is applied for temperatures between ambient and 400℃, at any insolation level from 100 to 1100 W/m^2, and at any incident angle from 0 to 90 degrees.

$$\mathrm{K}(\theta) = \cos(\theta) + 0.0003178(\theta) + 0.00003985(\theta)^2 \tag{5.13}$$

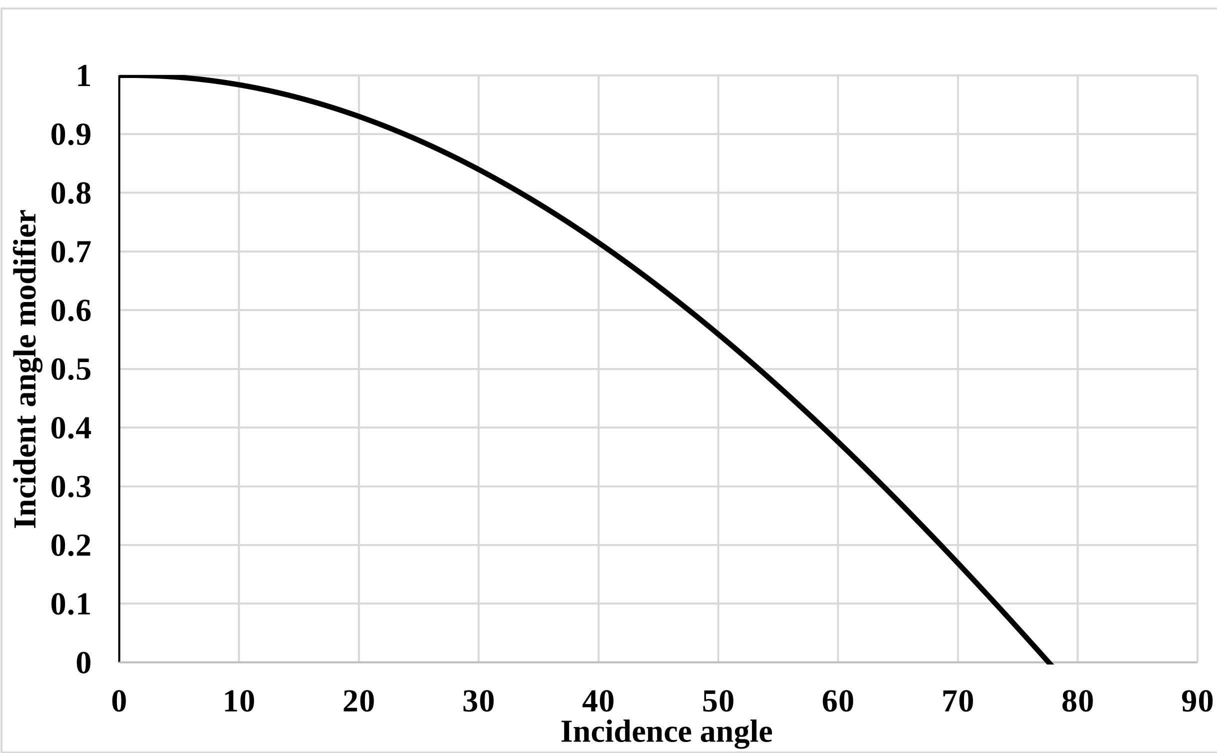

Figure 5. 2. Incident angle modifier for incidence angle 0-90 degree

The maximum optical efficiency ($\eta_{opt,max}$) is a product of various parameters. Every parameter regards a different optical loss. The absorber absorbance (α), the cover transmittance (τ), the intercept factor (γ), and the total reflectance (ρ_{tot}.) are the used parameters in the maximum optical efficiency calculation.

$$\eta_{opt,max} = \rho_{tot}.\gamma.\tau.\alpha \tag{5.14}$$

$$= 0.93*0.92*0.95*0.94$$

$$\boldsymbol{\eta_{opt,max}} \mathbf{= 0.764 = 76.4\%}$$

5.3 Thermal Modeling

The collector performance model uses an energy balance between the fluid flowing through the receiver, usually a heat transfer fluid (HTF), and the atmosphere. It includes all equations necessary to predict the various expressions of the energy balance, which depend on the ambient conditions and the collector receiver optical properties and condition (Kalogirou, 2012).

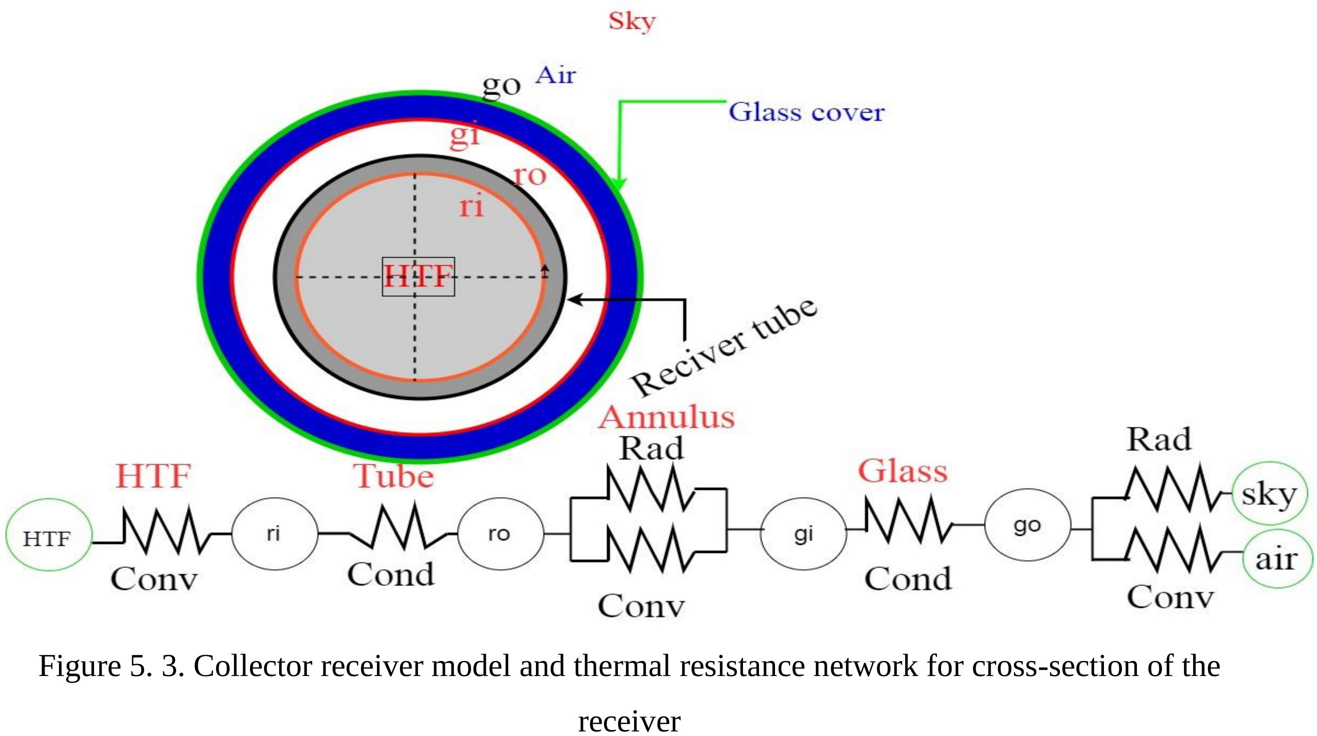

Figure 5. 3. Collector receiver model and thermal resistance network for cross-section of the receiver

The energy balance equations are determined by considering that the energy is conserved at each surfaces of the receiver cross section on the figure above.

Therefore

$$q_{\mathrm{f-ri,conv}} = q_{\mathrm{ri-ro,cond}}$$

$$q_{\mathrm{ro-sol\ Abs}} = q_{\mathrm{ro-ci,conv,}} + q_{\mathrm{ro-ci,rad}} + q_{\mathrm{ri-ro,cond}}$$

$$q_{\mathrm{ro-ci,conv}} + q_{\mathrm{ro-ci,rad}} = q_{\mathrm{ci-co,cond}} \tag{5.15}$$

$$q_{\mathrm{ci-co\ cond}} + q_{\mathrm{co-sol\ Abs}} = q_{\mathrm{co-amb,conv}} + q_{\mathrm{co-sky,rad}}$$

$$q_{\mathrm{Heat\ loss}} = q_{\mathrm{co-amb,conv}} + q_{\mathrm{co-sky,rad}}$$

The thermal model was developed based on the heat transfer process that occurs in the heat collection element (HCE) or Receiver. The useful heat production of a PTC (Q_u) can be calculated using the energy balance on the fluid volume:

$$Q_u = m.C_p.(T_{out} - T_{in}) \tag{5.16}$$

The thermal losses of the solar collector (Q_{loss}) can be expressed as below, using the thermal loss coefficient (U_L) and the mean absorber temperature (T_r) (Bellos, 2018):

$$Q_{loss} = A_{ro} * U_L * (T_r - T_{am}) \tag{5.17}$$

The thermal losses of the absorber to the cover

Heat transfer between the absorber tube and the cover occurs by convection and radiation mechanism.

Convection heat transfer

$$q_{ro-ci,cv} = h_{cv,int}(T_c - T_r) \tag{5.18}$$

Where, $h_{cv,int}$is estimated through natural convection relations between two horizontal, concentric cylinders and given by (Kalogirou, 2012):

$$h_{cv,int} = \frac{2\pi k_{eff}}{\ln \frac{D_{ci}}{D_{ro}}} \tag{5.19}$$

The effective thermal conductivity k_{eff} is given by (Kalogirou, 2012):

$$k_{eff} = 0.36 k_{air} (\frac{P_{r\,air}}{0.861 + P_{r\,air}})^{0.25} (R_{ac})^{0.25} \quad (5.20)$$

Where

$$R_{ac} = \frac{(\ln(\frac{D_{ci}}{D_{ro}}))^4}{{L_{eff}}^3 ({D_{ci}}^{-0.6} + {D_{ro}}^{-0.6})^5} (G_{r\,air} - P_{r\,air}) \quad (5.21)$$

The critical length is given by

$$L_{eff} = \frac{D_{ci} - D_{ro}}{2} \quad (5.22)$$

Radiation Heat Transfer

The radiation heat transfer between the receiver tube and glass cover is estimated by (Reta, 2020).

$$q_{ro-ci,rad} = \pi D_{ro}\, h_{rad,int} (T_r - T_c) \quad (5.23)$$

$$h_{r,int} = \frac{\sigma ({T_r}^2 + {T_c}^2) * (T_r - T_C)}{\frac{1}{\varepsilon_r} + \frac{1 - \varepsilon_c}{\varepsilon_c} (\frac{D_{ro}}{D_{ci}})} \quad (5.24)$$

Conduction heat transfer through the receiver tube wall

Conduction heat transfer through the receiver tube wall is determined by Fourier's law of conduction through a hollow cylinder with the assumption that there is no thermal resistance and the thermal conductivity of the glass is constant (Kalogirou, 2012).

$$q_{ri-ro\,cond,} = \frac{2\pi k_r (T_{ri} - T_{ro}))}{\ln(\frac{D_{ro}}{D_{ri}})} \quad (5.25)$$

Where k_r is receiver tube thermal conductivity of receiver tube at the average temperature $\frac{T_{ri} + T_{ro}}{2}$ (W/m°C). The thermal losses of the absorber to the cover are practically radiation thermal losses of the absorber to the cover (Bellos, 2018).

$$Q_{loss} = A_{ro}.\sigma.\frac{T_r^{\ 4} - T_c^{\ 4}}{\frac{1}{\varepsilon_r} + \frac{1-\varepsilon_c}{\varepsilon_c} * \frac{A_{ri}}{A_{co}}} \quad (5.26)$$

Heat transfer between the HTF and the receiver tube

From Newton's law of cooling the convection heat transfer from the inside surface of the receiver tube to the HTF is given by (Kalogirou, 2012):

$$q_{f-ri\ conv,} = \pi D_{ri}\, h_{conv,f}(T_{ri} - T_f) \quad (5.27)$$

The convection heat transfer coefficient at the inside pipe diameter (Mesfin, 2009)

$$h_{conv,f} = N_{u,f}\,\frac{k_f}{D_{ri}} \quad (5.28)$$

The Nusselt number depends on the type of flow through the receiver pipe. When the Reynolds number is lower than 2300, laminar flow exists in the receiver pipe and the Nusselt number is constant. For pipe flow, the constant value, assuming constant heat flux, as in the case of a PTC, is equal to 4.36.

Turbulent and transitional cases occur at Reynolds number > 2300. Therefore, the following Nusselt number correlation developed by Gnielinski is used for the convective heat transfer from the receiver pipe to the HTF (Kalogirou, 2012):

$$\text{For } R_{e,f} < 2300, \qquad N_{u,f} = 4.36 \quad (5.29)$$

$$\text{For } R_{e,f} > 2300,\ N_{u,f} = \frac{\frac{f}{8}(R_{e,f} - 1000)P_{r,f}}{1 + 12.7(P_{r,f}^{\frac{2}{3}} - 1)\sqrt{\frac{f}{8}}}\left(\frac{P_{r,f}}{P_{r,a}}\right)^{0.11} \quad (5.30)$$

$$\text{f} = [0.79 \ln R_{e,f} - 1.64]^{-2} \quad (5.31)$$

Where $N_{u,f}$Nusselt number based on the inside diameter of the tube is D_{ri} is the inside diameter of the tube (Mesfin, 2009)

$$N_{u,f} = 0.023 R_{e,f}^{\ 0.8} P_{r,f}^{\ n} \quad (5.32)$$

Where: n = 0.4 for heating ($T_r > T_f$) and 0.3 for cooling ($T_r < T_f$).

$$R_{e,f} = \frac{4 * \dot{m}}{\pi D_{ri} \mu_f} \tag{5.33}$$

μ_f as the viscosity of the HTF

$$P_{r,f} = \frac{v_f}{\alpha_f} \tag{5.34}$$

Where $P_{r,f}$ - The Prandtl number v_f- The kinematic viscosity of the HTF

α_f - The thermal diffusivity of HTF

$$v_f = \frac{\mu_f}{\rho_f} \text{ and } \alpha_f = \frac{k_f}{\rho_f C_f} \tag{5.35}$$

The HTF properties, $\alpha_f, v_f, \rho_f, C_f, k_f$ are functions of the HTF film temperature T_f.

The thermal losses of the cover to the ambient

The thermal losses of the cover to the ambient are assumed to be the same as the thermal losses of the absorber to the cover because the system is evaluated in steady-state conditions. There are both radiation and concentration thermal losses from the cover to the ambient.

$$Q_{loss} = A_{ro}.\sigma.({T_c}^4 - {T_{sky}}^4) + A_{co}.h_{out}.(T_c - T_{am}) \tag{5.36}$$

The sky temperature can be estimated by the following equation

$$T_{sky} = 0.0552{T_{am}}^{1.5} \tag{5.37}$$

The heat transfer coefficient between cover and ambient (h_{out}) can be calculated using the following formula (Bellos, 2018).

$$h_{out} = 4.{V_{wind}}^{0.58}.{D_{co}}^{-0.48} \tag{5.38}$$

Collector heat removal factor

The heat removal factor represents the ratio of the actual useful energy gain that would result if the collector-absorbing surface had been at the local fluid temperature. In Equation form, this is given by (Kalogirou, 2012).

$$F_R = \frac{\dot{m}C_p}{A_r U_L}[1 - \exp(\frac{-A_r U_L F'}{\dot{m}C_p})] \tag{5.39}$$

A_r- The receiver area (m^2)

F' - The collector efficiency factor

$$F' = \frac{1/U_L}{1/U_L + \frac{D_{ro}}{h_{fi}D_{ri}} + \frac{D_{ro}}{2K_f}\ [\ln(\frac{D_{ro}}{D_{ri}})]} \tag{5.40}$$

Where

$K_f -$ is the thermal conductivity of the working fluid (W/m K),

$D_{ri} -$ is receiver tube inner diameter

$D_{ro} -$is receiver tube outer diameter

$h_{fi} -$is convective heat transfer coefficient inside the receiver tube [W/m2K] and

$U_L -$is the thermal loss coefficient and given by

$$U_L = [\frac{A_r}{(h_{conv,ext} + h_{rad,ext})A_c} + \frac{1}{h_{rad,int}}]^{-1} \tag{5.41}$$

The useful heat production of a PTC (Q_u) can be calculated using the energy balance on the fluid volume:

$$Q_u = m.C_p.(T_{out} - T_{in}) \tag{5.42}$$

$$Q_u = F_R A_a[\eta_o I_b - U_L(\frac{T_{f\ in} - T_{amb}}{C})] \tag{5.43}$$

The available solar irradiation on the collector aperture (Q_s) is the product of the unshaded aperture area (A_a) and of the direct beam solar irradiation (I_b):

$$Q_s = A_a * I_b \tag{5.44}$$

Where $A_a = \pi(W_a - D_{ro})$ L

The thermal efficiency of the solar collector (η_{th}) is the ratio of the useful heat (Q_u) to the available solar direct beam irradiation (Q_s):

$$\eta_{th} = \frac{Q_u}{Q_s} \tag{5.45}$$

The temperature outlet is described as

$$T_{f\ out} = T_{amb} + \frac{C\eta_o I_b}{U_L} + (T_{f\ in} - T_{amb} - \frac{C\eta_o I_b}{U_L}).\exp\left(\frac{-A_r U_L F'}{\dot{m}C_p}\right) \tag{5.46}$$

$$T_{f\ out} = T_{f\ in} + \frac{\eta_o A_a\ I_b}{\dot{m}C_p} \tag{5.47}$$

The average solar beam radiation of Assela-Kulumsa solar radiation in each time of a year is around 302.84W/m^2. So at to get outlet temperature of PTSC at Assela 0.05kg/s mass flow rate of HTF is required.

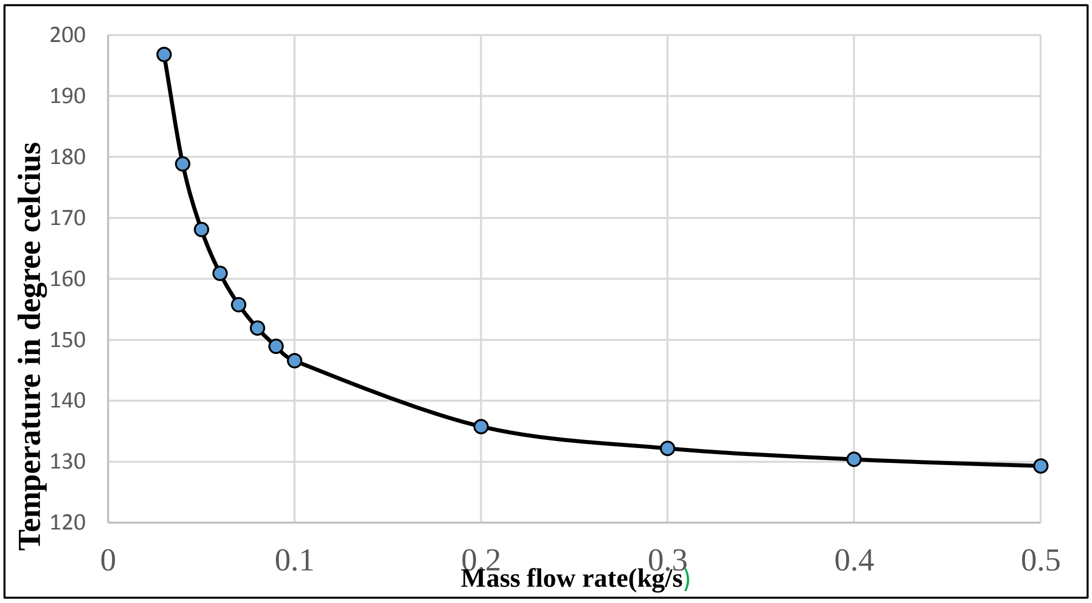

Figure 5. 4. Mass flow rate versus temperature in degree Celsius

5.4 Transient Analysis of Parabolic Trough Solar Collector

In this transient analysis of parabolic trough solar collectors different assumptions are considered: The mathematical model is based on the following assumptions:

- The heat transfer by conduction in the receiver tube is neglected.
- The absorber and the glass cover are assumed to be grey bodies.
- The form factor between the absorber and the glass cover is considered equal to 1.
- The fluid is incompressible.
- The solar flux on the absorber tube is uniform.
- Conduction losses at the ends of the receiver tube are neglected
- The flow is unidirectional.
- The glass is considered opaque to infrared radiation
- The parabolic shape is symmetrical

The following assumptions are applied in the present modeling (Tzivanidis, 2018):

- There are no contact thermal losses.
- The receiver is covered by an evacuated tube and the heat convection losses between absorber and cover are neglected.
- There is a uniform heat flux over the absorber.
- The receiver temperature does not have great variation along the tube because the collector has a reasonable length (~5 m).
- The solar collector radiates thermally to the ambient.
- There is no great difference between cover and ambient temperature levels.
- This model needs the knowledge of the fluid thermal properties, as well as of the heat transfer coefficient.
- All the thermal properties, as well as the receiver emittance, can be estimated for the temperature level of the inlet temperature.

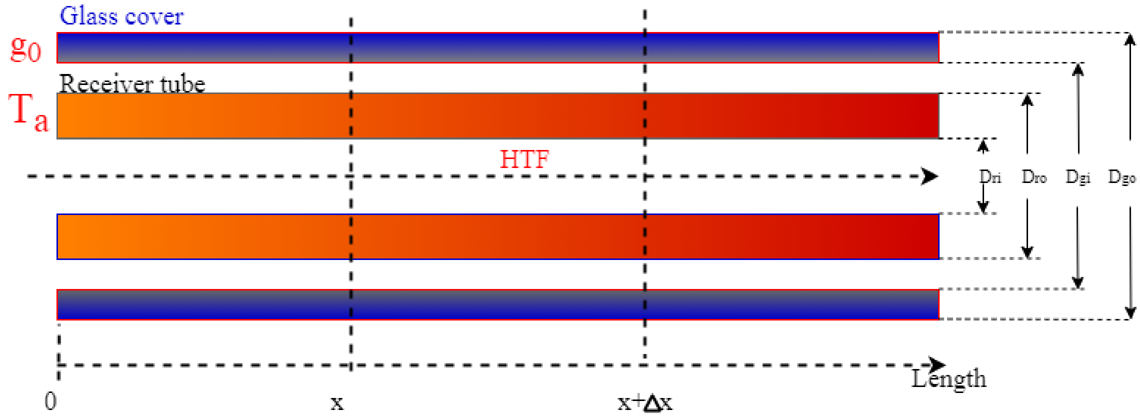

Figure 5. 5. Schematic diagram of heat transfer analysis in HCE

5.4.1 Energy Balance for the Fluid

The energy balance for the heat transfer fluid circulating in the absorber tube is expressed by the following relationship (Ghodbane, 2016).

$$\rho_F C_{P,F} A_{A,int} \frac{\partial T_F(X,t)}{\partial t} = q_u - \rho_F . C_{P,F} . Q_v . \frac{\partial T_F(X,t)}{\partial x} \tag{5.48}$$

Where

q_u – is the heat flow transmitted to the fluid [W]

ρ_F - is the fluid density $({}^{Kg}/_{m^3})$

$C_{P,F}$ - is the specific heat of fluid $({}^{J}/_{kg.K})$

Q_v - is the volume flow rate $({}^{m^3}/_{s})$

All thermophysical characteristics of the water are a function of its temperature.

Initial and boundary conditions of the above heat transfer fluid (HTF) energy balance

$$T_F(0,t) = T_F, entry(t) = T_{inlet}(t) \tag{5.49}$$

$$T_F(X,t) = T_F, initial(t) = T_{inlet}(0) \tag{5.50}$$

5.4.2 Energy Balance for the Absorbers

The energy balance for the absorber is given by the following equation (Ghodbane, 2016):

$$\rho_A C_{P,A} A_A . \frac{\partial T_F(X,t)}{\partial t} = q_{absorbed}(\mathrm{t}) - q_{exist}(X,t) - q_u(X,t) \tag{5.51}$$

$q_{absorbed/reciever}$ – is the heat quantity absorbed by the absorber tube (W)

$$q_{absorbed} = \rho_m . \gamma . A_c . K_{com} . \mathrm{DNI} \tag{5.52}$$

$$\begin{aligned}\rho_A C_{P,A} A_A . \frac{\partial T_F(X,t)}{\partial t} &= \rho_m . \gamma . A_c . K_{com} . \mathrm{DNI} - \pi D_{ro}\, h_{rad,int}(T_r - T_c) \\ &- \pi D_{ro}\, h_{cv,int}(T_r - T_c) - \pi D_{ri}\, h_{conv,f}(T_{ri} - T_F)\end{aligned} \tag{5.42}$$

Where

DNI - is direct radiation (W/ m²)

A_A - is the difference between the inner surface and the outer surface of the absorber tube (m²)

A_c – is the collector aperture area m^2

The initial conditions for the equations

$T_A(\mathrm{X,t}) = T_{A,initial}(\mathrm{t}) = T_{entry}(0)$

5.4.3 Energy Balance for the Cover (Glass Tube)

Energy balance for glass tube is (Ghodbane, 2016).

$$\rho_g C_{P,g} A_g . \frac{\partial T_g(X,t)}{\partial t} = q_{int}(X,t) - q_{ext}(X,t) \tag{5.54}$$

q_{int} - is the internal heat power (by convection and radiation) between absorber and glass tubes (W); $q_{int} = q_{ro-ci,cv} + q_{ro-ci,rad}$

Where

$$q_{ro-gi,cv} = \pi D_{ro} . h_{cv,int}(T_r - T_g) \tag{5.55}$$

$$q_{ro-gi,rad} = \pi D_{ro}\, h_{rad,int}(T_r - T_g) \tag{5.56}$$

$\boldsymbol{q_{ext}}$ - is the external heat power (by convection and radiation) between the glass tube and the atmosphere (W).

$$\boldsymbol{q_{ext}} = q_{go-amb\,,cv} + q_{go-sky\,,rad} \tag{5.57}$$

Where

$$q_{go-amb\,,cv} = A_{go} \,.\, h_{out} .\, (T_c - T_{am}) \tag{5.58}$$

$$q_{go-sky\,,rad} = A_{go} .\, \sigma .\, ({T_c}^4 - {T_{sky}}^4) \tag{5.59}$$

$$\rho_g C_{P,g} A_g . \frac{\partial T_g(X,t)}{\partial t} = [\pi D_{ro} \,.\, h_{cv,int}(T_r - T_g) + \pi D_{ro}\, h_{rad,int}(T_r - T_g)] - [A_{go} \,.\, h_{out} .\, (T_c - T_{am}) + A_{go} .\, \sigma .\, ({T_g}^4 - {T_{sky}}^4)] \tag{5.60}$$

The initial condition of the equation is $T_g(\mathrm{X}, \mathrm{t}) = T_{g,initial}(\mathrm{t}) = T_{amb}(0)$

The above differential equations are discretized by using an Explicit Finite difference method. The length of HCE $0 \leq x \leq L$ is divided into Δx equal parts of the mesh size. A forward time and centered space finite difference scheme are used to obtain the following Equations

$$\frac{\partial T_F(X,t)}{\partial t} = \frac{{T_{F,n}}^{i+1} - {T_{F,n}}^{i}}{\Delta t} \tag{5.61}$$

$$\frac{\partial T_g(X,t)}{\partial t} = \frac{{T_{g,n}}^{i+1} - {T_{g,n}}^{i}}{\Delta t} \tag{5.62}$$

$$\frac{\partial T_r(X,t)}{\partial t} = \frac{{T_{A,n}}^{i+1} - {T_{A,n}}^{i}}{\Delta t} \tag{5.63}$$

$$\frac{\partial T_F(X,t)}{\partial x} = \frac{{T_{F,n+1}}^{i} - {T_{F,n-1}}^{i}}{2\Delta x} \tag{5.64}$$

By applying the above derivatives and some re arrangement the following algebraic equations obtained:

For fluid transfer

$${T_{F,n}}^{i+1} = [(\frac{1}{\Delta t} - \frac{\pi D_{r,i} \cdot h_{cv,int}}{\rho_F C_{P,F} A_{F,int}}) * {T_{F,n}}^{i} + \frac{\pi D_{r,i} \cdot h_{cv,int}}{\rho_F C_{P,F} A_{F,int}} {T_{r,n}}^{i} - \frac{\dot{m} C_{p,F}}{2 \rho_F C_{P,F} A_{F,int} \Delta x} (T_{F,n+1^i} - T_{F,n-1^i})]\, \Delta t \tag{5.65}$$

For receiver/Absorber

$$T_{A,n}{}^{i+1} = \Big[\frac{I_d \tau_g \alpha_{abs} r_m W K(\theta)}{\rho_A C_{P,A} A_A} + \Big(\frac{1}{\Delta t} - \Big(\frac{\pi D_{A,e}\ .\ h_{cv,int}}{\rho_A C_{P,A} A_A} + \frac{\pi D_{A,e}\ .\ h_{r,int}}{\rho_A C_{P,A} A_A} + \frac{\pi D_{A,i}\ .\ h_{cv,F}}{\rho_A C_{P,A} A_A}\Big) * T_{A,n}{}^{i} + \Big(\frac{\pi D_{A,e}\ .\ h_{cv,int}}{\rho_A C_{P,A} A_A} + \frac{\pi D_{A,e}\ .\ h_{r,int}}{\rho_A C_{P,A} A_A}\Big) T_{g,n}{}^{i} + \Big(\frac{\pi D_{A,i}\ .\ h_{cv,F}}{\rho_A C_{P,A} A_A}\Big) T_{F,n}{}^{i}\Big] \Delta t \qquad (5.66)$$

For cover/ glass

$$T_{g,n}{}^{i+1} = \Big[\Big(\frac{1}{\Delta t} - \frac{h_{cv,int}}{\rho_g C_{P,g} A_g} - \frac{\pi D_{A,e}\ .h_{r,int}}{\rho_g C_{P,g} A_g} - \frac{\pi D_{g,e}\ .h_{cv,int}}{\rho_g C_{P,g} A_g} - \frac{\pi D_{g,e}\ .h_{r,ext}}{\rho_g C_{P,g} A_g}\Big) T_{g,n}{}^{i} + \Big(\frac{h_{cv,int}}{\rho_g C_{P,g} A_g} + \frac{\pi D_{A,e}\ .h_{r,int}}{\rho_g C_{P,g} A_g}\Big) T_{A,n}{}^{i} + \Big(\frac{\pi D_{g,e}\ .h_{cv,int}}{\rho_g C_{P,g} A_g}\Big) T_{amb}{}^{i} + \Big(\frac{\pi D_{g,e}\ .h_{r,ext}}{\rho_g C_{P,g} A_g}\Big) T_{sky}{}^{i}\Big] \qquad (5.67)$$

Initials condition

At t =t_0; for $0 \le x \le L$

The glass envelope is at ambient air temperature

T_g(X, t_0) = T_{amb}(X, t_0)

The absorber is assumed to be 5℃ above the ambient air. T_g(X, t_0) = T_{amb}(X, t_0) + 5℃

The fluid is assumed as an initial temperature of 125℃ at the inlet of parabolic trough solar collectors.

5.5 Heat Exchanger

Assela Malt factory uses heat exchanger for heat transfer from steam which comes from boiler to an air which kilns a Malt. Assela Malt factory requires 10000 kg/hr of steam at 160℃ temperature energy for drying the Malt. The heat transfer fluid (HTF) which comes from parabolic trough collector that passes through phase change materials is set to be 160℃. It is convenient in solar process system calculations to use the effectiveness-NTU (number of transfer units) method of calculation of heat exchanger performance. A brief discussion of the method is provided here, based on the example of a countercurrent exchanger.

The working equation is the same for other heat exchanger configurations; the expressions for effectiveness vary from one configuration to another (Duffie and Beckman, 2013)

A schematic of an adiabatic countercurrent exchanger with inlet and outlet temperatures and capacitance rates of the hot and cold fluids. The overall heat transfer coefficient—area product is UA. The maximum possible temperature drop of the hot fluid is from $T_{h,in}$ to $T_{c,in}$; the heat transfer for this situation would be

$$Q_{max} = (\dot{m}C_p)_h(T_{h,in} - T_{h,out}) \quad (5.68)$$

Where $\dot{m} = mass\ flow\ rate\ of\ hot\ water\ enter\ to\ heat\ exchanger$

$C_p - specific\ heat\ of\ water\ at\ 158'C$

$$Q_{max,h} = 2.777\frac{kg}{s} * 4330\frac{J}{kg.K} * (158 - 120)^{O}C = Q_{h,water} = 465.092KW$$

The maximum possible temperature rise of the cold fluid would be from T_{ci} to T_{hi}. The maximum heat transfer that could occur in the exchanger is thus fixed by the lower of the two capacitance rates, $\dot{m}C_p)_{min}$ and The corresponding maximum heat exchange would be

$$Q_{max} = (\dot{m}C_p)_{min}\,(T_{hi} - T_{ci})$$

The actual heat exchange Q is given by

$$Q = (\dot{m}C_p)_h(T_{hi} - T_{ci}) = (\dot{m}C_p)_c(T_{hi} - T_{ci})$$

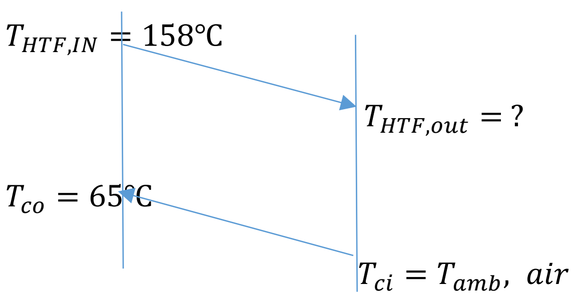

Since the ambient temperature of air varies with time the outlet temperature of heat transfer fluid (HTF) also varies with time.

$$Q_u = (\dot{m}C_p)_{HTF}\big(T_{HTF,in} - T_{HTF,out}\big) = (\dot{m}C_p)_{air}\big(T_{amb,in} - T_{air,out}\big) \quad (5.69)$$

5.6 Sizing of Parabolic Trough Solar Collector

The primary step in the design of a parabolic trough solar field is to explain a set of factors that determine solar field performance. These factors are collector positioning, day of the design point, direct solar irradiance (DNI) and ambient air temperature for the nominated date and time, geographical location of the plant site (latitude and longitude), overall thermal output power to be provided by the solar field, inlet/outlet temperatures of the solar field, heat transfer fluid (HTF) for the solar collectors and working fluid (water) flow rate.

In a typical PTSC field, several collectors connected in series make a row, and a number of rows are connected in parallel to achieve the required nominal thermal power output at the design point.

The number of collectors connected in series in every row depends on the temperature increase to be achieved between the row inlet and outlet. The number collectors of in a single row that is connected in parallel are determined based on thermal power demanded Malt kilning.

$$\text{Number of PTC collectors} = \frac{\text{Thermal power demand}}{\text{Thermal power in single PTC collector}} \qquad (5.70)$$

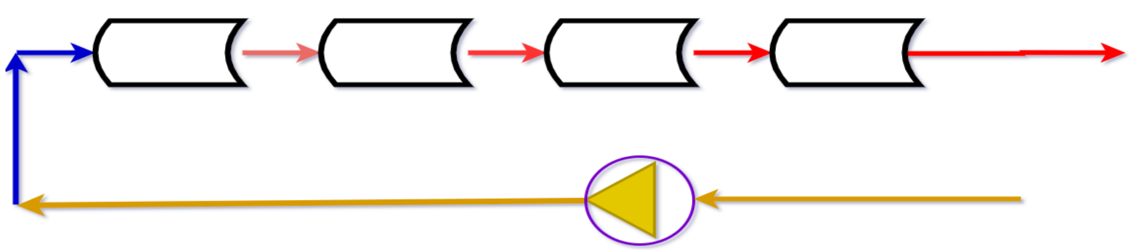

Figure 5. 6. Series parabolic trough solar collectors for Assela Malt factory

5.7 Thermal Energy Storage Analysis

One of the principal barriers stands on the intermittent nature of some renewable source, solar energy which supposes a mismatch between the energy production and demand periods. Thermal energy storage (TES) is identified as a technology that can help in the management and control of these systems by eliminating this mismatch or by making peak load shifting strategies (Gracia, 2016). Latent thermal energy storage systems are considered to be more energy-dense, efficient, and compact and have been extensively studied.

The major characteristics of a thermal energy storage system are (Duffie and Beckman, 2013)

- ✓ It is capacity per unit volume;
- ✓ the temperature range over which it operates, that is, the temperature at which heat is added to and removed from the system;
- ✓ the means of addition or removal of heat and the temperature differences associated therewith;
- ✓ temperature stratification in the storage unit;
- ✓ the power requirements for addition or removal of heat;
- ✓ the containers, tanks, or other structural elements associated with the storage system;
- ✓ the means of controlling thermal losses from the storage system; and
- ✓ Its cost.

5.7.1 Thermal Energy Storage Modes

Charging Modes: is starts with a circulation of the hot HTF heated in the collector system at a temperature higher than the PCM melting temperature. During this period, hot HTF enters the tube side at the top, transfers heat to the solid PCM, and then HTF exits at the bottom of the tubes. This mode occurs during daytime and terminates with a complete melting of the PCM, charging of the store does not terminate with a complete melting of the PCM. If the inlet fluid temperature is above the melt temperature, the charging of sensible heat continues.

Discharging Modes: This is started by the circulation of the cold HTF having inlet temperature lower than the PCM melting temperature. The cold HTF enters the system at the bottom is heated by the storage PCM, and then exits at the top. This mode terminates with complete solidification of the PCM.

Standby mode: This mode occurs when there is no further storage of energy occurring because the thermal storage tank is completely charged or the energy is directly fed to the utility without using storage. There is no flow of HTF in the tube side and heat transfer within the system is dominated by axial conduction which acts to redistribute the axial temperature gradient formed in the system during charging. This is the transition period between the charge and discharge modes**.**

5.7.2 Thermal Performance Analysis of Thermal Storage System

The first parameter considered in the selection of PCM material is its melting point. Based on melting point, the PCMs can be divided into three contributions: low-temperature heat storage (less than 120°C), medium-temperature heat storage (120–300°C), and high-temperature heat storage (more than 300°C) (Mao, 2018). The melting point temperature of the PCM should be much the operating temperature of a designed thermal system. The PCM melting point was selected with an interval of about 5 to 10 °C above the desired operating temperature of the application (Reta, 2020). Assela Malt factory used operating temperature for kilning of Malt is around 160℃. So it’s preferable to use phase change materials whose melting temperature is above 160℃.

Huang (2018) has developed and studied the PCMs with phase change points at medium temperatures between 120 and 300 °C mainly comprise of three classes: sugar alcohols, fatty acids, and inorganic salts. Here, they selected D-mannitol, sebacic acid (SA), and LiNO3-KCl eutectic to represent these three classes, respectively. Considering many medium-temperature PCM composites with desirable thermal performance.

Huang et al (2018) selected the system with 50% LiNO_3/50% KCl as the PCM and expanded graphite as the heat transfer promoter to prepare the composite of LiNO_3/KCl-EG. The experimental results revealed that the melting temperature of this composite was 165.60°C, and the latent heat ranging from 142.41 J/g to 178.10 J/g was dependent on the mass fraction of EG.

Binary and ternary mixtures of inorganic salts have been widely studied for thermal storage applications. Nitrate, chloride, and sulfate salts of alkali and alkaline metals, such as magnesium, potassium, lithium, and calcium, are the main compounds used to produce medium temperature eutectic mixtures, also known as ionic liquids (Jose, 2016).

D-mannitol is one of the greatest hopeful PCM candidates for medium-temperature applications since it also has low toxicity, low price, and, apparently, good thermal stability (Rojas, 2017).

Table 5. 2. Thermophysical properties of selected organic compounds (Cunha, 2016)

Organic Compounds	Formula	T_m (°C)	ΔH_m (kJ/kg)	k_s $(\frac{W}{m.K})$	k_l $(\frac{W}{m.K})$	Cp_s $(\frac{J}{kg.K})$	Cp_l $(\frac{J}{kg.K})$	ρ_s	$E_{density}$
D - mannitol	$C_6H_{14}O_6$	165	300	0.19	0.11	1310	2360	1490	139

5.7.3 Sizing of Latent Heat TES System

A PCM storage tank is sized according to the required storage capacity under a rated operating condition. The cylindrical LHTES unit proposed for this study consists of concentric tubes whereby the HTF and PCM are segregated. The HTF flows through the inner tubes and exchanges heat with the PCM in the surrounding region (Tehrani et al, 2016).

The graphic representation of the latent heat storage unit is shown in the figure below. As it is shown the capacity consists of internal tubes and an external tube (shell side). The heat transfer liquid (HTF) and the PCM are separated.

The HTF flows through the internal tubes and transfers heat with the PCM which is found within the external tube. For the period of the charging process (melting), the steam which comes from the parabolic trough solar collector exchanges heat with the solid PCM and the PCM the releasing process (solidification), the cold HTF circulates through the internal tube, and the PCM transfers heat with the cold HTF and begin solidifying.

Figure 5. 7. Schematic configuration of shell and tube latent heat thermal energy storage system (LHTES) unit with a complete system, and concentric cylinders (Tehrani et al., 2016).

The storage capacity of latent heat storage (LHS) system with phase change materials (PCM) is given by:

$$Q = m[a_m H + C_{sp}(T_m - T_i) + C_{lp}(T_f - T_m)] \tag{5.71}$$

Where

Q − Quantity of heat stored

m − mass of heat storage medium

a_m − fraction melted

H − Phase change enthalpy or melting enthalpy

C_{sp} − average specific heat between T_i and T_m

C_{lp} − average specific heat between T_m and T_f

T_i − initial temperature

T_m − melting temperature

T_f − final temperature

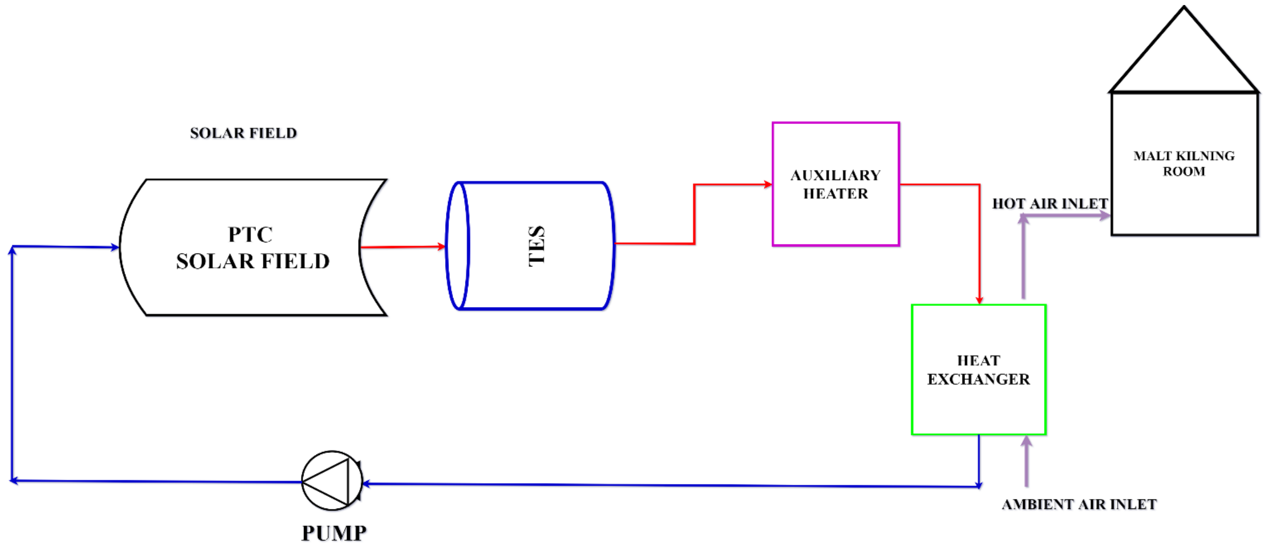

Figure 5. 8. Schematic diagram of PTSC integrated with PCM up to Malt kilning.

Sizing of thermal energy storage

$$V_{total,PCM} = \frac{Q_{HTF,TOTAL}(J)}{\rho_{pcm,s} * Cp_s(T_m - T_{ci}) + \rho_{pcm,l} * H_{pcm} + \rho_{pcm,l} * Cp_l(T_{co} - T_m) \quad (\frac{J}{m^3})} \qquad (5.72)$$

Where

Q_ (HTF, TOTAL) (J) – is the required storage capacity of the system

$\rho_{pcm,s}$, $\rho_{pcm,l}$ – density of solid and liquid PCM respectively

C_{pl}, C_{ps} – are the liquid and solid specific heat of the PCM

T_m , H_m are the phase change temperature and specific enthalpy of the PCM, respectively

From equation (5.72) the total volume of latent heat thermal storage integrating with phase change materials is $\boldsymbol{V_{T=}\ 6.7278\ m^3}$

By using the relation of $\boldsymbol{L/D\ =\ 1.75}$

The **diamete**r and **length** of the storage tank are **1.7** m and **3** m respectively and porosity is 0.45.

The range of geometric parameters selected with values of L = **2.7 m** and 0.01 $< r_{t,i} <$ 0.1.

For this study internal radius of the tube is assumed as the internal radius of the tube is $r_i = 0.03m$.

So the volume of the heat transfer fluid in a single tube is $V_{HTF} = \frac{\pi * {D_{t,i}}^2}{4} * L = \mathbf{0.00763\ m^3}$ and

The volume of phase change materials used in the latent heat storage system is $\mathbf{5.05\ m^3}$

$$\boldsymbol{V_{HTF} = V_T - V_{PCM}}$$

From the total volume of phase change material and a single volume of phase change materials we calculate the total volume of tube:

$$N_t = \frac{V_{HTF,total}}{V_{HTF,single}}$$

To fulfill the thermal energy demand **219.89** number of the tube is required, which is approximately **220** number of tube required.

- ✓ Mass of phase change materials (m_{PCM})

The total amount of phase change material required is evaluated from the density and volume of phase change materials.

$m_{PCM} = V_{PCM} * \rho_{PCM} = (1 - \varepsilon) * V_{PCM} * \rho_{PCM,S}$

Where m_{PCM} – mass of PCM, V_{PCM} – Volume of PCM, ρ_{PCM} – Density of PCM

By substituting in the above equations **4139 kg** of phase change material mass is required.

To simplify the physical and mathematical models, the following assumptions have been made:

- ➢ The PCM is isotropic (having identical thermos physical property values in all directions).
- ➢ The thermal resistance of the inner tube is negligible.
- ➢ The thermos physical properties of the HTF and the PCM are independent of temperature; however, the thermal conductivity and the specific heat capacity of the PCM in the solid and liquid phase are different.
- ➢ The axial conduction in the HTF is negligible.
- ➢ Any small void spaces between LHTES pipes are neglected.
- ➢ The latent heat storage unit is well insulated, so there are no heat losses to the environment.

5.7.4 Mathematical Modeling and Performance Analysis of Shell and Tube LHTES integrating with PCM

This investigation leads to an analysis of the formulation of a mathematical model that defines moving solid-liquid interfaces. The transient heat transfer between the operating fluid (HTF) and the PCM is numerically investigated using a finite difference scheme. The numerical investigation of the shell and tube LHTES system employing numerical model and simulation with a MATLAB software package. The energy conservation is expressed in terms of total volumetric enthalpy and temperature for constant thermophysical properties by equation.

$$\frac{\partial \rho H}{\partial t} + \nabla.(\rho \mathrm{v} H) = \nabla.(k \nabla T) \tag{5.73}$$

Where

H – Volumetric enthalpy which is the addition of sensible and latent heat

$$H = h + \gamma h_{PCM} \tag{5.74}$$

$$\mathrm{x}h = h_{ref} + \int_{T_{in}}^{T} C_P dt \tag{5.75}$$

$\gamma -$ indicates to fluid(liquid) fraction and shows the fraction of a cell volume in the fluid.

$$\gamma = \begin{cases} 0 & \mathrm{T} < \mathrm{T_{solidus}} \\ \dfrac{\mathrm{T} - \mathrm{T_s}}{\mathrm{T_l} - \mathrm{T_s}} \quad (0 < \mathrm{f} < 1) & \mathrm{T_s} \leq \mathrm{T} \leq \mathrm{T_l} \\ 1 & \mathrm{T} > \mathrm{T_{liquidus}} \end{cases} \tag{5.76}$$

The governing equations of the problem are the energy conservation equations written for the HTF (Heat Transfer Fluid), the wall, and the PCM in a cylindrical orientation system. The main heat exchange mechanism within the HTF is convection. So, it is possible to model the heat transfer within the HTF through the definition of a convective heat transfer coefficient *h*. The computational domain is discretized using 12 nodes in the axial direction (Fortunato, 2012).

Energy equation is

$$\frac{\partial \rho H}{\partial t} + \nabla.(\rho \mathrm{v} H) = \nabla.(k \nabla T) - \frac{\partial \rho h_{PCM}}{\partial t} - \nabla.(\rho v f h_{PCM}) \tag{5.77}$$

$$\frac{\partial \mathrm{H}}{\partial \mathrm{t}} = \frac{\mathrm{H}(\mathrm{T}^{\mathrm{i}+1} - \mathrm{T}^{\mathrm{i}})}{\Delta \mathrm{t}} \tag{5.78}$$

The convective heat transfer coefficient is calculated as follow

- ✓ Area of tube (A_t)

$$A_t = \frac{\pi}{4} * {D_{i,t}}^2 = \frac{\pi}{4} * 0.06^2 = \mathbf{0.002827\ m^2}$$

- ✓ Heat transfer fluid average velocity (u_m)

$$u_m = \frac{\dot{m}_f}{\rho * A_t} = \frac{0.01}{910 * 0.0012566} = \mathbf{0.003887}\ {}^{\boldsymbol{m}}\!/_{\boldsymbol{s}}$$

- ✓ Reynolds number (R_e)

$$R_e = \frac{\rho * u_m * D_{i,t}}{\mu} = \frac{910 * \mathbf{0}.003887\ {}^{m}\!/_{s} * 0.06m}{1.729 * 10^{-4}} = \mathbf{1227.525}$$

Since $R_e < 2300$ then the flow is laminar flow inside the tube.

$\mathrm{N_u} = 3.66$

- ✓ prandl number ($\mathrm{P_r}$)

$$\mathrm{P_r} = \frac{C_p * \mu}{K(T_{average})} = \frac{4.342 * 10^3 * 1.729 * 10^{-4}}{0.68} = \mathbf{1.1}$$

- ✓ Nusselt number($\mathrm{N_u}$)

$$\mathrm{N_u} = 1.86 * (R_e * \mathrm{P_r} * \tfrac{D_{i,t}}{L})^{1/3} = 1.86 * \left(1227.525 * 1.1 * \tfrac{0.06}{2.7}\right)^{1/3} = \mathbf{5.78}$$

- ✓ Convective heat transfer coefficient(h_f)

$$h_f = \frac{\mathrm{N_u} * K(T_{average})}{D_{i,t}} = \frac{5.78 * 0.68}{0.06} = \mathbf{65.5}\,\frac{\boldsymbol{W}}{\boldsymbol{m^2 K}}$$

a. Heat transfer fluid (HTF)

$$\rho_f * C_{p,f} * \frac{\partial T_f}{\partial t} = \frac{-\dot{m}_f * C_{p,f}}{A_{t,f}} * \frac{\partial T_f}{\partial y} + \frac{h * \pi * D_{i,t}}{A_{t,f}} * (T_w - T_f) \tag{5.79}$$

Where

$\rho_f, C_{p,f}, \dot{m}_f -$ density, specific heat, and mass flow rate of HTF respectively.

$h, D_{i,t} -$ Convective heat transfer coefficient and an inner tube diameter of HTF respectively.

$A_{t,f} -$ inner tube cross − section area of fluid (heat transfer fluid).

$T_w, T_f -$ temperature of the wall and HTF respectively

$$\frac{\partial T_f}{\partial t} = \frac{{T_{f,i}}^{t+\Delta t} - {T_{f,i}}^{t}}{\Delta t} \tag{5.80}$$

$$\frac{\partial T_f}{\partial y} = \frac{{T_{f,i}}^{t+\Delta t} - {T_{f,i-1}}^{t+\Delta t}}{\Delta y} \quad (5.81)$$

$$\frac{{T_{f,i}}^{t+\Delta t} - {T_{f,i}}^{t}}{\Delta t} = \frac{1}{\rho_f * C_{p,f}} (\frac{-\dot{m_f} * C_{p,f}}{A_{t,f}} * (\frac{{T_{f,i}}^{t+\Delta t} - {T_{f,i-1}}^{t+\Delta t}}{\Delta y}) + \frac{h * \pi * D_{i,t}}{A_{t,f}} * ({T_{w,i}}^{t} - {T_{f,i}}^{t})) \quad (5.82)$$

$${T_{f,i}}^{t+\Delta t} = \frac{1}{1 - AB * \frac{\Delta t}{\Delta y}} * [(1 - \Delta t * CD) * {T_{f,i}}^{t} + AB * \frac{\Delta t}{\Delta y} * {T_{f,i-1}}^{t+\Delta t} + \Delta t * CD * {T_{w,i}}^{t}] \quad (5.83)$$

Where

$$AB = \frac{\dot{m_f}}{\rho_f * A_{t,f}} \quad (5.84)$$

$$CD = \frac{\mathrm{h} * \pi * \mathrm{D_{i,t}}}{\rho_\mathrm{f} * \mathrm{C_{p,f}} * \mathrm{A_{t,f}}} \quad (5.85)$$

${T_{f,i}}^{t+\Delta t}$ – new temperature at node i

${T_{f,i}}^{t}, {T_{w,i}}^{t}$ – The previous time nodal temperature of HTF and wall at time t.

b. Wall

$$\rho_w * C_{p,w} * \frac{\partial T_w}{\partial t} = \frac{1}{\delta_w}\left(\frac{kA_{i,w}}{A_{t,w}} + R_w + \frac{k_{pcm}A_{i,pcm}}{A_{t,w}}\right) * \left(T_{pcm} - T_w\right) + \frac{h * \pi * D_o}{A_{t,w}}(T_f - T_w) \quad (5.86)$$

Where

$\mathrm{k_w}$, $\mathrm{k_{PCM}}$ – Thermal conductivity of the wall and phase change materials respectively

$\mathrm{R_w}$ – the tube wall resistance which is negligible

$\delta_w, A_{t,w}$ – are the thickness of the wall and cross – section area of the wall respectively

Discretization using finite difference

$$\frac{{T_{w,i}}^{t+\Delta t} - {T_{w,i}}^{t}}{\Delta t} = (\frac{k_w A_{l,w}}{A_{t,w}} + \frac{k_{pcm}A_{l,pcm}}{A_{t,w}}) * \frac{{T_{pcm,i}}^{t} - {T_{w,i}}^{t}}{\rho_w * C_{p,w} * \delta_w} + \frac{h * \pi * D_o}{A_{t,w} * \rho_w * C_{p,w}}({T_{f,i}}^{t} - {T_{w,i}}^{t}) \quad (5.87)$$

$${T_{w,i}}^{t+\Delta t} = (1 - \Delta t * EF - \Delta t * GH){T_{w,i}}^{t} + \Delta t * EF * {T_{f,i}}^{t} + \Delta t * GH * {T_{pcm,i}}^{t} \quad (5.88)$$

$$EF = \frac{h * \pi * D_o}{A_{t,w} * \rho_w * C_{p,w}} \quad (5.89)$$

$$GH = \frac{1}{\rho_w * C_{p,w} * \delta_w}(\frac{k_w A_{l,w}}{A_{t,w}} + \frac{k_{pcm} A_{l,pcm}}{A_{t,w}}) \quad (5.90)$$

$T_{w,i}^{t+\Delta t}$ − temperature of a wall at node i

$T_{w,i}^{t}, T_{pcm,i}^{t}, T_{f,i}^{t}$ − are previuous temperature of wall, pcm and HTF at time t

c. Phase Change Materials (PCM)

The general cell of the PCM

Governing equation:

$$\rho_{pcm} * \frac{\partial H_{pcm}}{\partial t} = \frac{k_{pcm}}{C_{p,pcm}}(\frac{1}{r} * \frac{\partial}{\partial r} * \left(r * \frac{\partial H_{pcm}}{\partial r}\right)) \quad (5.91)$$

The time discretization the semi-implicit of first order accurate is adopted:

$$\frac{H_{pcm,i}^{t+\Delta t} - H_{pcm,i}^{t}}{\Delta t} = \frac{1}{2} * (\frac{k_{pcm}}{C_{p,pcm}}\left(\frac{1}{r} * \frac{\partial}{\partial r} * \left(r * \frac{\partial H_{pcm}}{\partial r}\right)\right)^{t+\Delta t} + \frac{k_{pcm}}{C_{p,pcm} * \rho_{pcm}}[\frac{1}{r} * \frac{\partial}{\partial r} * \left(r * \frac{\partial H_{pcm}}{\partial r}\right)]^{t}) \quad (5.92)$$

$$\rho_{pcm} * \frac{\partial H_{pcm}}{\partial t} = \frac{1}{\delta_w}\left(\frac{k_w A_{l,w}}{A_{t,w}} + \frac{k_{pcm} A_{l,pcm}}{A_{t,w}}\right) * \left(T_{pcm} - T_w\right) + \frac{1}{\delta_w} * \frac{k_{pcm}}{A_{pcm}}\left(\frac{H_{pcm}^{i+1} - H_{pcm}^{i}}{A_{t,w}}\right) \quad (5.93)$$

$$\rho_{pcm} * C_p(T) * \frac{\partial T}{\partial t} = \frac{1}{\delta_w}\left(\frac{k_w A_{l,w}}{A_{t,w}} + \frac{k_{pcm} A_{l,pcm}}{A_{t,w}}\right) * \left(T_{pcm} - T_w\right) + \frac{1}{\delta_w} * \frac{k_{pcm}}{A_{pcm}} * C_p(T)\left(\frac{T_{pcm}^{i+1} - T_{pcm}^{i}}{A_{t,w}}\right) \quad (5.94)$$

$$\rho_{pcm} * C_p \frac{T_{pcm,i}^{t+\Delta t} - T_{pcm,i}^{t}}{\Delta t} = \frac{1}{\delta_w}\left(\frac{k_w A_{l,w}}{A_{t,w}} + \frac{k_{pcm} A_{l,pcm}}{A_{t,w}}\right) * \left(T_{pcm}^{t} - T_{pcm}^{t}\right) + \frac{1}{\delta_w} * \frac{k_{pcm}}{A_{pcm} * A_{t,w}} * C_p * (T_{pcm,i}^{t+\Delta t} - T_{pcm,i}^{t}) \quad (5.95)$$

$$T_{pcm,i}^{t+\Delta t} = \left(\frac{1}{1 - \Delta t * KL}\right) * (1 + \Delta t * IJ - \Delta t * KL) * T_{pcm,i}^{t} - \Delta t * IJ * T_{w,i}^{t} \quad (5.96)$$

$$IJ = \frac{1}{\delta_w * \rho_{pcm} * C_p}\left(\frac{k_w A_{l,w}}{A_{t,w}} + \frac{k_{pcm} A_{l,pcm}}{A_{t,w}}\right) \tag{5.97}$$

$$KL = \frac{k_{pcm}}{\rho_{pcm} * A_{pcm} * A_{t,w} * \delta_w} \tag{5.98}$$

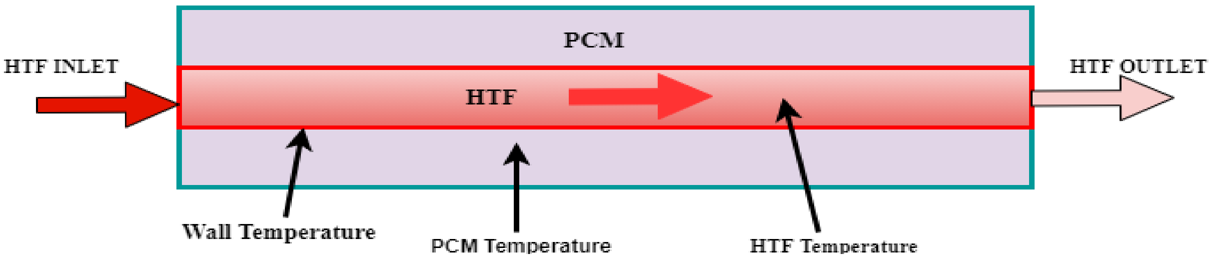

Figure 5. 9. Schematic diagram of transient heat transfer flow through the shell and tube latent heat thermal storage system

Initials and boundary conditions

To solve the discretized governing form of the HTF (heat transfer fluid) and PCM (phase change materials) an initial and boundary conditions are displayed. The temperature inlet of the HTF to the thermal energy storage tank is the outlet temperature of the parabolic trough solar collector. Initial conditions of fluid inner the cylindrical tube

$$T_{HTF}(x, t = 0) = T_{HTF,initial} = T_{HTF(outlet\ T\ from\ the\ collector)} \tag{5.99}$$

Wall temperature of the tube is an average of heat transfer and phase change temperature:

$$T_w = \frac{T_{HTF} + T_{pcm}}{2} \text{ at initial conditions } t = 0 \tag{5.100}$$

The initial temperature of phase change materials is equal to ambient temperature at t=0

$$T_{pcm}(x, t = 0) = T_{pcm,initial} = T_{ambient} \tag{5.101}$$

Boundary condition

$$T_{HTF}(x = t, 0) = T_{HTF,initial} = T_{HTF(outlet\ T\ from\ the\ collector)}$$

$$\frac{\partial T_f(x=l,t)}{\partial x} = 0\,, \frac{\partial T_w}{\partial x} = 0\,, \frac{\partial T_{pcm}}{\partial x} = 0 \qquad (5.102)$$

5.7.5 Pressure Drop in the Parabolic Trough Solar Collectors

Pressure drop in the parabolic trough solar collector depends on the diameter of the absorber tube, mass flow rate, and flow pattern based on the schematic diagram.

At the average temperature of 190°C the following properties are from table

Density $(\rho) = 877.895\ \frac{kg}{m^3}$

Dynamic viscosity $(\mu) = 1.3475 * 10^{-4}\,\frac{kg}{m.s}$

Mass flow rate inside the tube $(\dot{m} = 0.05\,\frac{kg}{s})$

Then volume flow rate is calculated as

$$Q = \frac{\dot{m}}{\rho} \qquad (5.103)$$

$$= \frac{0.05\,\frac{kg}{s}}{877.895\ \frac{kg}{m^3}} = 5.695 * 10^{-5}\,\frac{m^3}{s}$$

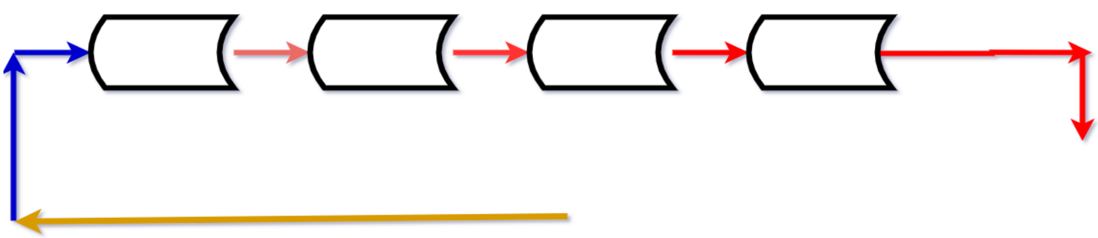

Figure 5. 10. Schematic diagram of pressure drop in series parabolic trough solar collector

- **Pressure drop inside the absorber tube**

Assuming the volume flow rate inside the tube is uniform where the diameter of absorber tube is 0.066m:

$$Q = 5.695 * 10^{-5}\,\frac{m^3}{s}$$

The average velocity inside the absorber tube is

$$V_{av} = \frac{Q}{A_{ab,tube}} = \frac{5.695 * 10^{-5}\,\frac{m^3}{s}}{\pi/_4 * 0.066^2 m^2} = \mathbf{0.016646}\,\frac{\boldsymbol{m}}{\boldsymbol{s}}$$

Reynolds number $R_e = \frac{\rho * V_{av} * D}{\mu} = \mathbf{7157.7}$

For the tube material of galvanized steel, the equivalent roughness is, $\varepsilon = 0.15mm$ and $k = \frac{\varepsilon}{D} = 0.0022727$ since relative roughness is less than 0.01. Then from the moody formula friction factor for turbulent flow is calculated as:

$$f = 0.0055 * (1 + \left(2 * 10^4 * \frac{k}{D} + \frac{10^6}{Re})^{\frac{1}{3}}\right) \tag{5.104}$$

$$f = 0.03688$$

Pressure drop inside the absorber tube is (Shuja et al., 2019)

$$\Delta P_{ab,tube} = f * \frac{L}{D} * \frac{\rho * {V_{av}}^2}{2} \tag{5.105}$$

$\Delta \boldsymbol{P}_{\boldsymbol{ab,tube}} = \mathbf{1.9033}\boldsymbol{pa}$

- **Pressure drop inside the header**

The average volume flow rate is

$$Q_{av} = \frac{\dot{Q}}{2} = \frac{5.695 * 10^{-5}\,\frac{m^3}{s}}{2} = 2.8475 * 10^{-5}\,\frac{m^3}{s}$$

$$V_{av} = \frac{Q_{av}}{A_{header}} = \mathbf{0.008323}\,{}^{\boldsymbol{m}}/_{\boldsymbol{s}}$$

$R_e = \frac{\rho * V_{av} * D}{\mu} = \mathbf{29.787}$ **,** f = $\frac{64}{R_e}$

For laminar flow $\Delta P_{header} = f * \frac{L}{D} * \frac{\rho * {V_{av}}^2}{2} = \mathbf{27.71658}\,\boldsymbol{Pa}$

For two headers $\Delta P_{header} = \mathbf{2 * 27.71658}\boldsymbol{pa} = \mathbf{55.433}$ **Pa**

- **Pressure drop in the fitting**

There are 2 bends in the single parabolic trough collectors. For 90° bends laminar flow $k_f = 0.9$

$$\Delta P_f = k_f * \frac{\rho * {V_{av}}^2}{2} \tag{5.106}$$

$\Delta P_f = \mathbf{0.35}\boldsymbol{pa}$

For four series-connected the pressure drop in the fitting is

$\Delta P_f = k_f * \frac{\rho * {V_{av}}^2}{2} = \mathbf{4} * \mathbf{0.35}\boldsymbol{pa} = \mathbf{1.4}\boldsymbol{pa}$

- **Pressure drop inside the connection tube**

The total connection tube length for a single collector is:

$$\Delta P_{connection} = f * \frac{L}{D} * \frac{\rho * {V_{av}}^2}{2} \tag{5.107}$$

$\Delta \boldsymbol{P_{connection}} = \mathbf{24.262}\ \boldsymbol{pa}$

Total pressure drop is the sum of each pressure drop:

$$\Delta \boldsymbol{P_T} = \Delta P_{ab,tube} + \Delta P_{connection} + \Delta P_f + \Delta P_{header} \tag{5.108}$$

$\Delta \boldsymbol{P_T} = \mathbf{82.9983}\boldsymbol{pa}$

5.7.5.1 Pressure Drop of Parabolic Trough Solar Collector's Assembly for Assela Malt Factory

To fulfill the thermal energy demand of the Assela Malt factory for steam supply instead of boiler 84 parabolic solar collectors are required. The flow pattern of the collector is in a series and parallel. Four (4) collectors are connected in series to get the required operating temperatures with the same mass flow rate in the tube. 21 collectors are connected with parallel to get the energy demand used in the Assela Malt factory.

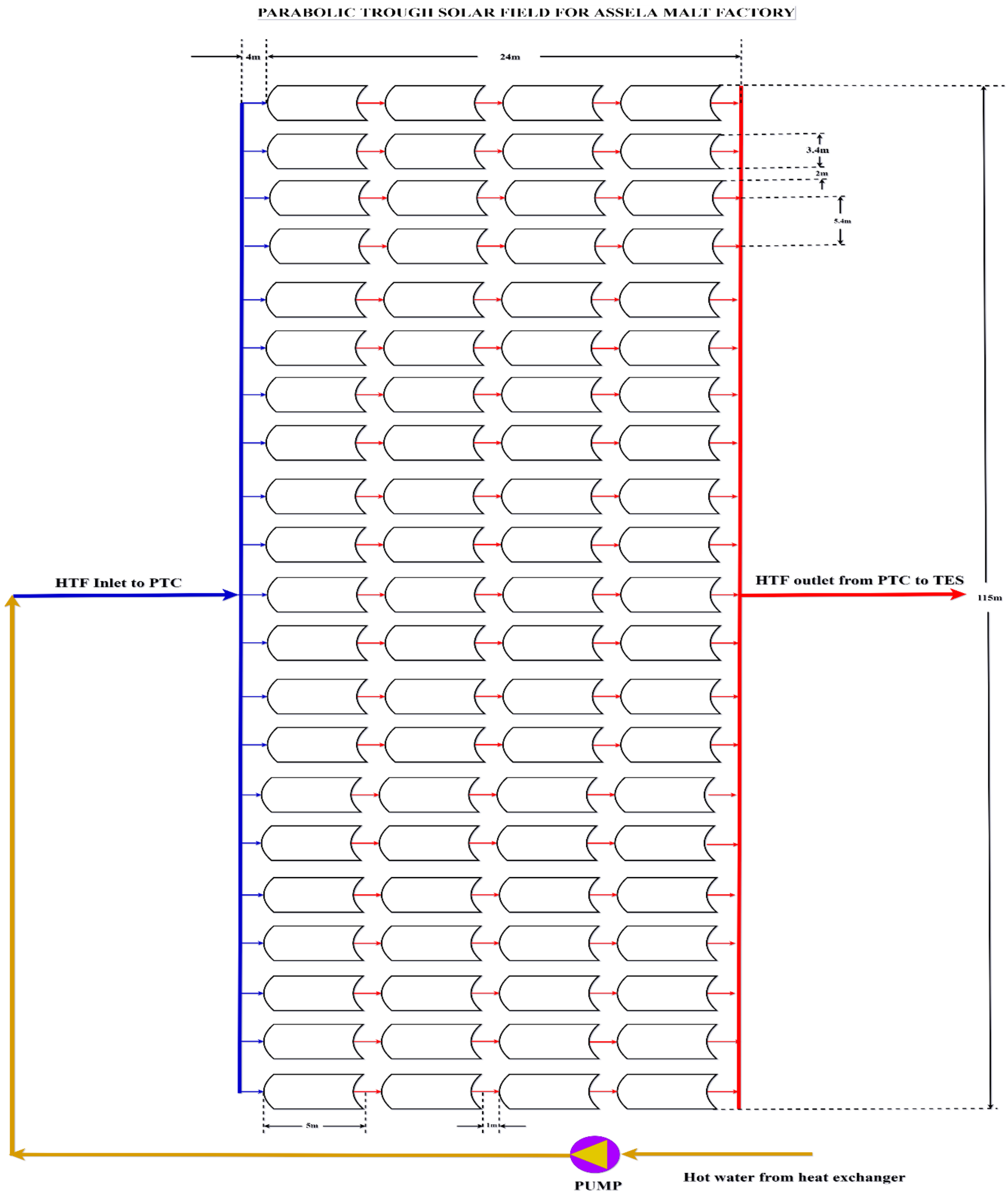

Figure 5. 11. Solar field of parabolic trough solar collectors

Generally, the Assela Malt factory uses parabolic trough solar collectors with 21 collectors in parallel and each parallel collector is connected with 4 series collectors.

Pressure drop in the line up to the collector assembly

Assuming the length between the pump and the collector is 50m and the closed-loop is 170m

Total volume flow rate is

$$Q = 21 * \frac{\dot{m}}{\rho} = 21 * \frac{0.05\,\frac{kg}{s}}{877.895\,\frac{kg}{m^3}} = \mathbf{1.196 * 10^{-3}\,\frac{m^3}{s}}$$

Average velocity is calculated as where the diameter of the tube is 66mm

$$V_{av} = \frac{Q}{A_{ab,tube}} = 0.35\,\frac{m}{s}$$

Reynolds number is $R_e = \frac{\rho * V_{av} * D}{\mu} = 150.323 * 10^3$ since Re>2300 the flow is turbulent.

The tube material is stainless steel $k = 0.15$mm, $\frac{k}{D} = 0.0022727$

The frictional factor is evaluated from the moody chart if the flow s turbulent:

$$f = 0.0055 * (1 + \left(2 * 10^4 * \frac{k}{D} + \frac{10^6}{Re})^{\frac{1}{3}}\right) = 0.026$$

$$\Delta P_m = f * \frac{L}{D} * \frac{\rho * {V_{av}}^2}{2} = \mathbf{12528.3\ Pa}$$

- **Pressure drop in the fitting**

There are 2 bends in the single parabolic trough collectors

$$\Delta P_f = 21 * k_f * \frac{\rho * {V_{av}}^2}{2} = \mathbf{2460\ Pa}$$

Where k_f- Pressure loss factor = 0.9

Total pressure drop in single parabolic trough solar collector is $\Delta P_T = 82.99 pa$

Pressure drop due to the inclination of the collector to the horizontal

$$\Delta \boldsymbol{P_h = \rho g h = 6338.25\ Pa}$$

Total pressure drop in PTC solar field of Assela Malt factory is

$$\Delta \boldsymbol{P_{Total} = 21409.29\ Pa}$$

Total specific work $y = \frac{\Delta P_{Total}}{\rho} = \mathbf{24.387}\, {\boldsymbol{m^2}}/{\boldsymbol{s^2}}$

Total static head = $\frac{y}{g} = \mathbf{3m}$

$$Q = \mathbf{1.196 * 10^{-3}\,\frac{m^3}{s}}$$

5.7.6 Pressure Drop in the Thermal Energy Storage (Shell and Tube)

For Assela Malt factory thermal energy storage (phase change material) is used to store thermal energy during the daytime. Phase change material is filled in the cylinder and HTF is flows through the tubes which also filled in the cylinder. Pressure drops in the thermal energy storage are calculated as follow:

Pressure drop in the thermal energy storage (PCM) depends on the diameter of HTF tubes, mass flow rate, and flow pattern based on the schematic diagram.

At the average temperature of 190°C the following properties are from table

Density $(\rho) = 877.895\ \frac{kg}{m^3}$

Dynamic viscosity $(\mu) = 1.3475 * 10^{-4}\,\frac{kg}{m.s}$

Mass flow rate inside the tube ($\dot{m} = 0.01\,\frac{kg}{s}$)

Then volume flow rate is calculated as

$$Q = \frac{\dot{m}}{\rho} = \frac{0.01\frac{kg}{s}}{877.895\,\frac{kg}{m^3}} = \mathbf{1.139 * 10^{-5}\,\frac{m^3}{s}}$$

- **Pressure drop inside the absorber tube**

Assuming the volume flow rate inside the tube is uniform where the diameter of HTF tube is 0.06m:

$$Q = 1.139 * 10^{-5}\,\frac{m^3}{s}$$

The average velocity inside the HTF is

$$V_{av} = \frac{Q}{A_{ab,tube}} = \frac{1.139 * 10^{-5}\frac{m^3}{s}}{\pi/_4 * 0.06^2 m^2} = \mathbf{0.004028}\frac{\boldsymbol{m}}{\boldsymbol{s}}$$

Reynolds number $R_e = \frac{\rho * V_{av} * D}{\mu} = \mathbf{1574.7}$

Since Reynolds number is < 2300 the flow is laminar. f = $\frac{64}{R_e} = 0.0406$

Pressure drop inside the absorber tube is (Shuja et al., 2019)

$$\Delta P_{ab,tube} = f * \frac{L}{D} * \frac{\rho * {V_{av}}^2}{2}$$

$$\boldsymbol{\Delta P_{ab,tube} = 0.0121\ Pa}$$

- **Pressure drop inside header**

The average volume flow rate is

$$Q_{av} = \frac{\dot{Q}}{2} = \frac{1.139 * 10^{-5}\frac{m^3}{s}}{2} = \mathbf{0.5695 * 10^{-5}}\ \frac{\boldsymbol{m^3}}{\boldsymbol{s}}$$

$$V_{av} = \frac{Q_{av}}{A_{header}} = \mathbf{0.002014}\ \boldsymbol{m/_s}$$

$R_e = \frac{\rho * V_{av} * D}{\mu} = \mathbf{787.347}$ **Pa ,** f = $\frac{64}{R_e} = 0.0813$

For laminar flow

$$\Delta P_{header} = f * \frac{L}{D} * \frac{\rho * {V_{av}}^2}{2} = \boldsymbol{0.00677\ Pa}$$

For two headers $\Delta P_{header} = \mathbf{2 * 0.00677}\ \boldsymbol{Pa} = \mathbf{0.01354}$ **Pa**

- **Pressure drop in the fitting**

There are 2 bends in the thermal energy storage. For 90° bends laminar flow $k_f = 0.9$

$$\Delta P_f = k_f * \frac{\rho * {V_{av}}^2}{2} = \boldsymbol{0.35\ Pa}$$

The pressure drop in the fitting is

$$\Delta P_f = k_f * \frac{\rho * {V_{av}}^2}{2} = \mathbf{4 * 0.35\ Pa = 1.4\ Pa}$$

Pressure drop in a single tube of thermal energy storage is **1.4256 Pa**

The total pressure drop in thermal energy of **220** tubes is **313.632 Pa.**

5.7.7 Pump Selection

An active system uses a pump or circulator to transport the hot water from the heat exchanger outlet to the parabolic trough solar collector to heat up again. In pressurized systems, the system is full of liquid and a circulator is operated to move hot water or heat-exchange liquid from the collector to the thermal energy storage.

Pumps are sized to overcome static and head pressure necessities in arrange to meet specific system design and performance flow rates.

Pump selection is based on different factors such as:

- ✓ Rate of delivery required (capacity)
- ✓ System types (direct and indirect)
- ✓ Heat collection fluid
- ✓ Operating temperature
- ✓ Required fluid flow rates
- ✓ Head required
- ✓ Friction losses
- ✓ Availability and easy maintenance

The power required for driving a pumping unit to achieve steam to demand can be:

$$P_{required} = \frac{\rho * g * Q * (H + S * L)}{\text{Pump efficiency}} \tag{5.109}$$

Where

$P_{required}$ – Rate of delivery required (capacity) in Watts ρ – density of fluid $(\frac{kg}{m^3})$ Q – volume flow rate $\frac{m^3}{s}$ H – static head(m) S = hydraulic gradient (m/km) and L = pipe length (m). $P_{required} = = 397.15$ W

Pump type – centrifugal pump (single-stage horizontal chemical pump)

Flow rate Flow: 2.2-480 m^3/h

Application - Chemical engineering, conveying for oil products, food, beverage, medicine, paper making, water treatment, environmental protection, some of the acid, alkali, salt, etc.

Rotating speed 1480 r/min or 2960 r/min, Head: 2.8-129 m, Motor power: 0.12-90 kW Maximum operating pressure: ≤1.6 MPa, Temperature of pumped - hot water

MOTOR

Type - 3 phase, Rated power 0.75 kW, Voltage: 380-415 V, Frequency 50 Hz, Poles 2 poles

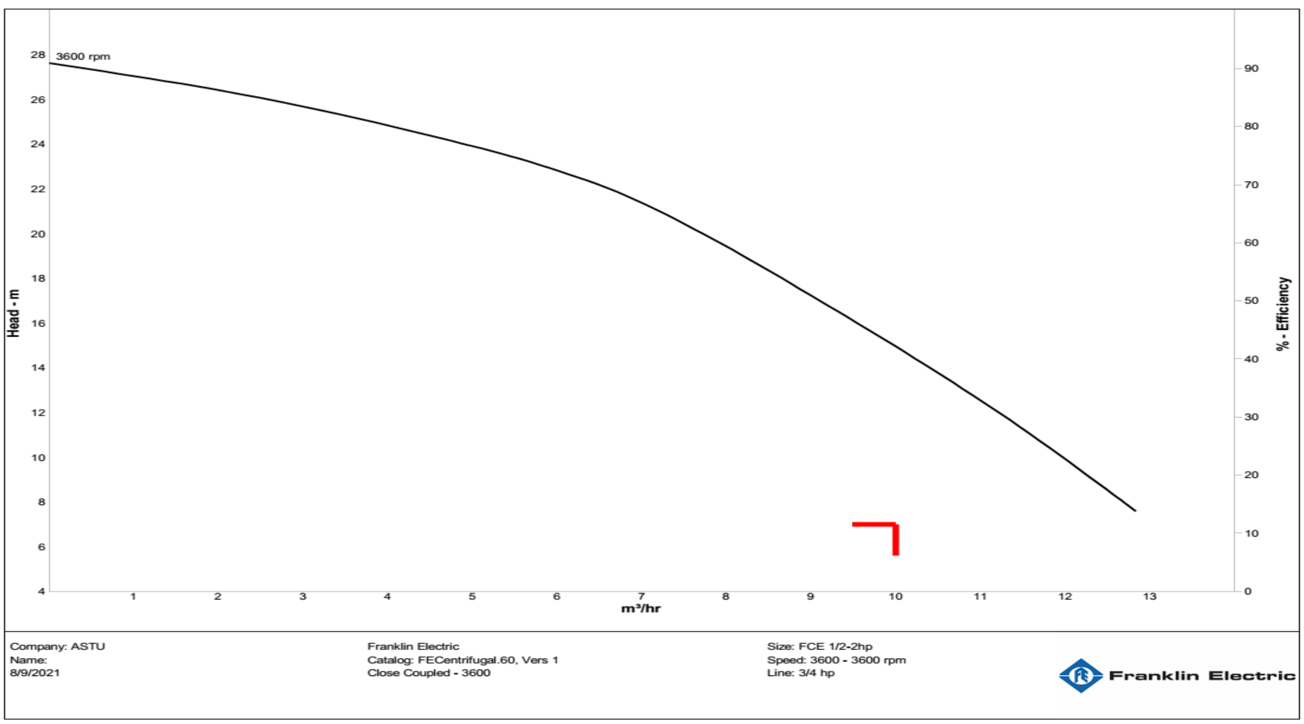

Figure 5. 12. Performance curve for the selected centrifugal pump model

CHAPTER SIX

RESULTS AND DISCUSSIONS

6.1 Introduction

Assela Malt factory is located near to Assela city in front of Kulumsa agricultural research center. All solar radiation data are taken from the east shewa metrological agency of Kulumsa station. The monthly average hourly beam radiation of each season is in the figure below. As the result shown below maximum beam solar radiation is recorded in the winter season (February 16, January 17, and December 10) respectively and minimum beam radiation is in the summer season (July 17 August 16 and June 11) respectively.

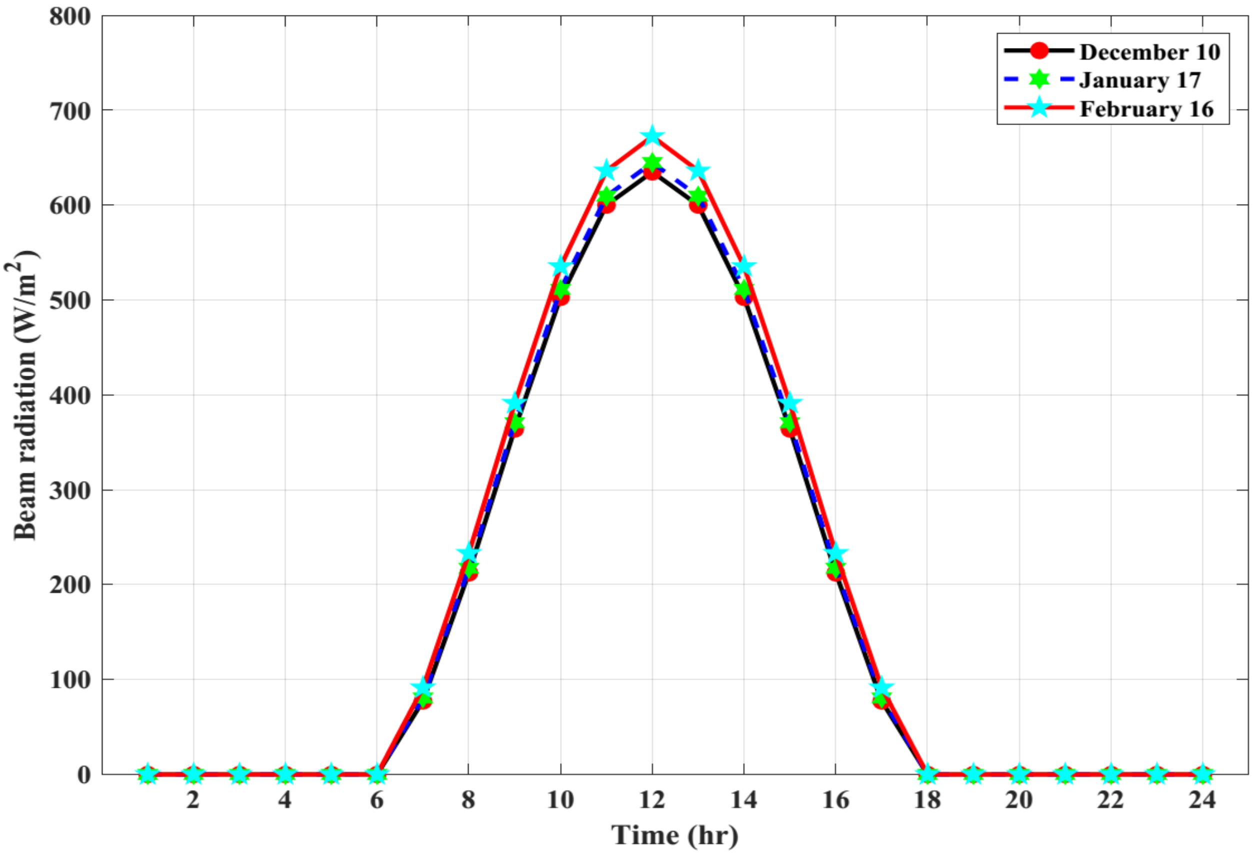

Figure 6. 1. Hourly beam incident solar radiation on horizontal surface for winter season

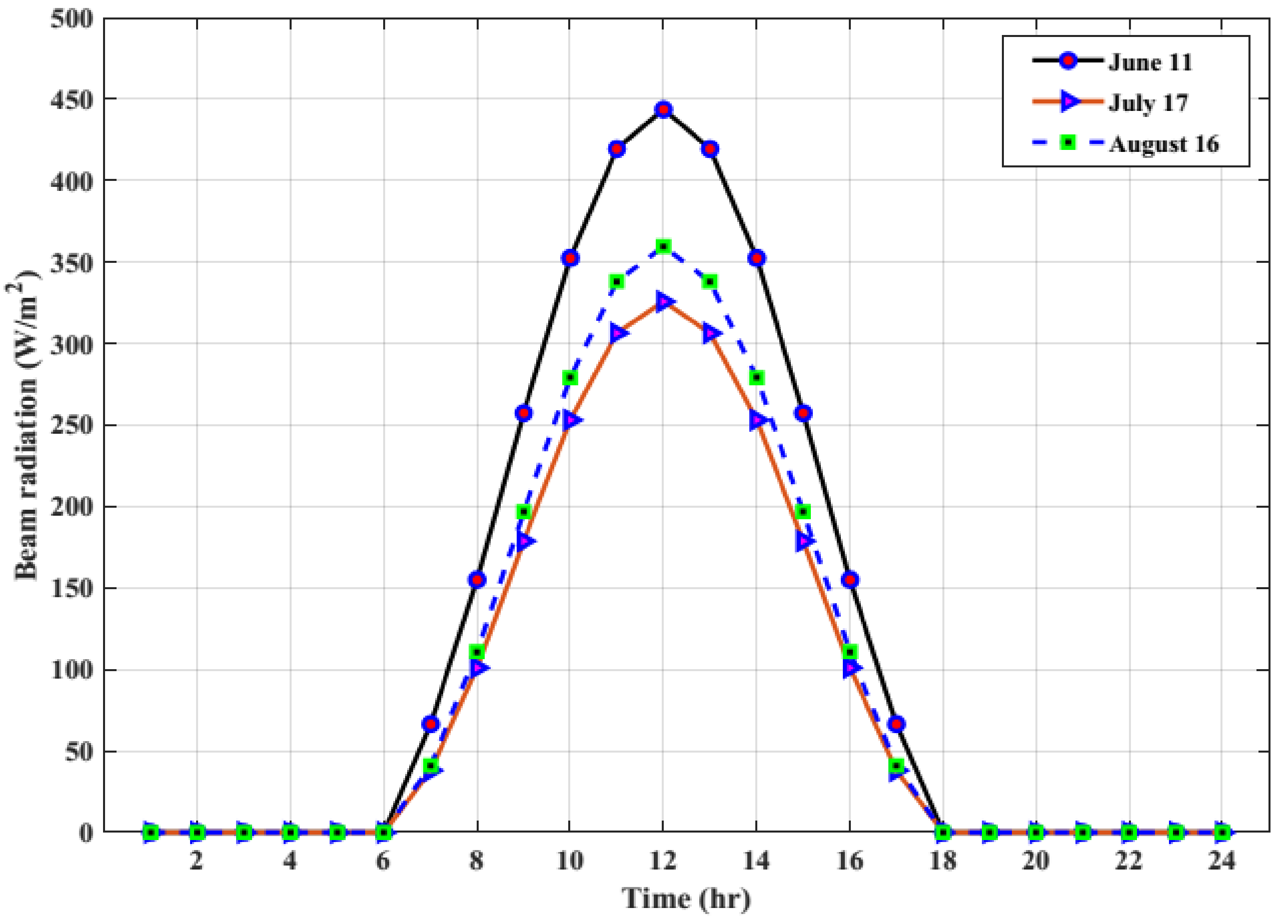

Figure 6. 2. Hourly beam incident solar radiation on horizontal surface for summer season

6.2 Temperature Outlet of Parabolic Trough Solar Collector (PTSC)

The temperature outlet of PTSC at Assela Malt factory different seasons are presented below. The mass flow rate of heat transfer fluid (HTF) is 0.05 $^{kg}/_{s}$ and an inlet temperature of heat transfer fluid is 398.47 K (125.27℃) in average. Maximum temperature outlet is in the winter season (February 16, January 17 and December 10) respectively. After HTF passed through four PTC connected in series maximum temperature is calculated is 557.7301K (284.58 ℃) in February month and minimum temperature outlet is 472.2377 K in July 17 month. The average maximum outlet temperature of each months in a year is 517.8016K (244.65℃).

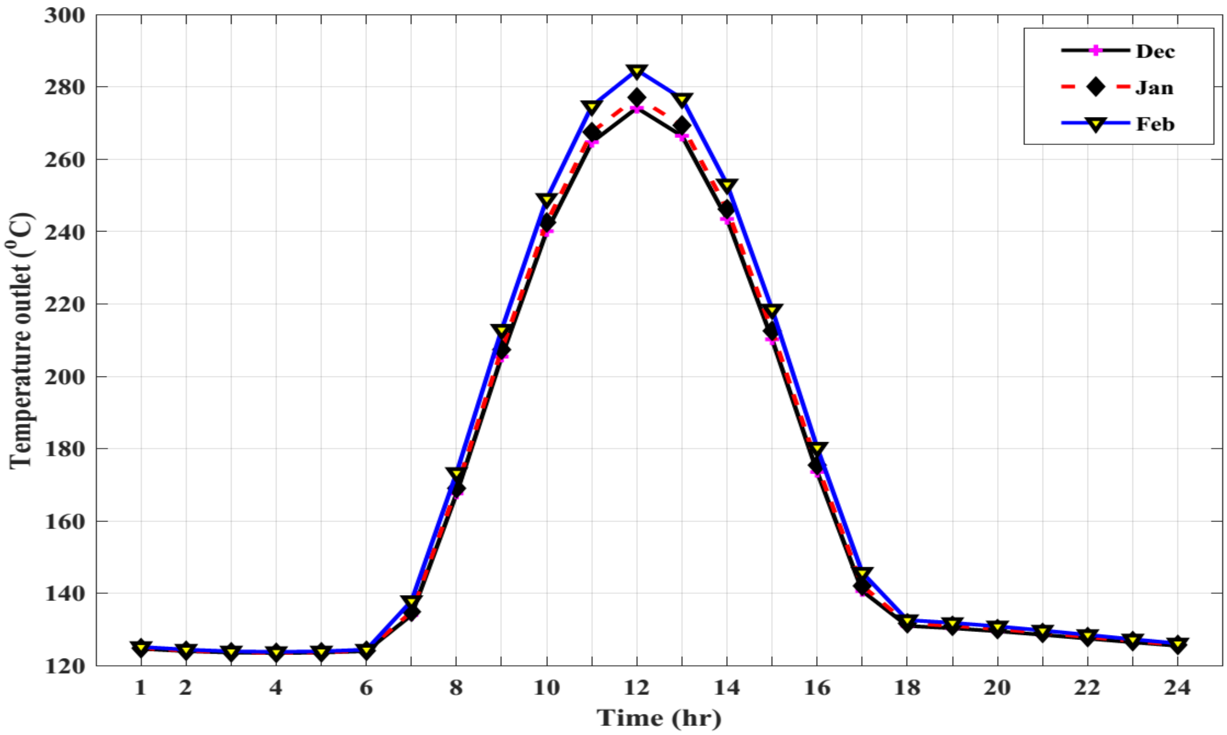

Figure 6. 3. PTC Hourly HTF outlet temperature of representative days in winter season

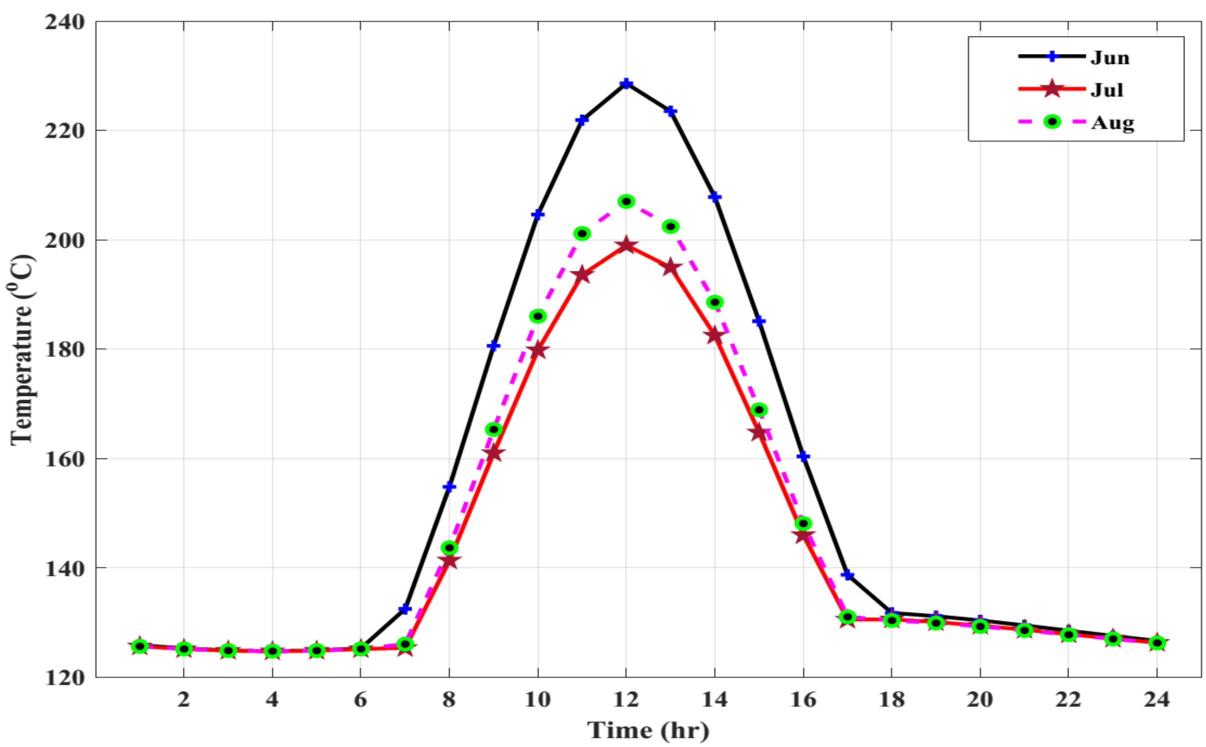

Figure 6. 4. PTC Hourly HTF outlet temperature of representative days in summer season

From above figures the temperature fluid continuously increases from sunrise (morning) to noontime and ranges a maximum, then declines slightly up to sunset hour. For another season, steam outlet temperature variations at the outlet of the parabolic trough solar collector (PTC).

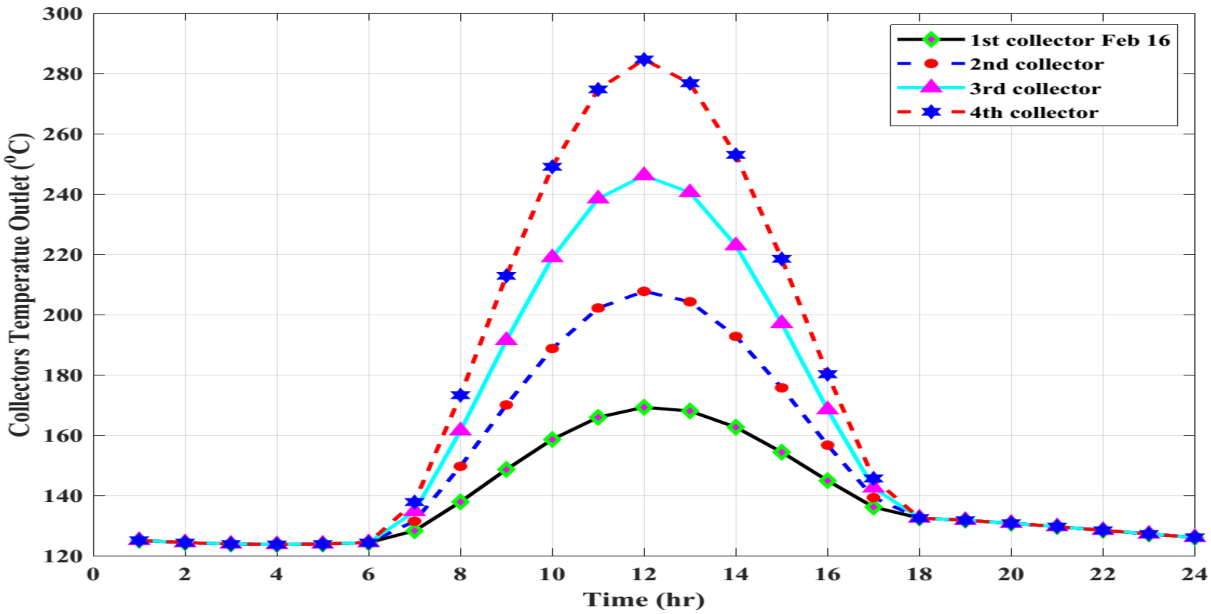

Figure 6. 5. Series PTSC Heat transfer fluid temperature outlet of February 16

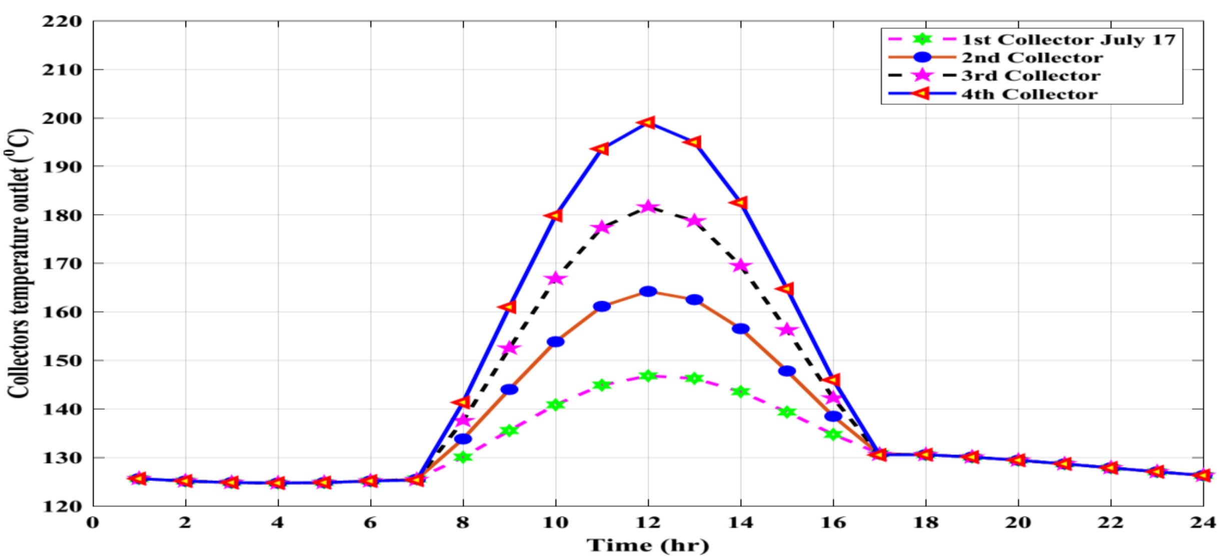

Figure 6. 6. Series PTSC temperature outlet of July 17

From figure 6.5 and 6.6 above represent the temperature of heat transfer fluid (HTF) of Feb 16 and July 16 respectively for four (4) collector in series which fulfill the temperature required at Assela Malt factory for steam supply to Malt kilning. The temperature outlet of the first collector is the inlet of the second collector and similarly the outlet temperature of the third collector is the inlet of the fourth collector. The mass flow rate in each collector is the same but the temperature increases from one collector to the next collector.

Parabolic trough solar collectors maximum temperature output in each months are presented in figure below.

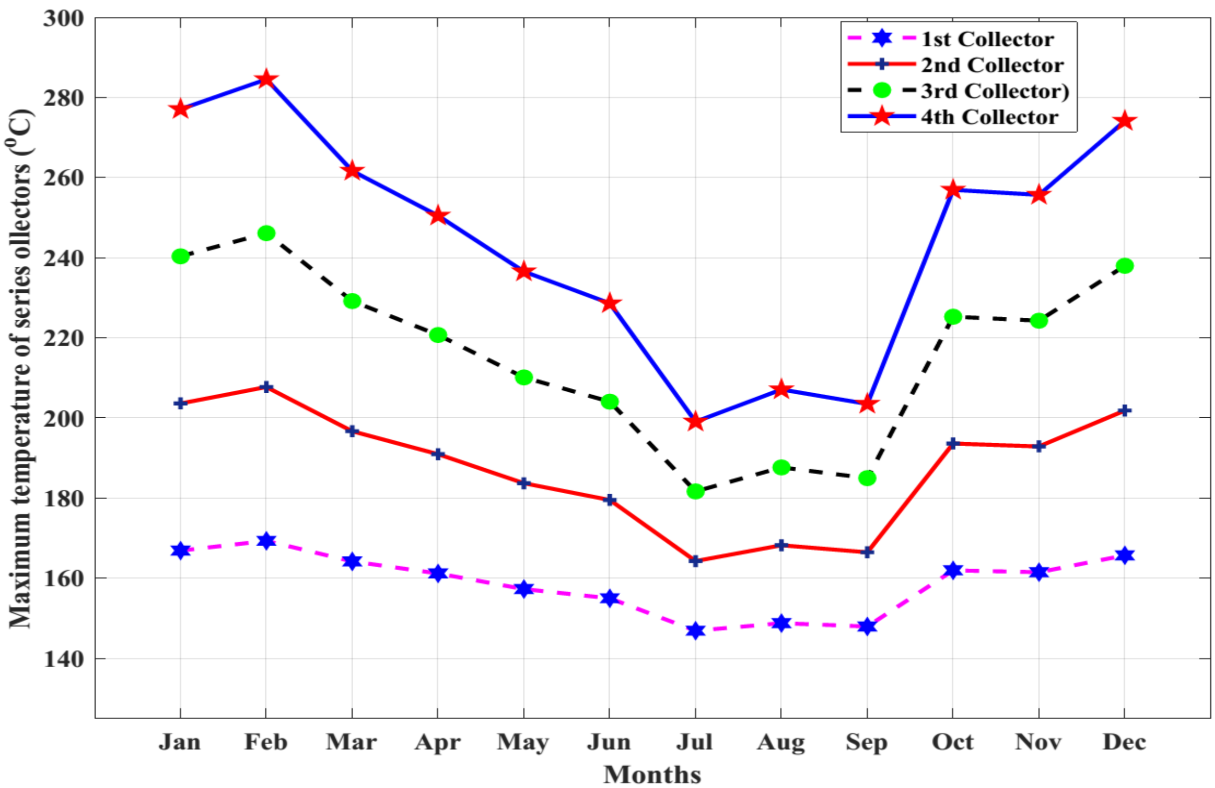

Figure 6. 7. Maximum temperature outlet of series PTSC in each months

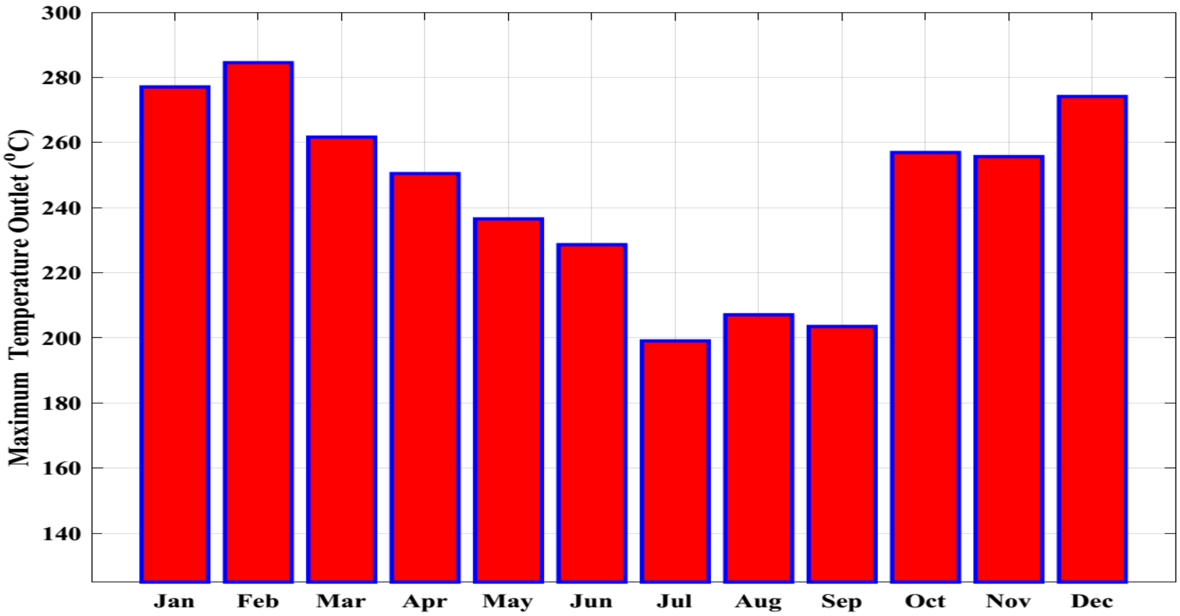

Figure 6. 8. Maximum HTF outlet temperature of PTSC in representative days in a year

6.3 Size Estimation of Parabolic Trough Solar Collector

In this thesis, for Assela Malt factory area required to fulfill thermal energy demand and number of collector required is estimated. In this study sizing of the number of collectors is based on the maximum temperature outlet. Since intensity of solar radiation is less in the summer season so it takes more area and number of collectors. Maximum area required is on July 17 area required is 2176 m^2 with 128 number of collectors. Minimum area required is on Febraury 16 area required is 986 m^2 with 58 number of collectors. The results of each months are tabulated in Table 6.1 below.

Table 6. 1. Number of collector and area required of PTSC needed in each months

Months	Number of collector	Area required to fulfill demand (m^2)
January 17	61	1037
February 16	58	986
March 16	69	1173
April 15	75	1275
May 15	85	1445
June 11	91	1547
July 17	128	2176
August 16	115	1955
September 15	120	2040
October 15	71	1207
November 15	71	1207
December 10	62	1054
Average	**84**	**1428**

By considering average of maximum temperature outlet of each month's Assela Malt Factory approximately around 84 parabolic trough solar collectors and **1428** $\boldsymbol{m^2}$ field area are required to fulfill the thermal energy demand.

6.4 Useful Energy Gain by Parabolic Trough Solar Collectors

Hourly useful heat energy gain from parabolic trough solar collectors are collected simultaneously calculated hourly from sun rise to sunset as shown in Figure 6.9, the energy collected usually high at noon time.

Conventional, solar energy delivered is found as outlet fluid temperature variation of PTC throughout the day times the temperature rise of the HTF to its mass flow rate and specific heat capacity of the fluid.

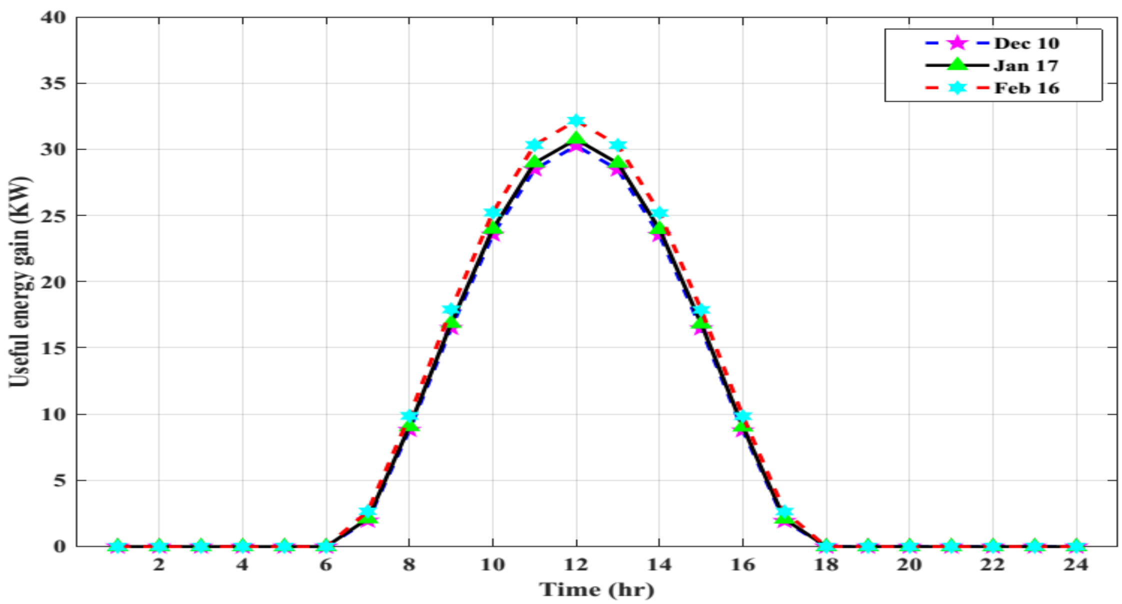

Figure 6. 9. Hourly useful energy gain of PTSC representative days of winter season

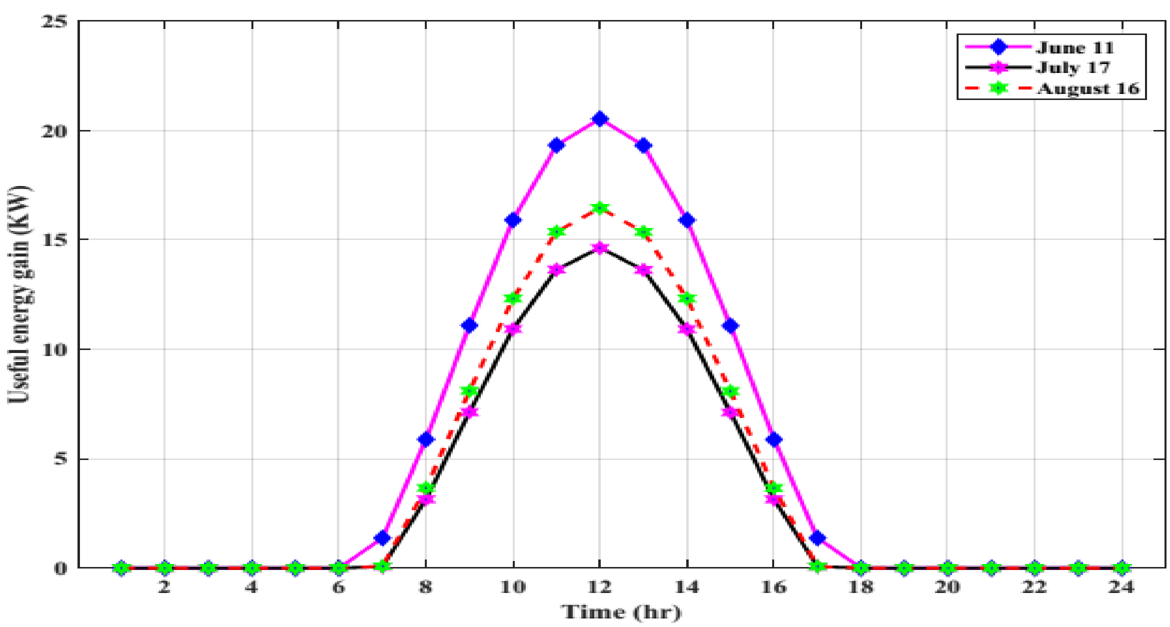

Figure 6. 10. Hourly useful energy gain of PTSC representative days of summer season

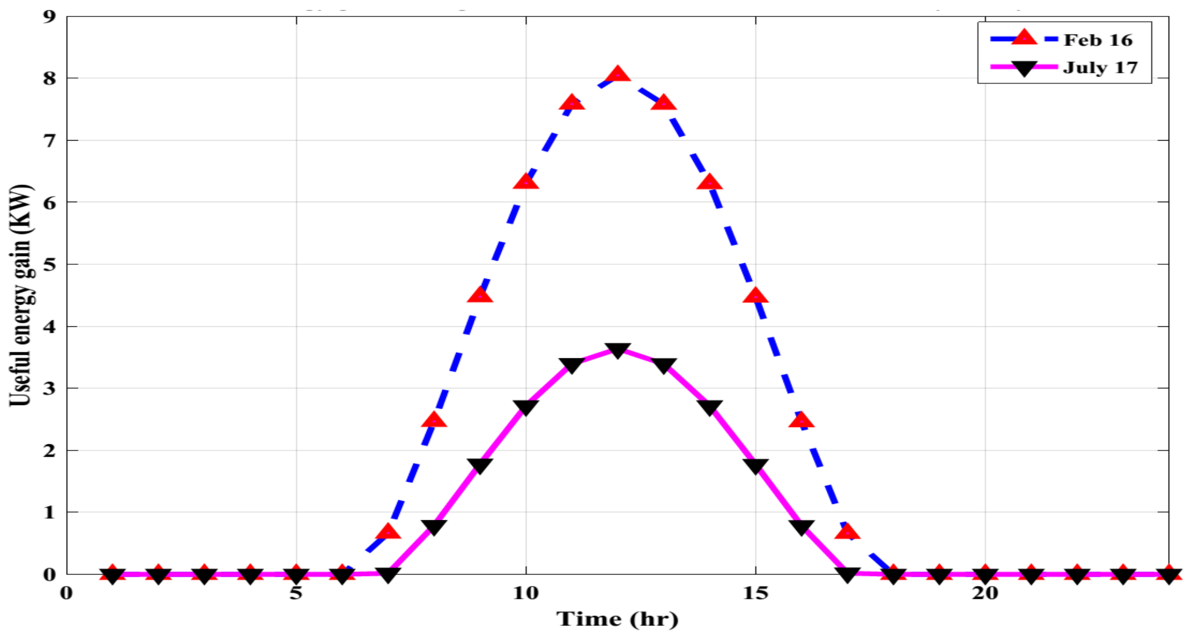

Figure 6. 11. Useful energy gain of single PTSC for maximum and minimum representative days in a year

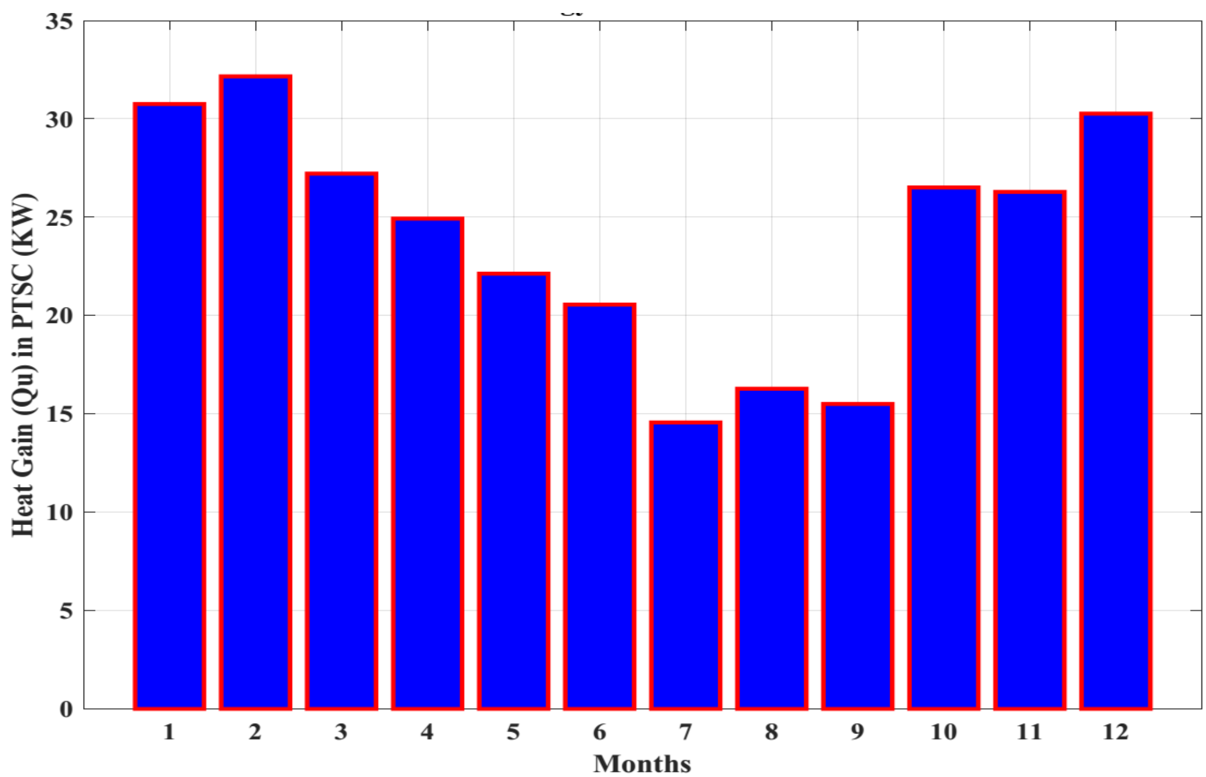

Figure 6. 12. Maximum useful energy gain of PTSC in each representative days in a months

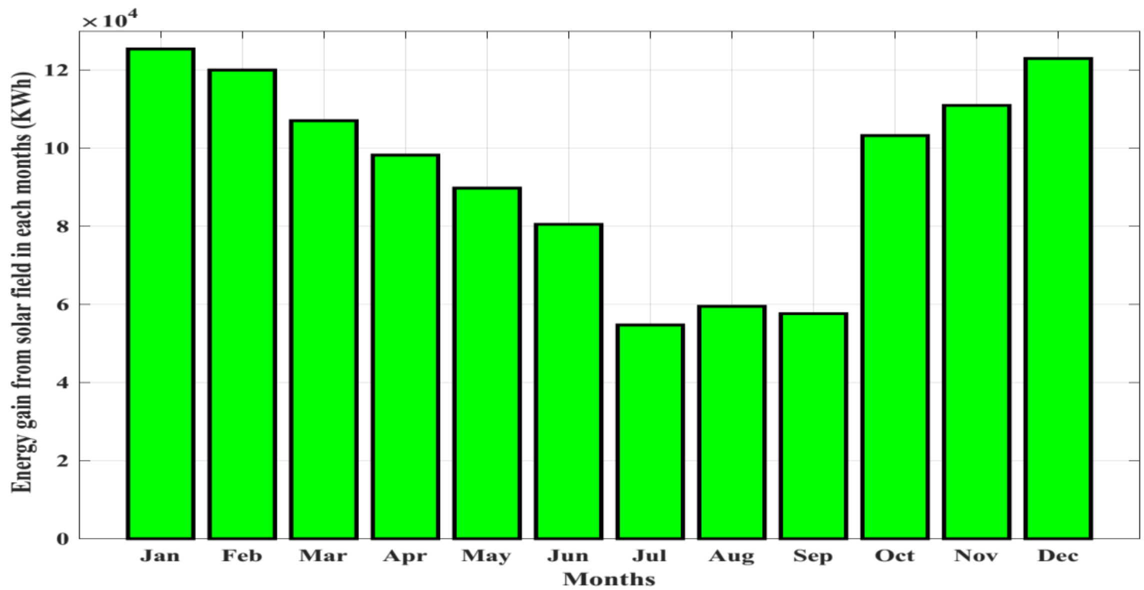

Figure 6. 13. Total useful energy gain of PTSC in a year

6.5 Optical Efficiency

Using the optical model developed in the previous chapter the maximum and minimum optical efficiency of the collector calculated is equal to 76.4 and 70.50 % respectively. The Figure 6.14 indicates that lowest and highest efficiency observed during June and September respectively.

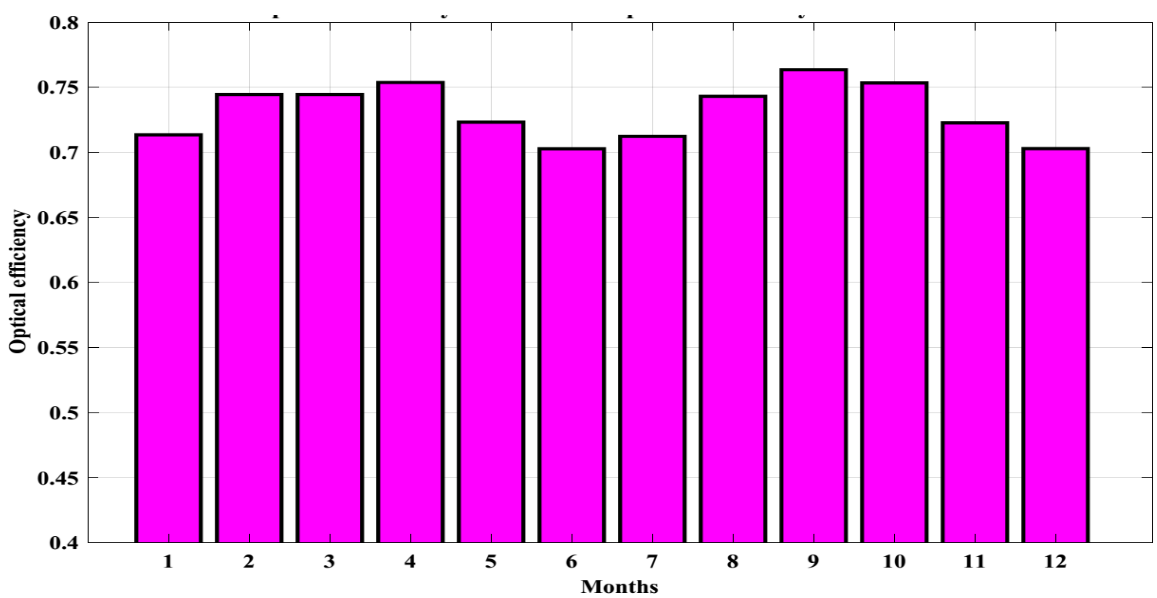

Figure 6. 14. Daily optical efficiency of PTSC for representative days of each month (Polar N-S axis with E-W tracking)

6.6 Instantaneous Thermal Efficiency

The instantaneous thermal efficiency of the solar collector depends on mass flow rate, the heat transfer fluid inlet and outlet temperature of the collector and beam solar radiation. Instantaneous total solar radiation incidence on collector surface and variation is from sunrise to sunset. Maximum and minimum thermal efficiency of PTC is recorded during Febraury 16 and July 17 respectively.

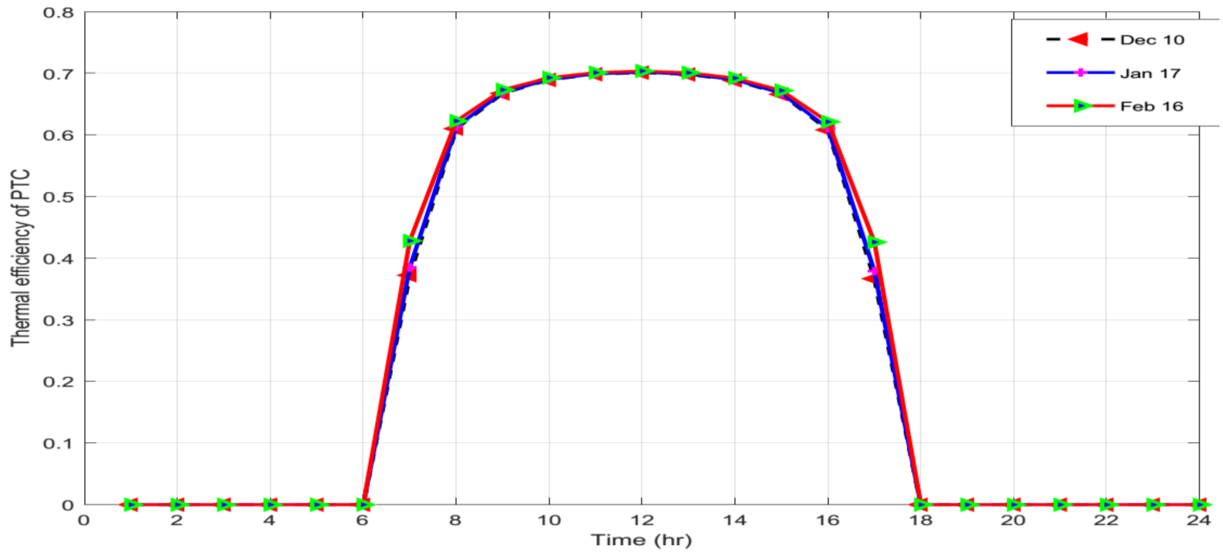

Figure 6. 15. Thermal efficiency of PTSC at representative days of winter season

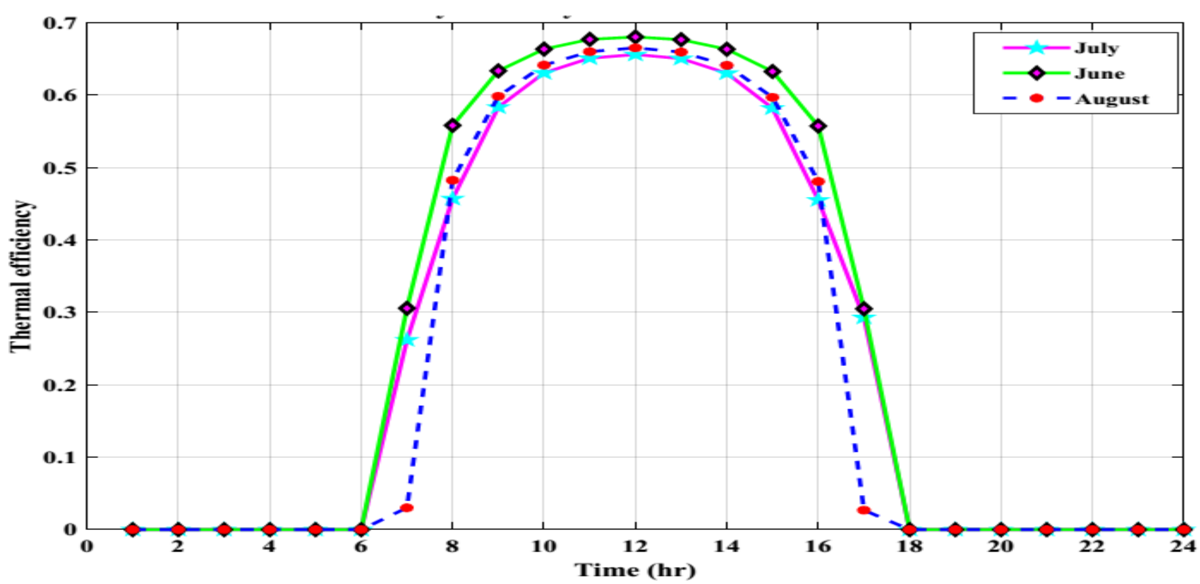

Figure 6. 16. Thermal efficiency of PTSC for summer season

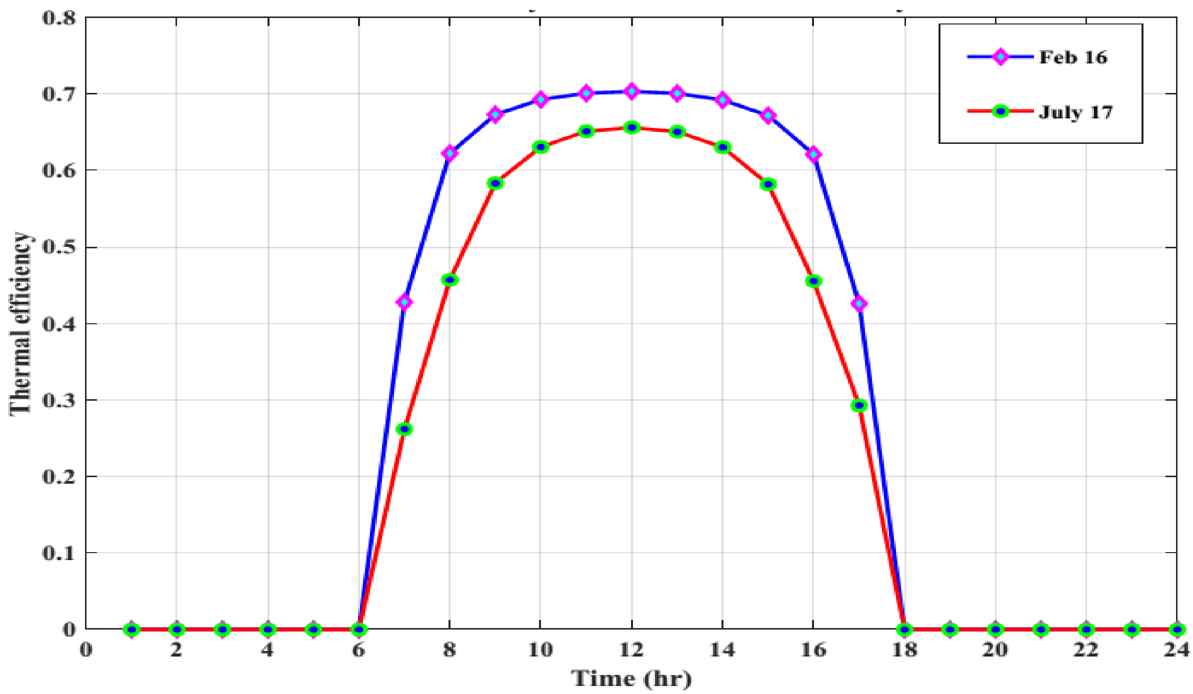

Figure 6. 17. Thermal efficiency of PTSC for maximum and minimum representative days in a months

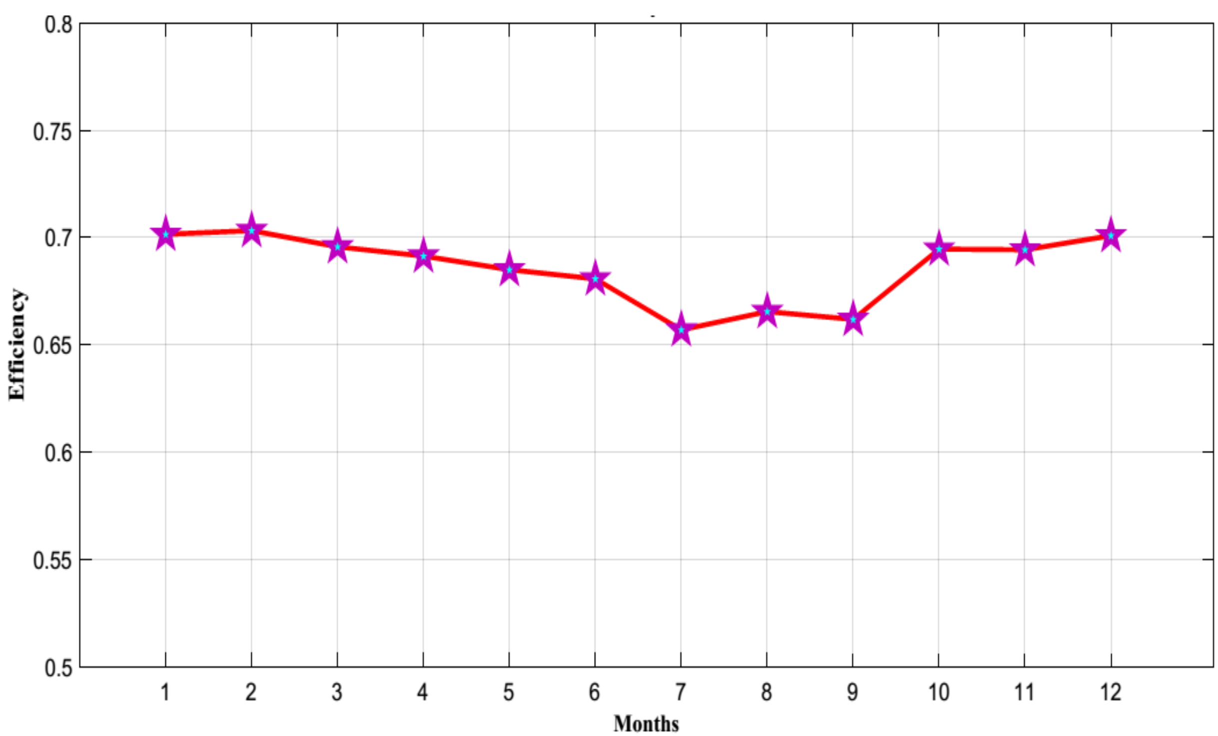

Figure 6. 18. Maximum thermal efficiency PTSC in each months

6.7 Charging Process of Phase Change Materials

The variation of phase change materials (D- mannitol) temperature throughout charging processes is studied with variation of HTF throughout the day at inlet point. The inlet temperature of HTF is almost same as outlet temperature of HTF from the solar collector. Initially, the temperature of PCM is assumed as the same as the ambient temperature and the temperature of HTF initially, have the same temperature with the temperature of HTF at the outlet of heat exchanger which is almost 125 degree Celsius. Then, the melting process is occurs with sensible heating initial point for two hour and thirteen minutes. During melting process, phase change process happens within a slightly temperature range 0.5-1.5 ℃. The melting process occurs approximately for five and half-hours' of time duration. After D-mannitol phase change process ends, simultaneously sensible heating continues. To solve the governing equation a finite difference method (FDM) was implemented by using the MATLAB pdepe solver.

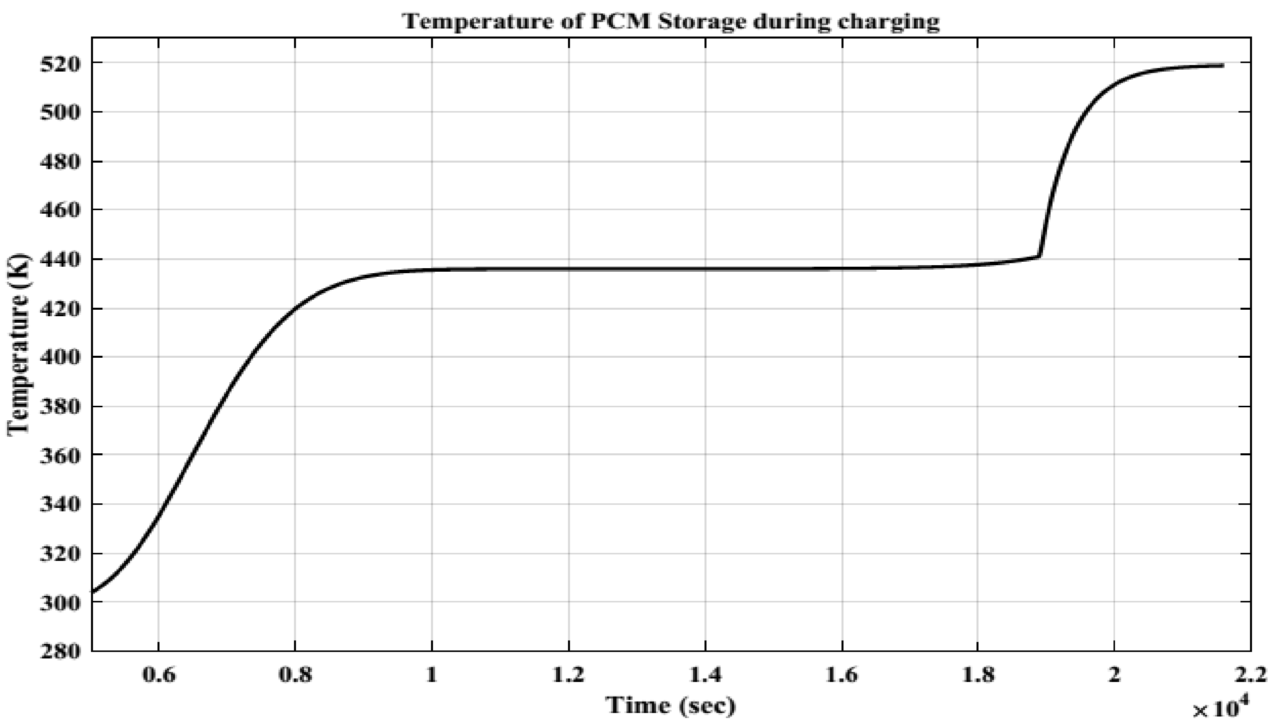

Figure 6. 19. Charging process of D-mannitol phase change material

From a simulation and modeling thermal storage tank with integrating PCM, the total volume required to integrate D-mannitol is 5.05 m^3 i.e. the total volume needs to fill the D-mannitol. The D-mannitol filled in shell or concentric cylindrical shape on outer surface of the tube and a porosity (ε= 0.45), through which steam (HTF) flows. Hence the storage unit is shell filled by PCM has a volume of 5.05 m^3 and a single tube with 0.007634 m^3 which HTF is flow through it. The total number of tube used to fulfill the required thermal energy demand is approximately 220.

6.8 Temperature and Heat Gain Effect on PTSC With and Without Integrating PCM

Since during night time there is no intensity of solar radiation integrating with and without PCM for Assela Malt factory in kilning process is presented below.

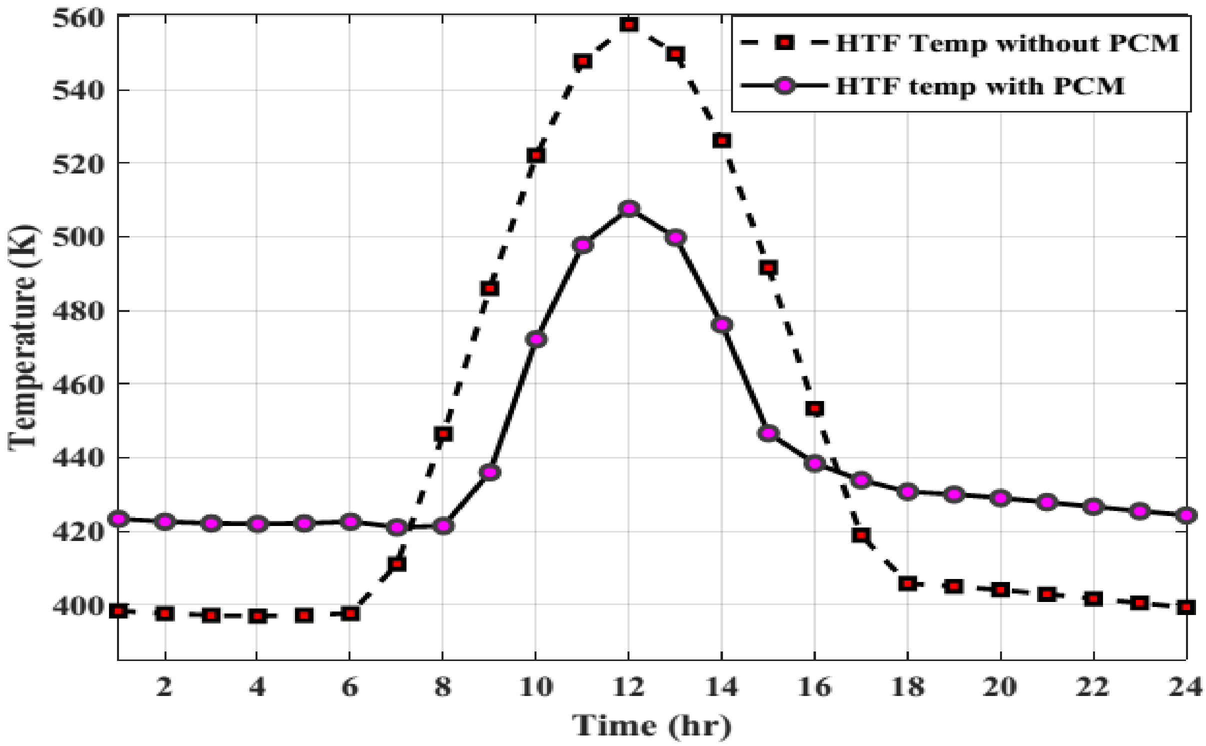

Figure 6. 20. Effect of PCM on temperature outlet variation of PTSC integrated with and without phase change materials for February 16

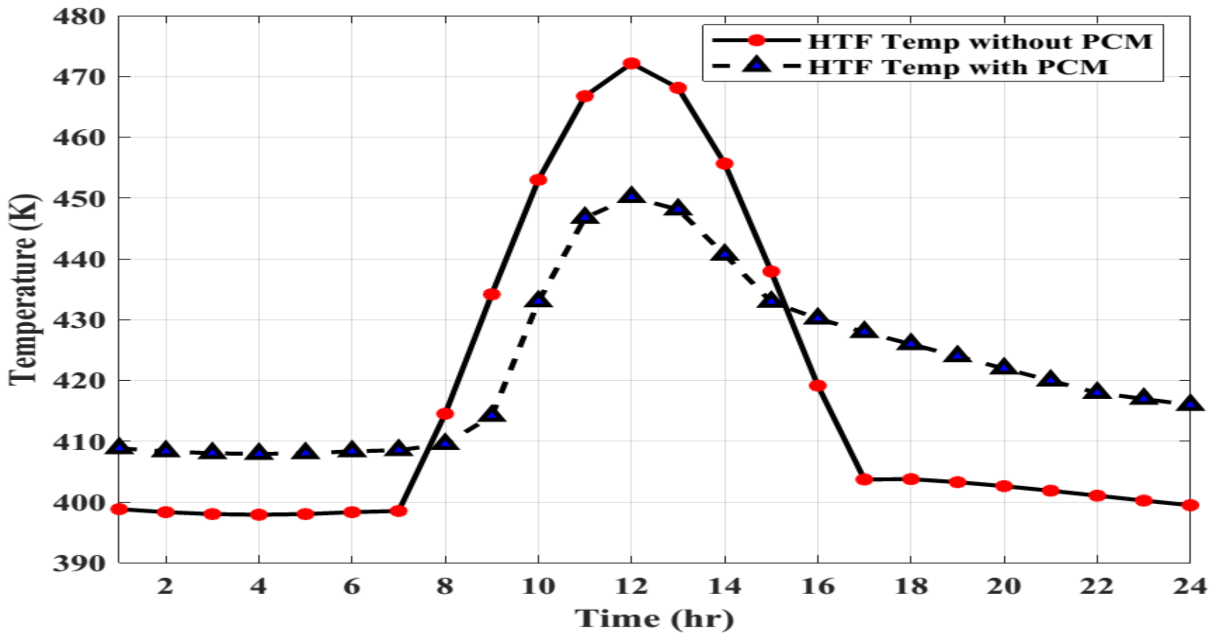

Figure 6. 21. Effect of PCM on temperature outlet variation of PTSC integrated with and without phase change materials for July 17

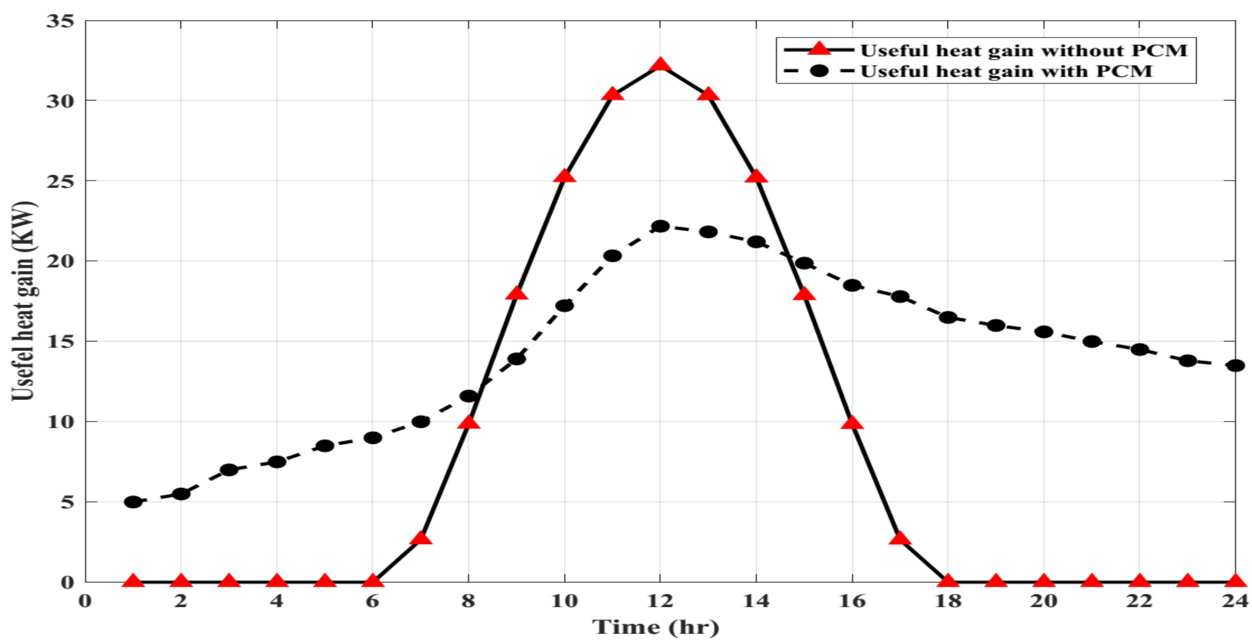

Figure 6. 22. Effect of PCM on useful heat gain of PTSC integrated with and without phase change materials for February 16

6.9 Validation

To approve the reliability of parabolic trough solar collector (PTSC) the numerical model, the mathematical results are related with the previously published journal articles. (Lamrani & Draoui, 2018) Investigated numerically parabolic trough solar collector thermal performance, outlet temperature and its shape are in good agreement with this study.

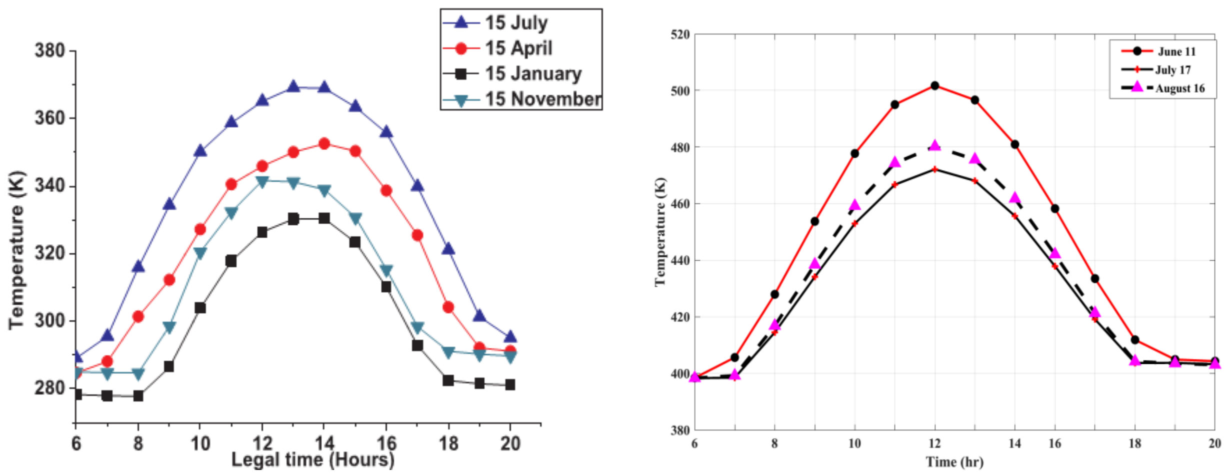

Figure 6. 23. (a) Numerical validation of parabolic trough solar collector for four representative days (Lamrani & Draoui, 2018) and (b) PTC for summer season at Assela Malt factory respectively

To confirm the reliability of the numerical model, the mathematical results are related with the previously published journal articles. (Shibahara et al., 2015) studied, the melting of d-mannitol experimentally and numerically to build a fundamental database of the waste heat recovery system for ships. Experimentally, the melting temperature of d-mannitol was measured under various conditions. Moreover, the thermal analysis was carried out by thermogravimetric (TG) analysis and differential thermal analysis (DTA) in order to determine the melting temperature for subsequent numerical simulation. The numerical simulation was conducted by using a commercial CFD code, ANSYS FLUENT, to clear up the melting progression and heat transfer characteristics of d-mannitol as the phase change materials. The results have similar shape graphically with the published one but there is difference in melting time and heat energy amount which depends on the geometric size of latent heat storage system.

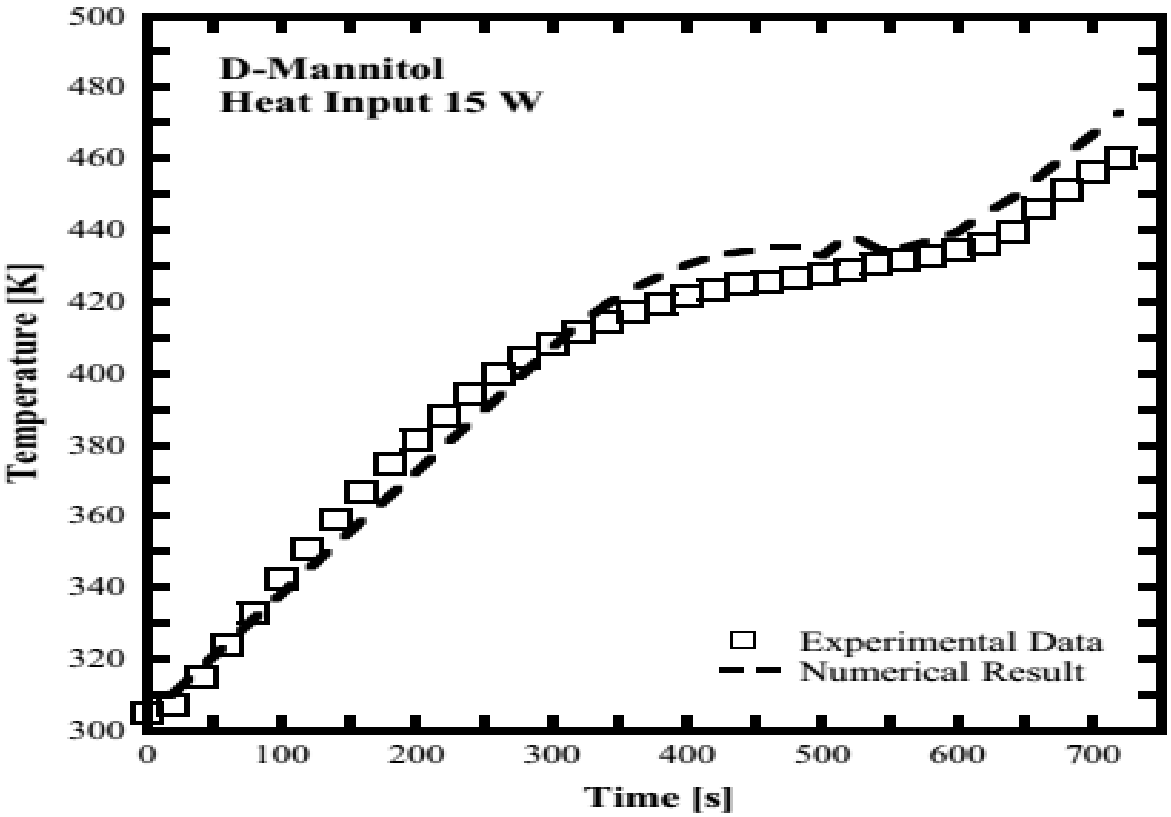

Figure 6. 24. Numerical and experimental validation of D-mannitol phase change material during charging process (Shibahara et al., 2015).

CHAPTER SEVEN

CONCLUSIONS AND RECOMMENDATIONS

7.1 Conclusions

In this study performance of parabolic trough solar collector integrated with phase change materials (latent thermal energy storage) to supply steam for Malt kilning at Assela Malt factory is investigated. Assela Malt factory one of the top Malt supplier factory in Ethiopia which used electric boiler for steam supply in Malt kilning. This study focus on using renewable solar energy as alternative energy source for Assela Malt factory. Depends on energy demand for steam supply at Assela Malt factory parabolic trough solar collector and latent thermal energy storage size is designed.

In this thesis, simulation performance analysis of a parabolic trough steam supply integrated with phase change materials has been done for Assela Malt Factory. One dimensional model was developed to analysis parabolic trough solar collector and the heat transfer in latent thermal energy storage. The simulation was conducted using MATLAB software and Microsoft Excel package. Transient mathematical model was developed and solved using a finite difference method implemented by using the MATLAB pdepe solver. Currently, the factory needs maximum steam (steam supply) 10,000 kg/hr.

Generally from numerical simulations by considering average of maximum temperature outlet of each month's to fulfill thermal energy demand of Assela Malt factory approximately around 84 number of parabolic trough solar collectors (1428 m^2 field area) of $0.05 \frac{kg}{s}$ mass flow rate of HTF are required. To substitute the gap during night time mass of 4139kg of D-mannitol (phase change materials) and 220 number of HTF tubes each tube has 0.06m diameter and 2.7m length are required. Maximum optical efficiency of the parabolic trough is 76.4% and the maximum thermal efficieny of PTSC is 70%.

7.2 Recommendations

As the results from this thesis it is recommended that:

- If concentrated solar steam generation (parabolic through solar collector integrated with PCM) is implemented for Asella Malt factory, the electric consumption and operational cost of the boiler can be reduced.
- It is thus recommended that the Oromia farmers' cooperative union and Asella Malt factory board members should consider this outcome for its implementation so as to overcome the high operational cost of the existing boiler by using the parabolic trough collector steam generation system.
- Solar intensity during summer season at Kulumsa station (Assela Malt factor) is too low so it is recommended that using electric boiler as alternative additional heat sources.

This Research is done under grant number ASTU/SM-R/334/21

References

Alvaro de Gracia, L. F. (2016). Numerical simulation of a PCM packed bed system: A review. *science direct*, 1-29.

Amir Shahsavari, M. A. (2018). Potential of solar energy in developing countries for reducing energy-related. *Renewable and Sustainable Energy Reviews*, 275–291.

Arun Kumar, S. S. (2015). A Review on Thermal Energy Storage Unit for Solar Thermal Power Plant Application DOI:10.1016/J.EGYPRO.2015.07.728. *Energy procedia*, 32-35.

Ashish K. Sharma, C. S. (2017). Solar industrial process heating: A review. *Renewable and Sustainable Energy Reviews*, 124–137.

Ashraf E. Elmohlawy, B. I. (2018). Modeling and Performance Prediction of Solar Parabolic Trough Collector for Hybrid Thermal Power Generation Plant under Different Weather Conditions. *Journal of Renewable and Sustainable Energy*, 2-10.

Babajide, s. a. (2016). an investigation of an oil/packed bed thermal energy storage system using phase change material for domestic cooking. *A thesis submitted in fulfillment of the requirements for the degree of Doctor of Philosophy in Physics at the Northwest University, South Africa*, 20-35.

Beckman, J. A. (2013). *Solar Engineering of Thermal Processes Fourth Edition.* USA: John Wiley & Sons, Inc., Hoboken, New Jersey.

Bekele, A. (2007). Large scale application of solar water heating system in ethiopia. *A thesis submitted to the School of Graduate Studies of Addis Ababa University in partial fulfillment of the Degree of Masters of Science in Mechanical Engineering* , 80-95.

Chaves, J. R. (2019). Concentrated Solar Power: A comparison and evaluation of innovative parabolic trough collector concepts for large scale application. *Master thesis*, 1-126.

Dakuri Arjun and J. Hayavadana. (2014). Thermal energy storage materials (PCMs) for textile applications. *Journal of T extile and Apparel, T echnology and Management*, 12-13.

Evangelos Bellos, C. T. (2018). Alternative parabolic trough solar collectors – A review. *Progress in Energy and Combustion Science*, 1-73.

Franz Mauthner, M. H. (2013). Manufacture of Malt and beer with low temperature solar. *International Conference on Solar Heating and Cooling for Buildings and Industry* (pp. 1189-1193). Freiburg, Germany: ScienceDirect.

Gaosheng Wei, G. W. (2017). Selection principles and thermophysical properties of high temperature phase change materials for thermal energy storage: A review. *ScienceDirect /Renewable and Sustainable Energy Reviews/*, 50-53.

Ghodbane, b. (2016). a numerical analysis of the energy behavior of a parabolic trough concentrator. *Journal of Fundamental and Applied Sciences*, 1-21.

Jose Pereira da Cunha, P. E. (2016). thermal energy storage for low and medium temperature applications using phase change materials - a review. *Science direct*, 1-22.

Kalogirou, S. A. (2012). A detailed thermal model of a parabolic trough collector receiver. *www.elsevier.com/locate/energy*, 298-306.

Kalogirou, S. A. (2014). *Solar Energy Engineering Processes and Systems.* USA: 1-815.

Kantole. (2012). Modelling and design of a latent heat thermal storage system with reference to solar absorption refrigeration. *Phd dessertation* , 1-93.

Karina Fullenkamp, M. M.-L. (2018). Review and selection of EPCM as TES materials for building applications. *International Journal of Sustainable Energy,* 23-25.

Lamrani, K. ,., & Draoui. (2018). Mathematical modeling and numerical simulation of a parabolic trough collector: A case study in thermal engineering. *Thermal Science and Engineering Progress,* 47-54.

M. Hauner, K. E. (2019). Model calculation of a solar assisted system for a Malt kiln. *BrewingScience,* 18-30.

M. Hauner, K. E. (January / February 2019 (Vol. 72)). Model calculation of a solar assisted system for a Malt kiln. *BrewingScience,* 18-30.

Makoto Shibahara, Qiusheng Liu and Katsuya Fukuda. (2015). Heat transfer characteristics of d-mannitol as a phase change material for a medium thermal energy system. *Heat Mass Transfer*, 5-7.

Matthias Günther, M. J. (2011). Parabolic Trough Technology. In A. C. Materials, *Parabolic Trough Technology* (pp. 1-105). Kassel: Institute for Electrical Engineering, Rational Energy Conversion, University of Kassel,.

Mesfin, M. (2009). Modeling, Simulation and Performance Evaluation of Parabolic Trough Solar Collector Power Generation System. *A thesis submitted to the School of Graduate Studies of Addis Ababa University in partial fulfillment of the requirements of the Degree of Masters of Science in Mechanical Engineering (Thermal Engineering Stream),* 1-85.

Odeh, S. D. (1999). Direct Steam Generation Collectors For Solar Electric Generation Systems . *A thesis submitted to the University of New South Wales in fulfillment of the requirements for the degree of Doctor of Philosophy* , 1-173.

Qianjun Mao, N. L. (2018). Recent Investigations of Phase Change Materials Use in Solar Thermal Energy Storage System. *Hindawi Advances in Materials Science and Engineering*, 1-13.

Raghurajsinh, B. a. (2016). Performance of an evacuated tube collector with heat pipe technology. *International Journal of engineering research and general Science*, 114-135.

Reta, B. (2020). Investigating the Performance of Parabolic Trough Solar Collector with Thermal Energy Storage System for Injera Baking Applications. *Msc thesis at Adama Science and Technology University*, 32.

Rojas, R. B. (2017). Feasibility study of D-mannitol as phase change material for thermal storage. *AIMS Energy*, Volume 5, Issue 3, 404-424.

S. Mekhilef, R. S. (2011). A review on solar energy use in industries. *Renewable and Sustainable Energy Reviews*, 1777–1790.

S. Saeed Mostafavi Tehrani, R. A. (2016). Design and feasibility of high temperature shell and tube latent heat thermal energy storage system for solar thermal power plants. *Renewable Energy*, 120 -136.

Sabiha. M., S. R. (2015). Progress and latest developments of evacuated tube solar collectors. *Renewable and sustainable energy reviews*, 1038-1054.

Shahzada Zaman Shuja, B. S.-Q. (2019). Thermal Assessment of Selective Solar Troughs. *MDPI*, 1-20.

Tiwari, G. T. (2016). *Handbook of Solar Energy Theory, Analysis and Applications.* India: Energy Systems in Electrical Engineering.

Tzivanidis, E. B. (2018). Analytical Expression of Parabolic Trough Solar Collector Performance. *MDPI*, 1-17.

Yune, H. (2019). Investigating the Thermal Performance of a Solar Water Heating System Integrated with Phase Change Material as a Thermal Energy Storage: A Case of Adama Hospital Medical College. *M.Sc. Thesis* , 37-40.

Zhaowen Huang, X. G. (2018). Characterization of medium-temperature phase change materials for solar thermal energy storage using temperature history method. *Solar Energy Materials and Solar Cells*, 152-160.

Ziye Linga, G. Z. (2015). Performance of a coil-pipe heat exchanger filled with mannitol for solar water heating system. *The 7th International Conference on Applied Energy – ICAE2015* (pp. 827 – 833). China: www.sciencedirect.com.

APPENDIX

Annex A: Hourly beam solar radiation

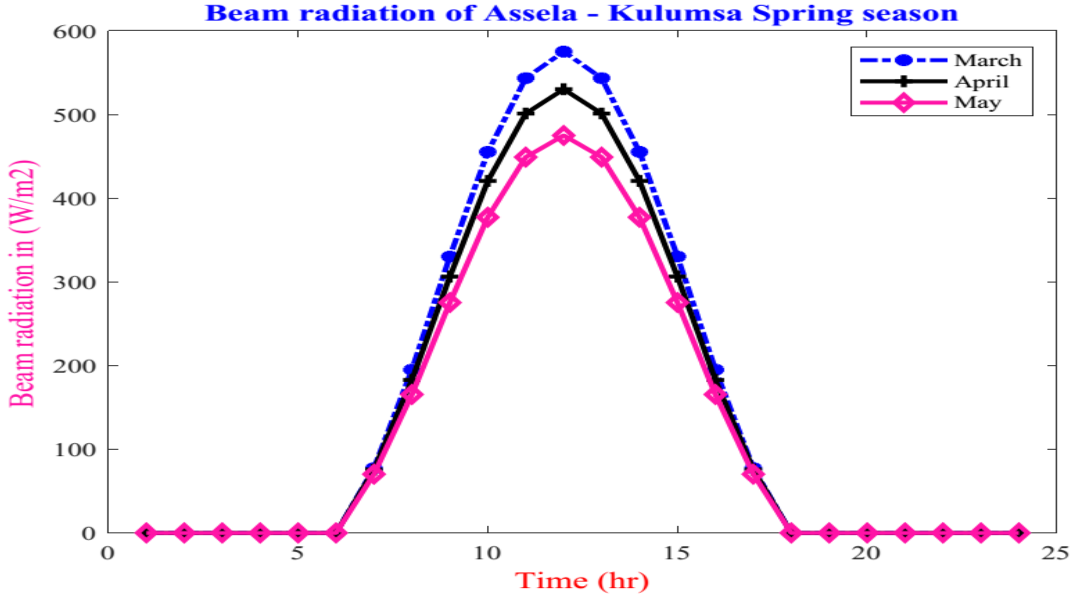

Figure A.0. 1. Hourly beam incident solar radiation on Horizontal surface for spring season

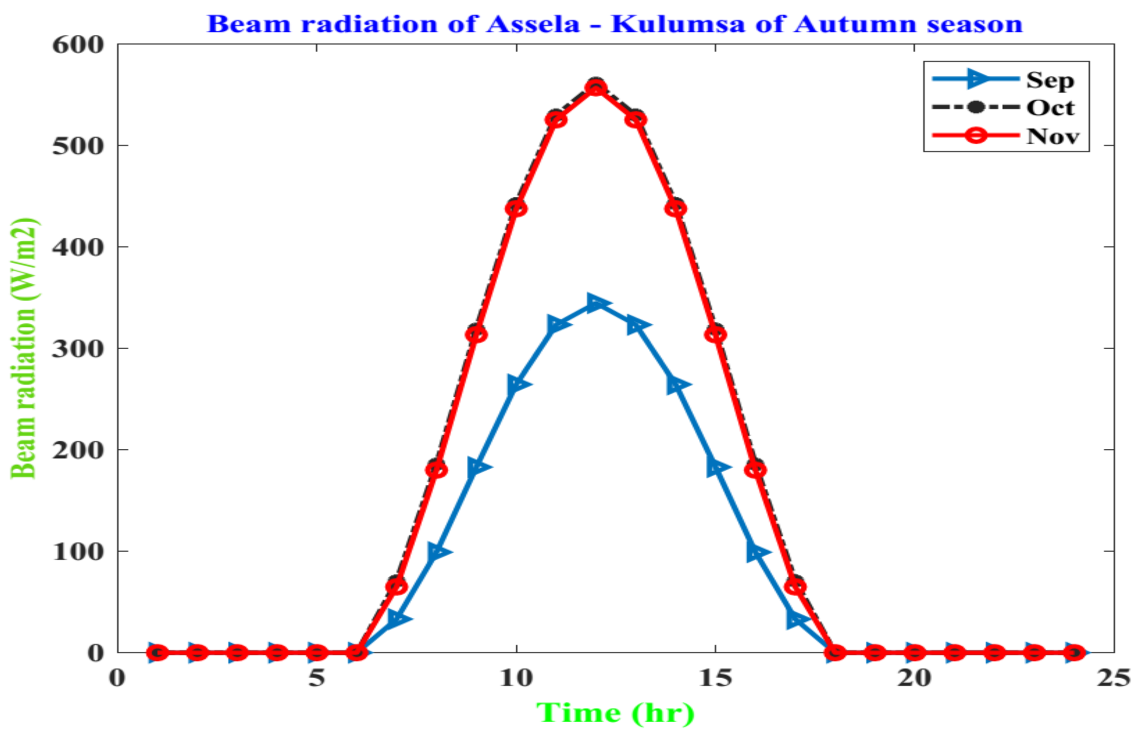

Figure A.0. 2. Hourly beam incident solar radiation on Horizontal surface autumn season

Annex B: Hourly HTF Temperature outlet variation

Maximum parabolic trough solar collector HTF temperature out let of each months at mass flow rate 0.05kg/s.

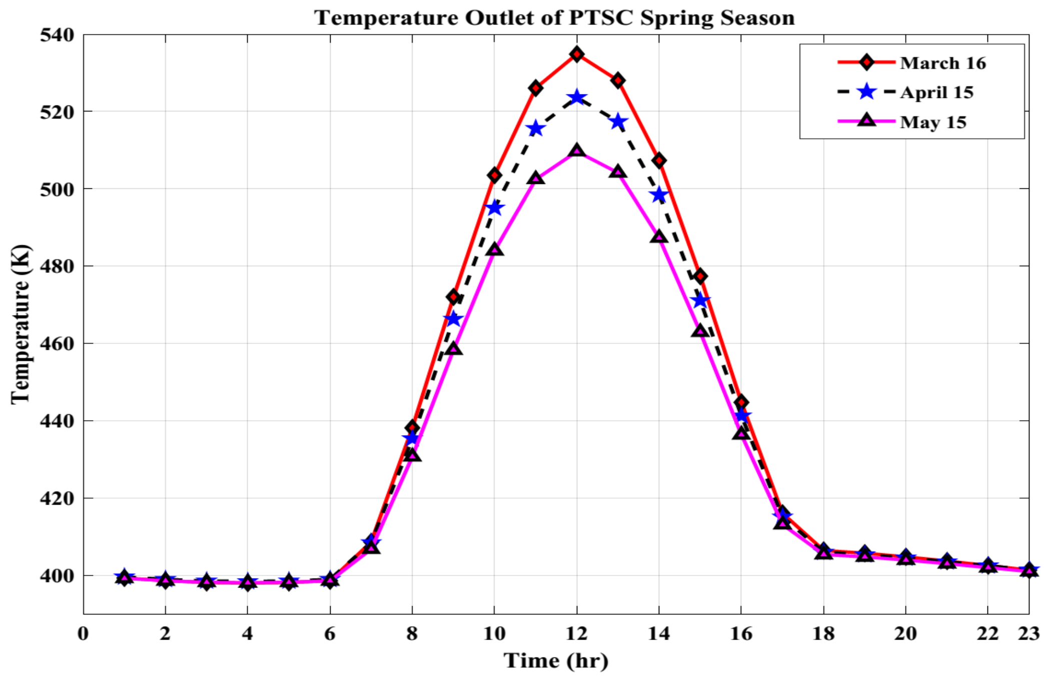

Figure B.0. 1. PTC Hourly HTF outlet temperature of representative days in spring season

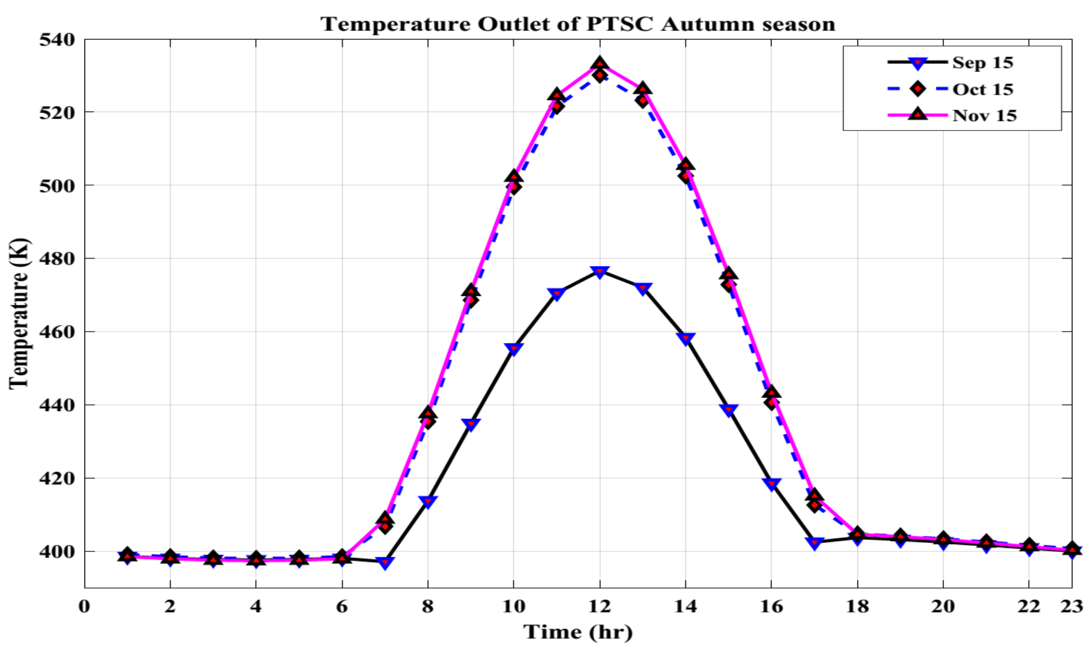

Figure B.0. 2. PTC Hourly HTF outlet temperature of representative days in autumn season

Table B .0. 1. PTC temperature outlet, heat gain and number of collector required for Assela Malt Factory

Months	**Temperature outlet(K)**	**Heat gain in each collector(KW)**	**Number of collector required**
January 17	550.2815	30.76675566	60.46682
February 16	557.8177	32.16599074	57.82085
March 16	534.8774	27.21843004	68.3065
April 15	523.6691	24.93185788	74.57564
May 15	509.6995	22.13077799	84.034
June 11	501.7726	20.55754706	90.47921
July 17	472.1853	14.56694861	127.7676
August 16	480.2186	16.28227284	114.3153
September 15	476.6772	15.51296969	119.9772
October 15	530.1561	26.51895448	70.14234
November 15	533.1871	26.29649891	70.74584
December 10	547.3476	30.27275112	61.46522
AVERAGE	**518.1575**	**23.93514625**	**83.34138**

Annex C: Hourly useful heat gain for spring and autumn season

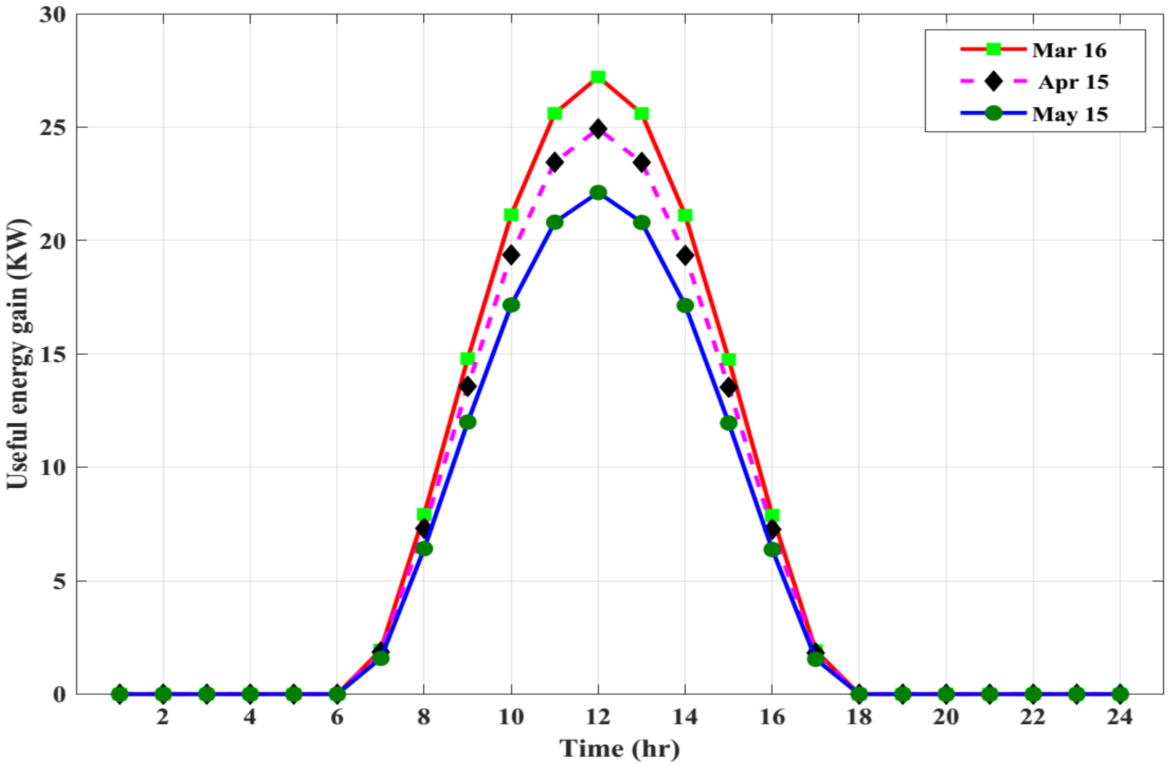

Figure C.0.1. Hourly useful heat gain form PTSC for spring season

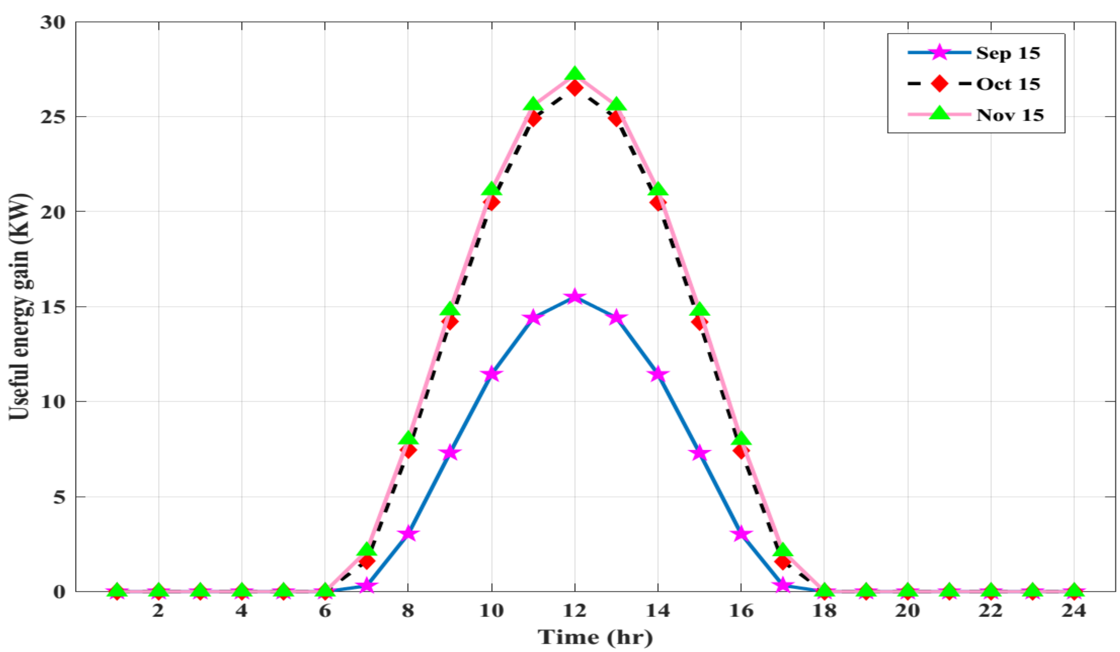

Figure C.0 2. Hourly useful heat gain from PTSC for autumn season

Annex D: Parabolic trough solar collector's data

Table D.0.1. Parabolic trough solar collector data

Collector	Width	Focal length	Length of module	L_{sca}
LS-1	2.55	0.94	6.3	50.2
LS-2	5	1.49	8	49
LS-3	5.76	1.71	12	99
IST	2.3	0.76	6.1	49
Euro Trough	5.76	1.71	12	150
Sky Trough	6	1.71	13.9	115

Annex E: Internal roughness (e) of common pipe materials

Table E.0.1. Internal roughness (e) of common pipe materials

Materials	**mm**	**inch**
Cast iron(Asphalt dipped)	0.122	0.004800''
Cast iron	0.4	0.001575''
Concrete	0.3	0.011811''
Copper	0.0015	0.000059''
PVC	0.005	0.000197''
Steel	0.045	0.001811''
Steel (galvanized)	0.15	0.005906''

Annex F: Electric boiler used at Assela Malt factory

Electric Hot Water Boiler 7000 kW Technical Data

Table F.0.1. Assela Malt factory used boiler specification

Type	**GET AS – 7000**
Serial Number	GET AS – 7000 – 38
year	2015
capacity	7000Kw
Steam Production	10000kg/hr
Design pressure	12 bar
Total internal volume	$1750m^3$
Length (resistances excluded)	5.4 m
Width	2.6 m
Height (excluding safety valves …)	3.050 m
Temperature	Min 0 ℃ and max 220 ℃
Capacity	16722 liter
Weight	7410 Kg
Weight full of water	24132 Kg
Hydrostatic test pressure	24 bar
Design pressure min/max	16 bar
Voltage	660 V
Frequency	50 Hz

Table F.0.2. Energy consumption of Assela Malt Factory in 2020

Month	Number of Malt produced (tons)	Electric Boiler energy consumption in (KWh)	Cost (birr)
January	3297.6	2395800	2108300.4
February	3389.4	2475000	2178000
March	3269.7	2356200	2073450.6
April	3452.5	2534400	2230270.2
May	3488.2	2455200	2160570.6
June	3332	2376000	2090880
July	3103	2296800	2021180.4
August	3483.8	2554200	2247690.6
September	3409.9	2574000	2265120
October	3287	2178000	1916640
November	3273.4	2475000	2178000
December	M	M	
Total	36,786.5	26670600	23470130

From above table the steam production capacity of electric boiler in Assela Malt factory is 10000kg/hr. the maximum temperature steam supplied for Malt kilning is around 160°C. At 6 bar pressure.

To get the energy required for steam supply of drying Malt is

Yearly required energy consumption of electric boiler at Assela Malt factory is for steam production is **2,667,060 KWh.** Since December is always free for maintenance.

$$Q_u = m.C_p.(T_{out} - T_{in})$$

Where

T_{in} (°C) – The inlet temperature of fluid to boiler. (Outlet fluid from the heat exchanger)

T_{out} – Outlet temperature of steam at exist of boiler.

C_p – Specific heat of water (4.342KJ/kg.K)

T_{out} – Maximum operating temperature used for Malt kilning.

T_{in} – In let temperature of water (feed water)

$$Q_u = 2.77\,{}^{kg}/_{s} * 4.342\,{}^{KJ}/_{Kg.℃} * (160 - 120)℃$$

$$\boldsymbol{Q_u = 465.222\ \mathrm{KW}}$$

Annex G: Moody diagram

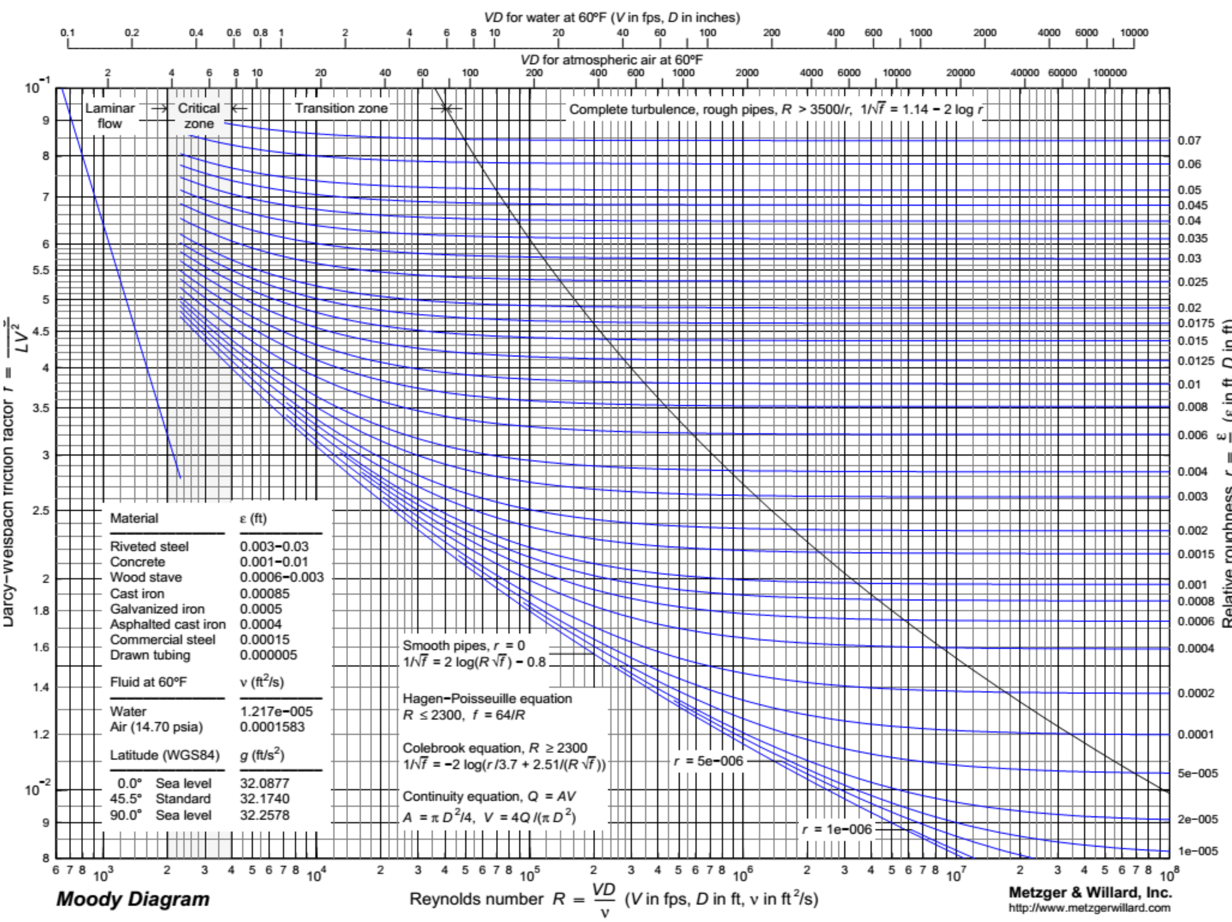

Figure G.0. 1 Moody chart

Annex H: MATLAB code

```
%%This MATLAB code Monthly Average of hourly beam incident solar radiation
%%on horizontal surface also variation of ambient temperature is calculated
%%using Kulumsa metrology data.
% January
phi=8.0141;%latitude of Kulumsa Assela
H_Jan=22.0470781;%Monthly mean daily Global radiation (MJ/m^2)
Hd_Jan=6.650026391;%%Monthly mean daily diffuse radiation (MJ/m^2)
Ws_Jan=86.91537129; %the sunset-hour angle
N_Jan=17;%n for the mean day of the month
i=0:24;% Time of the day
w=(i-12)*(15);
a_Jan=0.409+0.5016*sind((Ws_Jan-60));
b_Jan=0.6609-0.4767*sin((Ws_Jan-60)*pi/180);
G_Jan=(pi()/24)*(a_Jan+b_Jan*cos(w*pi/180)).*(cos(w*pi/180) -
cos(Ws_Jan*pi/180))/(sin(Ws_Jan*pi/180)-
(pi/180)*Ws_Jan*(cos(Ws_Jan*pi/180)));
I_Jan=(G_Jan.*H_Jan)*10^6/3600;%Monthly average hourly Global radiation in
(W/m^2)
I_Jan(I_Jan<0)=0;
Rd_Jan=(pi()/24)*(cos(w*pi/180)-cos(Ws_Jan*pi/180))/(sin(Ws_Jan*pi/180)-
(pi/180)*Ws_Jan*(cos(Ws_Jan*pi/180)));
ID_Jan=(Rd_Jan.*Hd_Jan)*10^6/3600;
ID_Jan(ID_Jan<0)=0;
Ib_Jan=I_Jan-ID_Jan %hourly beam solar radiation on horizontal surface for
January
figure
plot(i,Ib_Jan,'+-r')
legend('Jan 17')
grid on
xlabel('Time(hr)')
ylabel('beam radiation(Ib)(W/m^2)')
title('Beam Radiation for January 17 vs Time')
%February
H_Feb=23.5478; %Monthly mean daily Global radiation (MJ/m^2)
Hd_Feb= 7.317882646;%Monthly mean daily diffuse radiation(MJ/m^2)
Ws_Feb=88.14404375; %the sunset-hour angle
N_Feb=47;%n for the mean day of the month
Decl_Feb=23.5*sin((360*(284+N_Feb)/365)*pi/180);
a_Feb=0.409+0.5016*sin((Ws_Feb-60)*pi/180);
b_Feb=0.6609-0.4767*sin((Ws_Feb-60)*pi/180);
G_Feb=(pi()/24)*(a_Feb+b_Feb*cos(w*pi/180)).*(cos(w*pi/180) -
cos(Ws_Feb*pi/180))/(sin(Ws_Feb*pi/180)-
(pi/180)*Ws_Feb*(cos(Ws_Feb*pi/180)));
I_Feb=(G_Feb.*H_Feb)*10^6/3600;%Monthly mean hourly Global radiation
I_Feb(I_Feb<0)=0;
Rd_Feb=(pi()/24)*(cos(w*pi/180)-cos(Ws_Feb*pi/180))/(sin(Ws_Feb*pi/180)-
(pi/180)*Ws_Feb*(cos(Ws_Feb*pi/180)));
ID_Feb=(Rd_Feb.*Hd_Feb)*10^6/3600;
ID_Feb(ID_Feb<0)=0;
Ib_Feb=I_Feb-ID_Feb;%hourly beam solar radiation on horizonT_rl surface for
February
figure
plot(i,Ib_Feb,'<-b')
legend('Feb 16')
```

```
grid on
xlabel('Time(hr)')
ylabel('beam radiation(Ib)(W/m^2)')
title('Beam Radiation for February 16 vs Time')
% march
H_Mar=23.56240415;%Monthly mean daily Global radiation (MJ/m^2)
Hd_Mar=9.732296503;
Ws_Mar=89.65939859; %the sunset-hour angle
N_Mar=75;
Decl_Mar=23.5*sin((360*(284+N_Mar)/365)*pi/180);
a_Mar=0.409+0.5016*sin((Ws_Mar-60)*pi/180);
b_Mar=0.6609-0.4767*sin((Ws_Mar-60)*pi/180);
i=0:24;
w=(i-12)*(15);
G_Mar=(pi()/24)*(a_Mar+b_Mar*cos(w*pi/180)).*(cos(w*pi/180) -
cos(Ws_Mar*pi/180))/(sin(Ws_Mar*pi/180)-
(pi/180)*Ws_Mar*(cos(Ws_Mar*pi/180)));
I_Mar=(G_Mar.*H_Mar)*10^6/3600;%Monthly mean hourly Global radiation
I_Mar(I_Mar<0)=0;
Rd_Mar=(pi()/24)*(cos(w*pi/180)-cos(Ws_Mar*pi/180))/(sin(Ws_Mar*pi/180)-
(pi/180)*Ws_Mar*(cos(Ws_Mar*pi/180)));
ID_Mar=(Rd_Mar.*Hd_Mar)*10^6/3600;
ID_Mar(ID_Mar<0)=0;
Ib_Mar=I_Mar-ID_Mar;%hourly beam solar radiation on horizonT_rl surface for
March
figure
plot(i,Ib_Mar,'<-K')
legend('Mar 17')
grid on
xlabel('Time(hr)')
ylabel('beam radiation(Ib)(W/m^2)')
title('Beam Radiation for March 16 vs Time')
% April
H_Apr=23.29737762;%Monthly mean daily Global radiation (MJ/m^2)
Hd_Apr=10.45129947;
Ws_Apr=91.33772201; %the sunset-hour angle
N_Apr=105;
Decl_Apr=23.5*sin((360*(284+N_Apr)/365)*pi/180);
a_Apr=0.409+0.5016*sin((Ws_Apr-60)*pi/180);
b_Apr=0.6609-0.4767*sin((Ws_Apr-60)*pi/180);
i=0:24;
w=(i-12)*(15);
cozeT_r4=(sin(phi*pi/180))*(sin(Decl_Apr*pi/180))+(cos(phi*pi/180))*(cos(Decl
_Apr*pi/180))*(cos(w*pi/180));
G_Apr=(pi()/24)*(a_Apr+b_Apr*cos(w*pi/180)).*(cos(w*pi/180) -
cos(Ws_Apr*pi/180))/(sin(Ws_Apr*pi/180)-
(pi/180)*Ws_Apr*(cos(Ws_Apr*pi/180)));
I_Apr=(G_Apr.*H_Apr)*10^6/3600;%Monthly mean hourly Global radiation
I_Apr(I_Apr<0)=0;
Rt_Apr=(pi()/24)*(cos(w*pi/180)-cos(Ws_Apr*pi/180))/(sin(Ws_Apr*pi/180)-
(pi/180)*Ws_Apr*(cos(Ws_Apr*pi/180)));
ID_Apr=(Rt_Apr.*Hd_Apr)*10^6/3600;
ID_Apr(ID_Apr<0)=0;
Ib_Apr=I_Apr-ID_Apr;%hourly beam solar radiation on horizonT_rl surface for
April
```

```
figure
plot(i,Ib_Apr,'^-b')
legend('Apr 15')
grid on
xlabel('Time(hr)')
ylabel('beam radiation(Ib)(W/m^2)')
title('Beam Radiation for April 15 vs Time')
%may
phi=8.0141;
H_May=22.22586052;%Monthly mean daily Global radiation (MJ/m^2)
Hd_May=10.6596097;
Ws_May=92.74593573; %the sunset-hour angle
N_May=135;
Decl_May=23.5*sin((360*(284+N_May)/365)*pi/180);
a_May=0.409+0.5016*sin((Ws_May-60)*pi/180);
b_May=0.6609-0.4767*sin((Ws_May-60)*pi/180);
i=0:24;
w=(i-12)*(15);
cozeT_r5=(sin(phi*pi/180))*(sin(Decl_May*pi/180))+(cos(phi*pi/180))*(cos(Decl
_May*pi/180))*(cos(w*pi/180));
G_May=(pi()/24)*(a_May+b_May*cos(w*pi/180)).*(cos(w*pi/180)                 -
cos(Ws_May*pi/180))/(sin(Ws_May*pi/180)-
(pi/180)*Ws_May*(cos(Ws_May*pi/180)));
I_May=(G_May.*H_May)*10^6/3600;%Monthly mean hourly Global radiation
I_May(I_May<0)=0;
costeT_rp5=cos(Decl_May*pi/180);%Polar N-S axis with E-W tracking
Rd_May=(pi()/24)*(cos(w*pi/180)-cos(Ws_May*pi/180))/(sin(Ws_May*pi/180)-
(pi/180)*Ws_May*(cos(Ws_May*pi/180)));
ID_May=(Rd_May.*Hd_May)*10^6/3600;
ID_May(ID_May<0)=0;
Ib_May=I_May-ID_May;%hourly beam solar radiation on horizonT_rl surface for
March
figure
plot(i,Ib_May,'>-B')
legend('May 15')
grid on
xlabel('Time(hr)')
ylabel('beam radiation(Ib)(W/m^2)')
title('Beam Radiation for May 15 vs Time')
%June
H_Jun=21.46072658;%Monthly mean daily Global radiation (MJ/m^2)
Hd_Jun=10.62857541;
Ws_Jun=93.44049438; %the sunset-hour angle
N_Jun=162;
Decl_Jun=23.5*sin((360*(284+N_Jun)/365)*pi/180);
a_Jun=0.409+0.5016*sin((Ws_Jun-60)*pi/180);
b_Jun=0.6609-0.4767*sin((Ws_Jun-60)*pi/180);
i=0:24;
w=(i-12)*(15);
cozeT_r6=(sin(phi*pi/180))*(sin(Decl_Jun*pi/180))+(cos(phi*pi/180))*(cos(Decl
_Jun*pi/180))*(cos(w*pi/180));
G_Jun=(pi()/24)*(a_Jun+b_Jun*cos(w*pi/180)).*(cos(w*pi/180)                 -
cos(Ws_Jun*pi/180))/(sin(Ws_Jun*pi/180)-
(pi/180)*Ws_Jun*(cos(Ws_Jun*pi/180)));
I_Jun=(G_Jun.*H_Jun)*10^6/3600;%Monthly mean hourly Global radiation
```

```
I_Jun(I_Jun<0)=0;
Rd_Jun=(pi()/24)*(cos(w*pi/180)-cos(Ws_Jun*pi/180))/(sin(Ws_Jun*pi/180)-
(pi/180)*Ws_Jun*(cos(Ws_Jun*pi/180)));
ID_Jun=(Rd_Jun.*Hd_Jun)*10^6/3600;
ID_Jun(ID_Jun<0)=0;
Ib_Jun=I_Jun-ID_Jun;%hourly beam solar radiation on horizonT_rl surface for
March
figure
plot(i,Ib_Jun,'*-g')
legend('June 11')
grid on
xlabel('Time(hr)')
ylabel('beam radiation(Ib)(W/m^2)')
title('Beam Radiation for June 11 vs Time')
%July
H_Jul=18.92442057;%Monthly mean daily Global radiation (MJ/m^2)
Hd_Jul=11.26140663;
Ws_Jul=93.12780847; %the sunset-hour angle
N_Jul=198;
Decl_Jul=23.5*sin((360*(284+N_Jul)/365)*pi/180);
a_Jul=0.409+0.5016*sin((Ws_Jul-60)*pi/180);
b_Jul=0.6609-0.4767*sin((Ws_Jul-60)*pi/180);
i=0:24;
w=(i-12)*(15);
G_Jul=(pi()/24)*(a_Jul+b_Jul*cos(w*pi/180)).*(cos(w*pi/180)                   -
cos(Ws_Jul*pi/180))/(sin(Ws_Jul*pi/180)-
(pi/180)*Ws_Jul*(cos(Ws_Jul*pi/180)));
I_Jul=(G_Jul.*H_Jul)*10^6/3600;%Monthly mean hourly Global radiation
I_Jul(I_Jul<0)=0;
Rd_Jul=(pi()/24)*(cos(w*pi/180)-cos(Ws_Jul*pi/180))/(sin(Ws_Jul*pi/180)-
(pi/180)*Ws_Jul*(cos(Ws_Jul*pi/180)));
ID_Jul=(Rd_Jul.*Hd_Jul)*10^6/3600;
ID_Jul(ID_Jul<0)=0;
Ib_Jul=I_Jul-ID_Jul;%hourly beam solar radiation on horizonT_rl surface for
March
figure
plot(i,Ib_Jul,'+-r')
legend('July 17')
grid on
xlabel('Time(hr)')
ylabel('beam radiation(Ib)(W/m^2)')
title('Beam Radiation for July 17 vs Time')
%August
H_Aug=19.87433288;%Monthly mean daily Global radiation (MJ/m^2)
Hd_Aug=11.44229294;
Ws_Aug=91.9303211; %the sunset-hour angle
N_Aug=228;
Decl_Aug=23.5*sin((360*(284+N_Aug)/365)*pi/180);
a_Aug=0.409+0.5016*sin((Ws_Aug-60)*pi/180);
b_Aug=0.6609-0.4767*sin((Ws_Aug-60)*pi/180);
i=0:24;
w=(i-12)*(15);
G_Aug=(pi()/24)*(a_Aug+b_Aug*cos(w*pi/180)).*(cos(w*pi/180)                   -
cos(Ws_Aug*pi/180))/(sin(Ws_Aug*pi/180)-
(pi/180)*Ws_Aug*(cos(Ws_Aug*pi/180)));
```

```
I_Aug=(G_Aug.*H_Aug)*10^6/3600;%Monthly mean hourly Global radiation
I_Aug(I_Aug<0)=0;
Rd_Aug=(pi()/24)*(cos(w*pi/180)-cos(Ws_Aug*pi/180))/(sin(Ws_Aug*pi/180)-
(pi/180)*Ws_Aug*(cos(Ws_Aug*pi/180)));
ID_Aug=(Rd_Aug.*Hd_Aug)*10^6/3600;
ID_Aug(ID_Aug<0)=0;
Ib_Aug=I_Aug-ID_Aug;%hourly beam solar radiation on horizonT_rl surface for
March
figure
plot(i,Ib_Aug,'>-b')
legend('Aug 16')
grid on
xlabel('Time(hr)')
ylabel('beam radiation(Ib)(W/m^2)')
title('Beam Radiation for August 16 vs Time')
% September
H_Sep=19.36761059;%Monthly mean daily Global radiation (MJ/m^2)
Hd_Sep=11.4576099;
Ws_Sep=90.31227686; %the sunset-hour angle
N_Sep=258;
Decl_Sep=23.5*sin((360*(284+N_Sep)/365)*pi/180);
a_Sep=0.409+0.5016*sin((Ws_Sep-60)*pi/180);
b_Sep=0.6609-0.4767*sin((Ws_Sep-60)*pi/180);
i=0:24;
w=(i-12)*(15);
G_Sep=(pi()/24)*(a_Sep+b_Sep*cos(w*pi/180)).*(cos(w*pi/180)              -
cos(Ws_Sep*pi/180))/(sin(Ws_Sep*pi/180)-
(pi/180)*Ws_Sep*(cos(Ws_Sep*pi/180)));
I_Sep=(G_Sep.*H_Sep)*10^6/3600;%Monthly mean hourly Global radiation
I_Sep(I_Sep<0)=0;
Rd_Sep=(pi()/24)*(cos(w*pi/180)-cos(Ws_Sep*pi/180))/(sin(Ws_Sep*pi/180)-
(pi/180)*Ws_Sep*(cos(Ws_Sep*pi/180)));
ID_Sep=(Rd_Sep.*Hd_Sep)*10^6/3600;
ID_Sep(ID_Sep<0)=0;
Ib_Sep=I_Sep-ID_Sep;%hourly beam solar radiation on horizonT_rl surface for
March
figure
plot(i,Ib_Sep,'*-g')
legend('Sep 15')
grid on
xlabel('Time(hr)')
ylabel('beam radiation(Ib)(W/m^2)')
title('Beam Radiation for September 15 vs Time')
%October
H_Oct=22.6372326;%Monthly mean daily Global radiation (MJ/m^2)
Hd_Oct=9.262083145;
Ws_Oct=88.63556536; %the sunset-hour angle
N_Oct=288;
Decl_Oct=23.5*sin((360*(284+N_Oct)/365)*pi/180);
a_Oct=0.409+0.5016*sin((Ws_Oct-60)*pi/180);
b_Oct=0.6609-0.4767*sin((Ws_Oct-60)*pi/180);
i=0:24;
w=(i-12)*(15);
```

```
G_Oct=(pi()/24)*(a_Oct+b_Oct*cos(w*pi/180)).*(cos(w*pi/180) -
cos(Ws_Oct*pi/180))/(sin(Ws_Oct*pi/180)-
(pi/180)*Ws_Oct*(cos(Ws_Oct*pi/180)));
I_Oct=(G_Oct.*H_Oct)*10^6/3600;%Monthly mean hourly Global radiation
I_Oct(I_Oct<0)=0;
Rd_Oct=(pi()/24)*(cos(w*pi/180)-cos(Ws_Oct*pi/180))/(sin(Ws_Oct*pi/180)-
(pi/180)*Ws_Mar*(cos(Ws_Oct*pi/180)));
ID_Oct=(Rd_Oct.*Hd_Oct)*10^6/3600;
ID_Oct(ID_Oct<0)=0;
Ib_Oct=I_Oct-ID_Oct;%hourly beam solar radiation on horizonT_rl surface for
October
figure
plot(i,Ib_Oct,'+-b')
legend('Oct 15')
grid on
xlabel('Time(hr)')
ylabel('beam radiation(Ib)(W/m^2)')
title('Beam Radiation for October 15 vs Time')
%November
H_Nov=21.47419651;%Monthly mean daily Global radiation (MJ/m^2)
Hd_Nov=8.328282079;
Ws_Nov=87.23517191; %the sunset-hour angle
N_Nov=318;
Decl_Nov=23.5*sin((360*(284+N_Nov)/365)*pi/180);
a_Nov=0.409+0.5016*sin((Ws_Nov-60)*pi/180);
b_Nov=0.6609-0.4767*sin((Ws_Nov-60)*pi/180);
i=0:24;
w=(i-12)*(15);
G_Nov=(pi()/24)*(a_Mar+b_Mar*cos(w*pi/180)).*(cos(w*pi/180) -
cos(Ws_Nov*pi/180))/(sin(Ws_Nov*pi/180)-
(pi/180)*Ws_Nov*(cos(Ws_Nov*pi/180)));
I_Nov=(G_Nov.*H_Nov)*10^6/3600;%Monthly mean hourly Global radiation
I_Nov(I_Nov<0)=0;
Rd_Nov=(pi()/24)*(cos(w*pi/180)-cos(Ws_Nov*pi/180))/(sin(Ws_Nov*pi/180)-
(pi/180)*Ws_Nov*(cos(Ws_Nov*pi/180)));
ID_Nov=(Rd_Nov.*Hd_Nov)*10^6/3600;
ID_Nov(ID_Nov<0)=0;
Ib_Nov=I_Nov-ID_Nov; %hourly beam solar radiation on horizonT_rl surface for
November
figure
plot(i,Ib_Nov,'*-b')
legend('Nov 14')
grid on
xlabel('Time(hr)')
ylabel('beam radiation(Ib)(W/m^2)')
title('Beam Radiation for November 14 vs Time')
%December
H_Dec=21.51397144;%Monthly mean daily Global radiation (MJ/m^2)
Hd_Dec=6.393507106;
Ws_Dec=86.56555139; %the sunset-hour angle
N_Dec=344;
Decl_Dec=23.5*sin((360*(284+N_Dec)/365)*pi/180);
a_Dec=0.409+0.5016*sin((Ws_Dec-60)*pi/180);
b_Dec=0.6609-0.4767*sin((Ws_Dec-60)*pi/180);
i=0:24;
```

```
w=(i-12)*(15);
G_Dec=(pi()/24)*(a_Dec+b_Dec*cos(w*pi/180)).*(cos(w*pi/180) -
cos(Ws_Dec*pi/180))/(sin(Ws_Dec*pi/180)-
(pi/180)*Ws_Dec*(cos(Ws_Dec*pi/180)));
I_Dec=(G_Dec.*H_Dec)*10^6/3600; % Monthly mean hourly Global radiation
I_Dec(I_Dec<0)=0;
Rd_Dec=(pi()/24)*(cos(w*pi/180)-cos(Ws_Dec*pi/180))/(sin(Ws_Dec*pi/180)-
(pi/180)*Ws_Dec*(cos(Ws_Dec*pi/180)));
ID_Dec=(Rd_Dec.*Hd_Dec)*10^6/3600;
ID_Dec(ID_Dec<0)=0;
Ib_Dec=I_Dec-ID_Dec; % hourly beam solar radiation on horizonT_rl surface for
December
figure
plot(i,Ib_Dec,'*-k')
legend('Dec 10')
grid on
xlabel('Time(hr)')
ylabel('beam radiation(Ib)(W/m^2)')
title('Beam Radiation for December 10 vs Time')
%Hourly Ambient temperature
%The code for calculation of hourly ambient variation for January. For other %
months we can calculate in similar manner
Tmax=[24.0431 24.0431   24.0431 24.0431 24.0431 24.0431 24.0431 24.0431 24.0431
24.0431 24.0431 24.0431 24.0431 24.0431 24.0431 24.0431 24.0431 24.0431 24.0431
24.0431 24.0431 24.0431 24.0431 24.0431 24.0431
];
Tmin=[9.4474 9.4474 9.4474   9.4474   9.4474   9.4474   9.4474   9.4474   9.4474
9.4474   9.4474   9.4474   9.4474   9.4474   9.4474   9.4474   9.4474   9.4474   9.4474
9.4474   9.4474   9.4474   9.4474   9.4474   9.4474
];
DR = Tmax-Tmin;
T_rmean=(Tmax+Tmin)/2;
thmax=14;
t=0:1:24;
T_rmb=T_rmean+((DR/2).*(cos(2*pi*(t-thmax)/24)));
figure
plot(t,T_rmb,'+-k')
legend('Jan 17')
grid on
xlabel('Time(hr)')
ylabel('Ambient Temprature (C)')
title('Ambient Temprature Variation for January 17 vs Time')
```

```
%Code for simulation of Parabolic trough collector performance
```

```
% optical performance
L=5; %length of the collector
w=3.4; %width of the collector
di=0.066; %inner diameter of the receiver pipe
do=0.07; %outer diameter of the receiver pipe
Dco=0.109; %outer diameter of the Glass cover
Dci=0.115; %sfner diameter of the Glass cover
Ari=pi*di*L; % Internal raaciever area
er=0.24; %receiver tube emittance
eci=0.86; %Glass Cover emittance
eco=0.88; %
gct=0.95; %Glass Cover transmittance
rta=0.94; % Receiver tube absorbance
rsr=0.93; %Reflected surface reflectivity
sf=0.92; %sftercept factor(Shape factor)
n1=17; %n for the mean day of the month
dec1=23.5*sin((360*(284+n1)/365)*pi/180);%Decelaretion
costeta1=cos(dec1*pi/180);%PolAri N-S axis with E-W tracksfg;
teta1=acos(costeta1);
kteta1=costeta1+0.0003178*(teta1)-0.00003985*(teta1).^2;% modifier
opeff1=sf*gct*rta*rsr*kteta1; %Optical effeciency
n2=47; %n for the mean day of the month
dec2=23.5*sin((360*(284+n2)/365)*pi/180); %Declsfation
costeta2=cos(dec2*pi/180); %PolAri N-S axis with E-W tracksfg;
teta2=acos(costeta2);
kteta2=costeta2+0.0003178*(teta2)-0.00003985*(teta2).^2;    %sfcident    angle
modifier
opeff2=sf*gct*rta*rsr*kteta2; %Optical effeciency
n3=75; %n for the mean day of the month
dec3=23.5*sin((360*(284+n3)/365)*pi/180);
costeta3=cos(dec3*pi/180); %PolAri N-S axis with E-W tracksfg;
teta3=acos(costeta3);
kteta3=costeta2+0.0003178*(teta3)-0.00003985*(teta3).^2;    %sfcident    angle
modifier
opeff3=sf*gct*rta*rsr*kteta3; %Optical effeciency
n4=105; %n for the mean day of the month
dec4=23.5*sin((360*(284+n4)/365)*pi/180);
costeta4=cos(dec4*pi/180); %PolAri N-S axis with E-W tracksfg;
teta4=acos(costeta4);
kteta4=costeta4+0.0003178*(teta4)-0.00003985*(teta4).^2;    %sfcident    angle
modifier
opeff4=sf*gct*rta*rsr*kteta4; %Optical effeciency
n5=135; %n for the mean day of the month
dec5=23.5*sin((360*(284+n5)/365)*pi/180);
costeta5=cos(dec5*pi/180); %PolAri N-S axis with E-W tracksfg;
teta5=acos(costeta5);
kteta5=costeta5+0.0003178*(teta5)-0.00003985*(teta5).^2;    %sfcident    angle
modifier
opeff5=sf*gct*rta*rsr*kteta5; %Optical effeciency
n6=162; %n for the mean day of the month
dec6=23.5*sin((360*(284+n6)/365)*pi/180);
costeta6=cos(dec6*pi/180); %PolAri N-S axis with E-W tracksfg;
teta6=acos(costeta6);
kteta6=costeta6+0.0003178*(teta6)-0.00003985*(teta6).^2;    %sfcident    angle
modifier
```

```
opeff6=sf*gct*rta*rsr*kteta6; %Optical effeciency
n7=198;%n for the mean day of the month
dec7=23.5*sin((360*(284+n7)/365)*pi/180);
costeta7=cos(dec7*pi/180); %PolAri N-S axis with E-W tracksfg;
teta7=acos(costeta7);
kteta7=costeta7+0.0003178*(teta7)-0.00003985*(teta7).^2;    %sfcident    angle
modifier
opeff7=sf*gct*rta*rsr*kteta7; %Optical effeciency
n8=228; %n for the mean day of the month
dec8=23.5*sin((360*(284+n8)/365)*pi/180);
costeta8=cos(dec8*pi/180); %PolAri N-S axis with E-W tracksfg;
teta8=acos(costeta8);
kteta8=costeta8+0.0003178*(teta8)-0.00003985*(teta8).^2;    %sfcident    angle
modifier
opeff8=sf*gct*rta*rsr*kteta8; %Optical effeciency
n9=258; %n for the mean day of the month
dec9=23.5*sin((360*(284+n9)/365)*pi/180);
costeta9=cos(dec9*pi/180); %PolAri N-S axis with E-W tracksfg;
teta9=acos(costeta9);
kteta9=costeta9+0.0003178*(teta9)-0.00003985*(teta9).^2; %sfcident angle
opeff9=sf*gct*rta*rsr*kteta9; %Optical effeciency
n10=288; %n for the mean day of the month
dec10=23.5*sin((360*(284+n10)/365)*pi/180);
costeta10=cos(dec10*pi/180); %PolAri N-S axis with E-W tracksfg;
teta10=acos(costeta10);
kteta10=costeta10+0.0003178*(teta10)-0.00003985*(teta10).^2;%sfcident    angle
modifier
opeff10=sf*gct*rta*rsr*kteta10;%Optical effeciency
n11=318;%n for the mean day of the month
dec11=23.5*sin((360*(284+n11)/365)*pi/180);
costeta11=cos(dec11*pi/180);%PolAri N-S axis with E-W tracksfg;
teta11=acos(costeta11);
kteta11=costeta11+0.0003178*(teta11)-0.00003985*(teta11).^2;%sfcident    angle
modifier
opeff11=sf*gct*rta*rsr*kteta11;%Optical effeciency
n12=344; %n for the mean day of the month
dec12=23.5*sin((360*(284+n12)/365)*pi/180);
costeta12=cos(dec12*pi/180); %PolAri N-S axis with E-W tracksfg;
teta12=acos(costeta12);
kteta12=costeta12+0.0003178*(teta12)-0.00003985*(teta12).^2;  %sfcident  angle
modifier
opeff12=sf*gct*rta*rsr*kteta12; %Optical effeciency
Z=[opeff1  opeff2  opeff3  opeff4  opeff5  opeff6  opeff7  opeff8  opeff9  opeff10
opeff11 opeff12];
bar(Z)
```

```
%%%Phase change materials code for Assela Malt factory
function dmannitol_pcm
global L ro R N_z N_r N_t e v f_dens l_f c_f mu_f r_s1 r_s2 c_s1 c_s2 l_s1 l_s2
lh
global u_m1 u_m2 h_f u1 u2 d_t Re Pr tend
L=2.7;         % Length of cylinder in m
ro = 0.03;  %Radius of the tube (m)
R = 0.06;   % Diameter of the tube(m)
ratio = fix(L/(R-ro));
N_z = 800;  %Number of points in x direction
N_r = fix(N_z/ratio) % Number of points in r direction
time =11*3600;
N_t =11*3600*0.03 ;  %time (second)
dt = time/(N_t-1);
%% Physical properties of HTF (Water)
rho_f = 985;  %density (kg/m3)
mio_f = 4.92*10^-4;  %Dynamic viscosity of HTF water (kg/m s)
Cp_f = 4342;  %Specific heat capacity (J/kg.K)
m_f = 0.01;  %Mass flow rate of HTF (kg/s)
k_f = 0.652;% Thermal conductivity of water
Np=197;% Number of tubes in PCM
Re = 2*m_f/(pi*Np*ro*mio_f)  %Reynolds number
Pr = Cp_f*mio_f/k_f  %Prantel number
if Re<2200
    Nu = 3.66;
else
  if Re>5*10^6
     Nu = 0.023*Re^0.8*Pr^0.4;
  else
     if(Re >=2100)&& (Re<=5*10^6);
       f = ((0.79*log(Re))-1.64)^-2;
      Nu = ((f/8)*(Re-1000)*Pr)/(1+(12.7*((f/8)^0.5)*((Pr^(2/3))-1)));
     end
  end
end
h =Nu*k_f/(2*ro)  %Convective heat transfer coefficient (W/m2.k)
%%Physical properties of PCM (D-mannitol)
e=0.45;          % Porosity
v=4.715E-04;     % Fluid velocity in m/s
l_f=0.1690;      % Fluid thermal conductivity
c_f=2388.88;     % Fluid specific heat capacity
f_dens=874.4;  % Fluid density
mu_f=9.716E-3; % Fluid dynamic viscosity
d_t=0.06;      % Diameter of tubes
r_s1=1490;     % Density of solid PCM
r_s2=1300;     % Density of liquid PCM
c_s1=1310;     % Specific heat of solid PCM(J/kg.K)
c_s2=2360;     % Specific heat of liquid PCM(J/kg.K)
l_s1=0.19;     % Thermal conductivity of solid PCM (W/mK)
l_s2=0.11;     % Thermal conductivity of liquid PCM (W/mK)
lh=300000;     % Latent heat of fusion for PCM
u_m1=163;      % Lower limit melting temperature for phase change in K
u_m2=168.2;    % Upper limit melting temperature for phase change in K
tend=21600;    % seconds
```

```
Re=(f_dens*d_t*e*v)/mu_f; % Reynold number
Pr=(c_f*mu_f)/l_f; % Prandtl Number
h_f=(((6*(1-e))*(2+(1.1*(Re^0.6)*(Pr^(1/3)))*l_f))/(d_t^2));  %  Heat  transfer
coefficient
m = 0;
x = linspace(0,L,800); % Space discretization
t = 0:1:tend; % Time discretization
sol = pdepe(m,@tes1pde,@tes1ic,@tes1bc,x,t);

u1 = sol(:,:,1); % Solution for fluid phase
u2 = sol(:,:,2); % Solution for solid phase

% Plot of temperature variation with time for fluid

figure, plot(t,u2(:,10),'r',t,u1(:,10),'r:')
hold all
plot(t,u2(:,400),'c',t,u1(:,400),'c:')
hold all
plot(t,u2(:,700),'c',t,u1(:,700),'c:')
hold all
hleg2 = legend('T1','T2','T3','T4');
xlabel('Time,t')
ylabel('Temperature,T')
grid on;
set(hleg2,'location','SouthEast')
xlabel('Time (sec)')
ylabel('Temperature (^OC)')

function [c,f,s] = tes1pde(x,t,u,DuDx)
global l_f v f_dens c_f h_f e c_s1 c_s2 r_s1 r_s2 lh u_m1 u_m2 l_s1 l_s2
     if (u(2)<u_m1)
         c = [(e*f_dens*c_f); ((1-e)*r_s1*c_s1)];
     elseif (u(2)>=u_m1 && u(2)<u_m2)
         c                =                [(e*f_dens*c_f);                ((1-
e)*((r_s1+r_s2)./2)*(((c_s1+c_s2)/2)+(lh./(u_m2-u_m1))))];
     else
         c = [(e*f_dens*c_f); ((1-e)*r_s2*c_s2)];
     end
     if (u(2)<u_m1)
         f = [(e*l_f*DuDx(1))-(e*v*f_dens*c_f*u(1)); (1-e)*l_s1*DuDx(2)];
     elseif (u(2)>=u_m1 && u(2)<u_m2)
         f       =       [(e*l_f*DuDx(1))-(e*v*f_dens*c_f*u(1));        (1-
e)*((l_s1+l_s2)/2)*DuDx(2)];
     else
         f = [(e*l_f*DuDx(1))-(e*v*f_dens*c_f*u(1)); (1-e)*l_s2*DuDx(2)];
     end
        s = [-(h_f*(u(1)-u(2))); (h_f*(u(1)-u(2)))];
function u0 = tes1ic(x)
u0 = [25; 25];
function [pl,ql,pr,qr] = tes1bc(xl,ul,xr,ur,t)
global e v f_dens c_f
pl = [e*v*f_dens*c_f*244.85; ul(2)];
ql = [1; 1];
pr = [e*v*f_dens*c_f*ur(1); ur(2)];
qr = [1; 1];
```